

INFORMATION TO USERS

This manuscript has been reproduced from the microfilm master. UMI films the text directly from the original or copy submitted. Thus, some thesis and dissertation copies are in typewriter face, while others may be from any type of computer printer.

The quality of this reproduction is dependent upon the quality of the copy submitted. Broken or indistinct print, colored or poor quality illustrations and photographs, print bleedthrough, substandard margins, and improper alignment can adversely affect reproduction.

In the unlikely event that the author did not send UMI a complete manuscript and there are missing pages, these will be noted. Also, if unauthorized copyright material had to be removed, a note will indicate the deletion.

Oversize materials (e.g., maps, drawings, charts) are reproduced by sectioning the original, beginning at the upper left-hand corner and continuing from left to right in equal sections with small overlaps. Each original is also photographed in one exposure and is included in reduced form at the back of the book.

Photographs included in the original manuscript have been reproduced xerographically in this copy. Higher quality 6" x 9" black and white photographic prints are available for any photographs or illustrations appearing in this copy for an additional charge. Contact UMI directly to order.

UMI

**A Bell & Howell Information Company
300 North Zeeb Road, Ann Arbor MI 48106-1346 USA
313/761-4700 800/521-0600**

**Solar Infrared Relative Intensity Data From The
Halogen Occultation Experiment**

A Dissertation

Presented to The Faculty of the Department of Physics

The College of William and Mary

In Partial Fulfillment

Of the Requirements for the Degree of

Doctor of Philosophy

By

Philip Todd Spickler

May 1997

UMI Number: 9805164

UMI Microform 9805164
Copyright 1997, by UMI Company. All rights reserved.

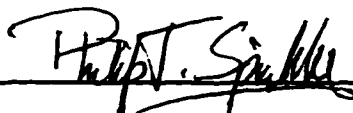
**This microform edition is protected against unauthorized
copying under Title 17, United States Code.**

UMI
300 North Zeeb Road
Ann Arbor, MI 48103

APPROVAL SHEET

This dissertation is submitted in partial fulfillment
of the requirements for the degree of

Doctor of Philosophy.



Philip Todd Spickler

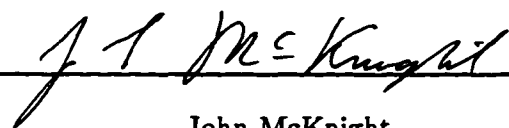
Approved, April 1997



D. Chris Benner, Advisor



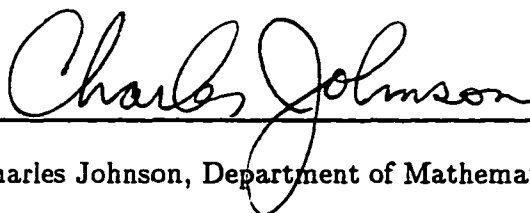
Eugene Tracy



John McKnight



Roy Champion



Charles Johnson, Department of Mathematics

To Katrina; you are my sunshine.

Contents

Acknowledgements	vi
List of Tables	vii
List of Figures	viii
Abstract	xii
Chapter 1 Introduction	2
1.1 The Sun - A General Description	5
1.2 The Photosphere	8
1.2.1 Wavelengths of Observations	8
1.2.2 The Quiet Photosphere	11
1.2.3 Sunspots	12
1.3 Solar Models	13
Chapter 2 Radiative Transfer	15
Chapter 3 Instrument And Observing Information	23
3.1 Spectral Response	25
3.2 Spatial Response	28
3.3 Sun Sensor	28
3.4 Electronics Response	31
Chapter 4 Analysis Technique	33
4.1 Nonlinear Least Squares	33
4.2 Limb Darkening Analysis	37
4.2.1 The Instrument Model	39
4.2.2 Analysis Description	45
4.3 Sunspot Intensity Analysis	47

4.3.1	Position Determination of the Sunspot	48
4.3.2	Analysis Technique	53
4.3.3	Calculation of Sunspot Parameter Derivatives	56
Chapter 5 Photospheric Relative Intensity and Temperature		57
5.1	Instrument and Observing Information	57
5.2	Relative Intensity Results	59
5.3	Temperature Analysis	67
5.3.1	Calculated Disk Brightness Temperatures, $T_b^{disk}(\lambda)$	67
5.3.2	Calculated $T(\tau_\lambda)$	71
Chapter 6 Sunspot Intensity and Temperature		75
6.1	Instrument Parameters and Data Information	75
6.2	Modified Sunspot Analysis Technique	77
6.3	Sunspot Relative Intensity Results	83
6.4	Temperature Analysis	88
Chapter 7 Conclusions		91
Appendix A Sunspot Parameter Derivatives		95
Bibliography		100
VITA		103

Acknowledgements

There are many people who have made this undertaking possible by giving me advice, information, and/or encouragement. I will begin by expressing my gratitude to my thesis advisor, Dr. D. Chris Benner whose guidance and insight have been invaluable. I especially appreciate the attentiveness he has shown towards me and my work even while shouldering many other responsibilities.

I have had many outstanding physics instructors, and I would like to recognize two in particular. My undergraduate physics teachers, Dr. Dean R. Neher and Dr. Dale V. Ulrich, helped develop my skills and were instrumental in helping me achieve loftier goals than I had initially set. Their enthusiasm for physics and teaching will never be forgotten.

While at William and Mary, I have had the great fortune of being connected with two outstanding groups of people. Thanks to the HALOE team at NASA Langley for your hospitality and your expertise: Guy Beaver, Mike Cisewski, Lance Deaver, Jill Fries, Larry Gordley, Joe McInerney, Sudha Natarajan, Pat Purcell, Ken Stone, Stan Shultz, and Earl Thompson. A special thank you to HALOE's principal investigator, James M. Russell, III and to John Wells for their support of this research through words of encouragement and funding. Appreciation is also expressed to Peter Taylor of the AAVSO, who promptly supplied the American Relative Sunspot Numbers and other valuable solar information. I also thank my friends in the Physics Department at William and Mary. Mike West, Mike Seale, Mike Zickel, and Pierre Emeric for the lunch conversations at Langley. Classmates Chris Nichols, Justin McIntyre, Danielle Gaitano, and Maciek Sasinowski for first (and second and third ...) year survival techniques. Special thanks to Rob Martin for all the technical information (I have another Latex question ...) and the B & B dinners. Thanks also to Paula, Sylvia, and Dianne for taking care of the maze of details and making the trip much smoother.

This project would never have been completed without the undying support from my family, my extended family and friends. I would like to say thank you to all these folks for the uplifting thoughts and best wishes they sent my way: my parents, Warren and Verdella Spickler; my sister Chris and husband Mike along with Jonathan, Joshua, Rachel, and Rebbekah (thanks for the cards!); my sister Gail and husband Kris. Thanks also goes to my extended family: Shirley Malnar; Lewis Paulin; Larry, Angie, Kristen, Mark and Adam Caplinger. I would also like to say a special thank you to all the folks we call friends, especially Sherry and Pete Gohdes, Donna and Tom Farrish, Dewie and Doc Arey, Robert and Leslie Bates, and Anne and Gary Gordon. Getting together with you was the best form of sanity preservation!

And finally to my wife, Katrina —my companion and best friend— my loving thanks. Her patience and understanding surpassed reasonable limits, and I can not begin to express in words my appreciation for all her support and dreaming the dream with me.

List of Tables

3.1	HALOE Wavelengths and Bandwidths at 5% Level.	28
5.1	Coefficients to the limb-darkening function at HALOE wavelengths.	61
5.2	Interpolated central intensity values and estimated uncertainties at HALOE wavelengths.	68
5.3	Calculated flux and disk brightness temperatures with uncertainties at HALOE wavelengths.	69
6.1	Sunspot and photosphere relative intensity and calculated sunspot to photosphere intensity ratio.	85
6.2	Black-body temperature comparison of photosphere and sunspot	89

List of Figures

1.1	The structure of the Sun showing an exaggerated view of the photosphere. When compared to the Sun's radius (R_{\odot}) of 696,000 km, this is actually a very thin layer of only 300 to 400 km thickness.	6
1.2	The upper panels show the height in the solar atmosphere where radiation is formed for visible and infrared wavelengths. The altitudes are specified with reference to the $\tau_{\lambda=0.5\mu m} = 1$ level. The lower panels give the relative opacity contributions at this height over the same wavelength range. (Adapted from Vernazza, Avrett, and Loeser [2].)	9
1.3	Absorption of solar radiation by the Earth's atmosphere over infrared wavelengths from 1 to 15 μm . (Adapted from LaRocca [13].)	10
2.1	The definition of intensity.	16
2.2	Geometry of beam trajectory in slab of material where emission and absorption occur.	17
2.3	(a) A plane-parallel element bounded by surfaces τ_1 and τ_2 with $\tau_1 < \tau_2$ (b) A semi-infinite atmosphere where element boundaries are $\tau_1 = 0$ and $\tau_2 = \infty$	19
3.1	The HALOE instrument and its external components.	24
3.2	The spectral response of the HALOE instrument over the channels centered at wavelengths of 2.45, 2.80, 3.40, and 3.46 μm	26
3.3	The spectral response of the HALOE instrument over the channels centered at wavelengths of 5.26, 6.25, 6.60, and 9.85 μm	27
3.4	HALOE spatial response functions plotted in elevation to ± 2 arc min from the center of the IFOV at 2.45, 2.80, 3.40, and 3.46 μm	29
3.5	HALOE spatial response functions plotted in elevation to ± 2 arc min from the center of the IFOV at 5.26, 6.25, 6.60, and 9.85 μm	30
3.6	The Butterworth function, $B(t_k)$, illustrating the time delay effects in the HALOE signal.	32

4.1	Example of 2.45 μm raw solar scan data for one event. The relative intensity signal (solid line) in volts shows smooth variation over the disk and sharp discontinuities as the IFOV scans over the limb. The dotted line represents the FSSTOP diode values which increase as the IFOV scans toward the top limb and decrease as the IFOV moves towards the bottom limb.	38
4.2	Geometry of the scan chord on the solar disk.	40
4.3	The positions of the Gaussian quadrature points in the IFOV for the horizontal integration of the relative intensity at $\theta_i + \theta_j$	42
4.4	Diagram of the geometry used to calculate the angle from disk center, θ . The measured angle θ is the hypotenuse of the right triangle of sides given by $\Phi_{az} + \phi_k$ and $\theta_i + \theta_j$	43
4.5	An illustration of two conditions where IFOV function angles, $\theta_i + \theta_j$, near the limb have only a partial horizontal intensity contribution to the intensity convolved with the IFOV function. The intensity is found by integrating over the horizontal length that is on the disk, l	44
4.6	An example of raw solar scan data for an event that includes a sunspot. The 2.45 μm signal (solid line) in volts shows a small dip when the IFOV scans over a sunspot. The dotted line represents the FSSTOP diode values which increase as the IFOV moves toward the top limb and decrease as the IFOV moves towards the bottom limb.	49
4.7	The geometry of the projections of the disk coordinate system, the solar axis, the Earth's axis of rotation, and scan chord onto the observed solar disk. The angle ψ is measured between the projection of the Earth's rotation axis and the vertical diameter of the instrument. The calculated angle Ω is measured between the projection of the Earth's axis of rotation and the projection of the solar axis.	50
4.8	Coordinates of a sunspot measured in arc minutes along the scan path, θ_{spot} , and perpendicular to the scan path, ϕ_{spot}	52
4.9	A circle of radius R with its center located at θ_{spot} and ϕ_{spot} shown relative to the moving IFOV. A portion of the sunspot will be located within the IFOV at scan angles where the difference between θ_i and θ_{spot} is less than $2 + R$	55
5.1	HALOE solar scan positions relative to the solar disk. The shaded horizontal region indicates the coverage of the center of the scan chords for the sunrise events that scanned the solar equator. The IFOV is shown to scale on the lower left portion of the disk.	58

5.2	Weighted residuals (observed minus calculated) from the analysis of the solar equator data of May 4-6, 1994. In each plot the values on the vertical axis are normalized to unit central intensity. The position on the disk is measured along the scan path and is given in terms of the ratio of the observing angle from scan center, ϕ , to the angle from center to limb, ϕ_{\odot} . All fits match the experimental data to the digitization level (indicated by the dotted horizontal lines in each plot).	60
5.3	(a) The limb-darkening functions as calculated using the coefficients of Table 5.1. The order that the curves are labeled indicates their position in the plot. A single line indicates the limb-darkening functions at 3.40 and 3.46 μm , since they are indistinguishable at this scale. (b) HALOE relative intensity at selected wavelengths along with various other relative intensity data are plotted as a function of μ . In general, the line labels coincide with the order of the curves in the plot.	62
5.4	Relative intensity as a function of wavelength at three values of μ for both HALOE and other measurements. In general, good agreement exists between HALOE relative intensity and other data between 2 and 5 μm . Between 5 and 10 μm , however, HALOE relative intensities are lower than other values.	63
5.5	HALOE solar scan positions relative to the solar for two other relative intensity studies. The vertical shaded region indicates the coverage of the centers of the scan chords for the sunrise events used to analyze the relative intensity from pole-to-pole. The shaded region from the 45° NE limb to the -45° SW limb as seen by the instrument indicate the coverage of the scan chords for sunset events used to obtain diagonally measured relative intensity.	65
5.6	Center-to-limb relative intensity differences between results obtained from equator, pole-to-pole, and diagonal (from the 45° NE limb to the -45° SW limb) scans. The differences between the measured relative intensity, $I_{\lambda}^r(\mu)$, are given as a function of μ at the eight HALOE wavelengths. The line labels coincide with the order of the curves in the plot. All differences are less than the uncertainty of the relative intensity measurements.	66
5.7	Disk brightness temperature comparison between calculated HALOE results and the Engelke [46] VAL-M approximation. Good agreement exists except at the shortest two wavelengths of 2.45 and 2.80 μm	70
5.8	Temperature as a function of optical depth for all eight HALOE wavelengths and VAL-M at 2.5 and 10 μm . HALOE results at 9.85 μm and VAL-M at 10 μm compare very well. Calculated temperatures at 2.45 μm , however, are lower than those of VAL-M at 2.5 μm	72

6.1	HALOE solar scan positions and sunspot position during one event on August 19, 1992.	76
6.2	Positions of the two sunspots relative to the IFOV.	78
6.3	Residuals (observed minus calculated) from the analysis of measurements excluding the sunspot. Values on the vertical axis are normalized to unit central intensity. The positions of the residuals is specified by the angle measured along the scan path from scan path center. The standard deviation of the fit, σ_{fit} , indicates that all fits match the experimental data to the digitization level specified by the dotted horizontal line in each plot.	79
6.4	Differences between calculated photospheric relative intensity and measured relative intensity of the sunspots for positive scans. The positions are given as angles measured along the scan path from scan path center.	81
6.5	Differences between calculated photospheric relative intensity and measured relative intensity of the sunspots for negative scans. Positions are specified in arc minutes along the scan path from scan path center.	82
6.6	Residuals as a function of scan position at each HALOE wavelength after solving for sunspot parameters. All specified RMS values are within the associated digitization level.	84
6.7	Umbral to photosphere intensity ratio at eight HALOE wavelengths along with linear relations obtained from measurements by Albrechtsen <i>et al.</i> [18] at ten shorter wavelengths. The size of the HALOE data symbols is indicative of the uncertainty.	87
6.8	Sunspot temperatures calculated by Maltby <i>et al.</i> [17] from observations of Albrechtsen <i>et al.</i> [18] at ten wavelengths and HALOE values.	90
A.1	Geometry of a sunspot of radius R in the IFOV. The sunspot center is given by θ_{spot} measured on the scan chord and ϕ_{spot} measured horizontally from the chord. The angular distance δ represents the vertical displacement of the sunspot center from the horizontal integration. The length of the chord through the sunspot circle on the horizontal at $\theta_i + \theta_j$ is l and the width of the IFOV is L	97

Abstract

Solar data from the Halogen Occultation Experiment (HALOE) were analyzed to determine the center-to-limb relative intensity and the vertical temperature profile for the quiet and active Sun over wavelengths from 2.4 to 10 μm . An algorithm was developed that modeled the HALOE instrument during data acquisition. It incorporated a nonlinear least squares procedure to obtain relative intensity information across the solar disk. Data obtained from limb-to-limb scans across the solar equator on days of very low activity in May 1994 were analyzed to obtain coefficients of a function describing the relative intensity from center-to-limb. Relative intensities produced by the limb-darkening functions were precise to 0.1% (2 standard deviations) from the center to 0.25 arc min from the limb. Once found, the coefficients to the limb-darkening function were used to calculate two temperature quantities: the brightness temperature from the flux, $T_b^{disk}(\lambda)$, and the temperature as a function of monochromatic optical depth, $T(\tau_\lambda)$. These quantities were normalized using published central intensity values and compared to a semi-empirical model of the photosphere. In general, the calculated temperature quantities were in good agreement with the model results. The largest differences occur between 2.4 and 3 μm and suggest that the central intensities used in this spectral region are low.

HALOE solar data were also investigated to obtain the intensity of a sunspot relative to the photosphere. A nonlinear least squares method was used to analyze the HALOE measurements of August 19, 1992 and retrieve relative intensity information on a sunspot. A one-component sunspot model was adopted where the spot was modeled as a circle of constant relative intensity. This model proved to be sufficient to fit the measurements of the photosphere and sunspot to the digitization level of the instrument at each wavelength. Sunspot/photosphere intensity ratios were calculated at each wavelength with a standard deviation of 2%. These were compared with previous measurements at shorter wavelengths from 0.387 to 2.35 μm . Although there is a larger than anticipated gap between the previous value at 2.35 μm and the HALOE ratio value at 2.45 μm , the two data sets exhibit the same general trend of larger ratio values with increasing wavelengths. By using the available intensity information, the photospheric and sunspot temperature were calculated at each HALOE wavelength. HALOE sunspot temperatures show a slight decrease with lengthening wavelengths. From 1.67 to 2.35 μm , the previous measurements exhibit a steep drop in sunspot temperature which is not supported by HALOE values. Consideration of terrestrial atmospheric effects in the previous data could explain this discrepancy.

**Solar Infrared Relative Intensity Data From The
Halogen Occultation Experiment**

Chapter 1

Introduction

Since the beginning of civilization, humans have viewed the Sun with curiosity and fascination. The Sun plays an enormous role in our lives and has influenced our philosophical development as well as scientific thought. Early cultures noted the Sun's regular, unchanging behavior and tended to think of it as an enslaved individual. Later, the Sun was elevated to deity status and its characteristics explained through myths and legends. With the rise of the Greeks came the first attempt at describing the universe using physical laws. The powerful philosopher, Aristotle, insisted that the Sun was perfect, and used scientific reasoning to validate his philosophical beliefs. His views on the universe influenced western culture and thought into the 17th century.

The invention of the telescope in the early 1600s contributed to significant observations and discoveries that profoundly changed our view of the universe. Small, dark marks on the Sun had been noticed centuries before with the unaided eye, but Galileo and his contemporaries are credited with making the first telescopic observations of the Sun. They determined that these marks on the Sun's disk, what we now call sunspots, were truly solar in nature. By continuously observing the movement of sunspots as well as bright regions

(called faculae) across the disk, Galileo determined that the Sun rotated. These discoveries were a blow to Aristotle's concept of a perfect solar sphere and helped usher in a new age of scientific thought.

Over the last few centuries, solar investigations have had a tremendous impact on our understanding of the physical nature of the universe. Observations of the Sun and the planets helped Newton formulate a description of gravity that accounts for Kepler's laws and explains the motion of the planets. Fraunhofer used the newly invented spectroscope to measure the positions of hundreds of dark lines seen in the solar spectrum. Later, by discovering how light is emitted and absorbed in solid and gaseous bodies, Kirchhoff was able to show from Fraunhofer's work that the Sun and Earth shared common elements. His work provided the evidence to support the idea that the Sun is a star and helped develop the notion of a universe that was homogeneous in composition.

Our star is seen as a link to the rest of the universe, but it is also viewed in terms of its intrinsic ties to conditions here on Earth. For example, it is thought that variations in solar activity might produce significant climatic changes. Very few sunspots were seen during a period from 1645 to 1715 known as the Maunder Minimum. This coincides with times of record low temperatures in Europe, often referred to as the Little Ice Age, and severe drought in the western United States. The composition of the Earth's atmosphere is directly influenced by the light and energetic particles emitted by the Sun. In the terrestrial atmosphere, solar energy helps sustain the particular chemical composition responsible for heat transfer. Gases, such as water vapor and carbon dioxide, interact with solar energy and block the radiated energy of the Earth producing a general warming of the Earth. This process is referred to as the Greenhouse Effect. In the Earth's upper atmosphere, energetic particles emitted by the Sun cause the ionization of gas molecules. These electrically charged ions and electrons become trapped in the Earth's magnetic field and form a layer in the

atmosphere referred to as the ionosphere. The ionosphere reflects radio waves, and its diurnal variation as well as its variation with solar activity greatly affects global radio communications.

The Sun also has a direct effect on the Earth's lifeforms. On the surface of the Earth, life itself is supported by the necessary heat provided by the Sun. Vision has evolved over time to detect the solar radiation transmitted by the Earth's atmosphere. For humans, exposure to ultraviolet (UV) sunlight activates production of vitamin D. Solar radiation is beneficial to terrestrial life, but it can also be harmful. Sunlight initiates chemical reactions between hydrocarbons and oxygen producing photochemical smog, which contains eye irritants and other dangerous contaminants. In the ozone layer of the atmosphere, most of the highly energetic UV radiation from the Sun is absorbed in reactions that create and destroy ozone. The portion of solar UV that makes it through the ozone layer tans the body's skin; however, long exposure to UV is thought to increase the risk of skin cancer.

Appropriately enough, the Sun is viewed from many perspectives. Man looks to the Sun to help provide answers to questions about the the physical nature of the universe as well as the understanding of life itself. Since the Sun has been observed for centuries, a large base of information exists that is still a source of investigation; however, our star is not completely understood. Its variable nature and dramatic phenomena are frequently a source of surprise and excitement. The aim of the work presented in this dissertation is to provide further information that will increase our understanding of the Sun.

1.1 The Sun - A General Description

The Sun has remained relatively unchanged from its present state for the last 4 to 5 billion years and it is estimated to continue like this for another 5 billion years. Compared to other stars, the Sun is about average in mass, size, surface temperature, and chemical composition. The energy transport mechanism varies throughout the Sun and leads to a division of the solar atmosphere into regions. In the core at the center of the Sun, thermonuclear reactions convert hydrogen into helium. The energy created in the core is transported through the rest of the solar interior to the surface through various complicated processes. Above the solar interior there are three regions beginning with the photosphere, then the chromosphere, and finally the outermost region called the corona. These are illustrated in Figure 1.1. The regions are rather distinct in character, yet each is intricately tied to the others. Studying one particular region provides valuable information about the overall workings of the solar sphere.

The Sun's power plant is found in its core which extends to about 0.3 of the solar radius (R_{\odot}). Since we cannot observe the core directly, indirect methods are used to calculate what is taking place at the center of the Sun. Evidence suggests that the temperature in the core is about 15.5×10^6 K. At this temperature, hydrogen atoms combine to form helium. Thermonuclear fusion of hydrogen into helium is described by the proton-proton chain whereby four hydrogen atoms are converted to one helium atom plus other particles. The mass difference, m , between the four hydrogen and the resulting helium atom and other particles is converted into energy, E , according to Einstein's relation

$$E = mc^2, \quad (1.1)$$

where c is the speed of light. The energy is transported outwards via photons to $0.7R_{\odot}$ through the process of radiative diffusion. From this point, convection is the dominant

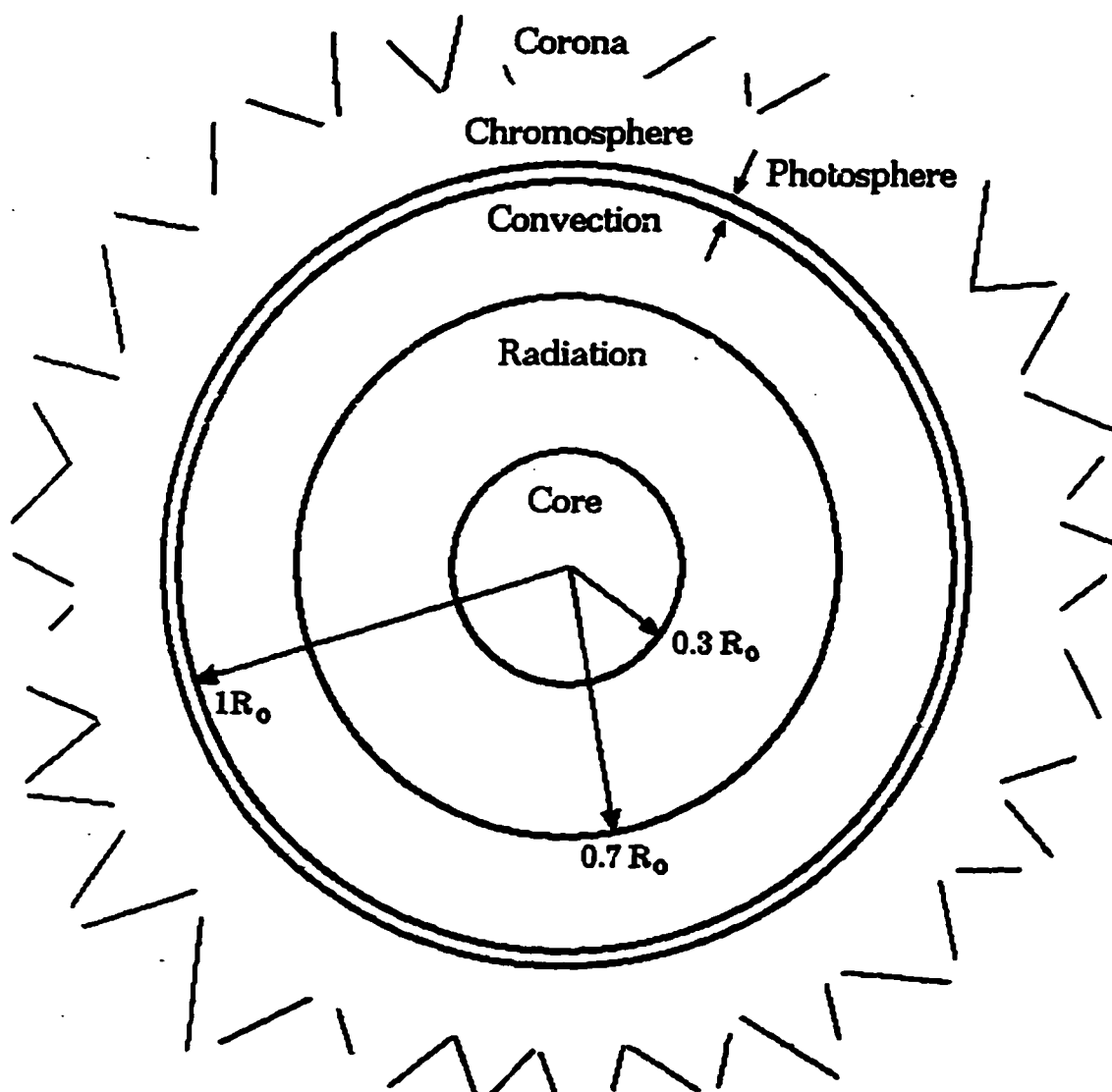


Figure 1.1: The structure of the Sun showing an exaggerated view of the photosphere. When compared to the Sun's radius (R_{\odot}) of 696,000 km, this is actually a very thin layer of only 300 to 400 km thickness.

transport medium to the surface. This description of the solar interior is widely accepted by solar scientists; however, experiments to detect neutrinos created during the proton-proton cycle have detected too few for this model [1].

The photosphere is a thin layer directly above the convection zone and is commonly called the Sun's surface. Most visible light emitted into space by the Sun originates in this region; hence the name photosphere or 'sphere of light.' Compared to the Sun's radius of 696,000 km, this is a very thin layer of only 300 to 400 km thickness, yet from this region, more than 95% of the Sun's light is emitted. Besides visible radiation, light of infrared wavelengths also comes from the photosphere. Since this work pertains to the photosphere, a more detailed description of this layer is given in subsequent sections.

The region above the photosphere can be seen prominently during a total solar eclipse. At this time, the bright photosphere is blocked by the Moon and the 2000-km-thick reddish-pink layer called the chromosphere or 'sphere of color' can be seen. The color of the chromosphere is attributed to one of the brightest emission lines in its spectrum, the Balmer line H_{α} at 656.3 nm. From the base of the chromosphere outward, temperatures remain comparable to those of the photosphere. In the upper chromosphere, however, temperatures increase dramatically to 1 to 2 million K. Why this large change in temperature occurs is still a subject of debate.

The corona is the outermost region of the solar atmosphere and extends from the top of the chromosphere several million kilometers. It maintains temperatures in the million-Kelvin range, and thus produces radiation at extreme ultraviolet (EUV) and X-ray wavelengths. Spectacular eruptions of plasma as streamers or in closed loops are observed in the corona and associated with underlying active regions. Eventually the corona becomes the solar wind, which consists of high-speed protons and electrons streaming away from the Sun.

1.2 The Photosphere

Much of what is known about the Sun comes from observations of the photosphere and yet it is by far the smallest layer of the Sun. The operational boundary definitions of the photosphere are given in terms of the continuum optical depth, τ_λ , but are somewhat arbitrary since optical depth varies with wavelength. The continuum optical depth describes how the intensity of light decreases as it passes through absorbent material.

$$\frac{I_\lambda}{I_{\lambda_0}} = e^{-\tau_\lambda}, \quad (1.2)$$

Here I_{λ_0} is the original intensity, and I_λ is the intensity at optical depth τ_λ . The λ subscripts are to emphasize the wavelength dependence of this relationship which is shown in Figure 1.2. Typically, the middle of the photosphere is defined as the layer where $\tau_\lambda = 1$ for $\lambda = 0.5 \mu\text{m}$, with the understanding that the photosphere extends 100 to 200 kilometers above and below this level. In the remaining portion of this section, a description of the photosphere is given which lays the foundation for the work of this thesis.

1.2.1 Wavelengths of Observations

There have been solar observations recorded in virtually every wavelength region of the electromagnetic spectrum. In the photosphere, a small layer is responsible for producing visible wavelength radiation. Figure 1.2 illustrates an important feature of solar near infrared radiation. From the visible up to about $1.6 \mu\text{m}$, radiation is emitted at greater depths relative to the layer producing visible light. At $1.6 \mu\text{m}$, the opacity is at a minimum, and radiation comes from the deepest observable layer. Solar radiation of wavelengths longward of $1.6 \mu\text{m}$ is emitted from subsequently higher and higher layers of the photosphere. Therefore, observations of solar infrared radiation can be used to a great advantage as a probe of the structure of the photosphere. This is a troublesome condition for ground-

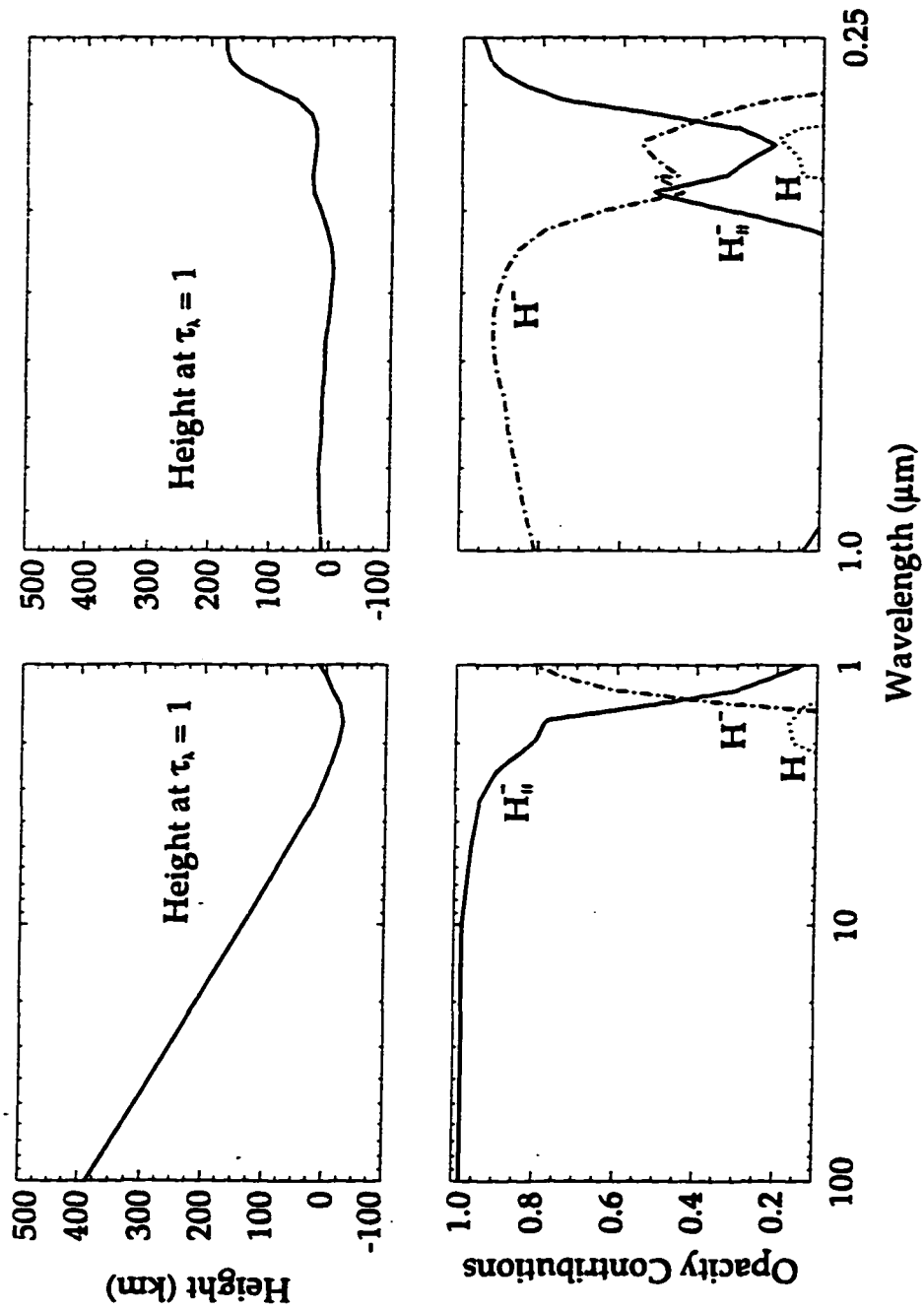


Figure 1.2: The upper panels show the height in the solar atmosphere where radiation is formed for visible and infrared wavelengths. The altitudes are specified with reference to the $\tau_{\lambda=0.5\mu\text{m}} = 1$ level. The lower panels give the relative opacity contributions at this height over the same wavelength range. (Adapted from Vernazza, Avrett, and Loeser [2].)

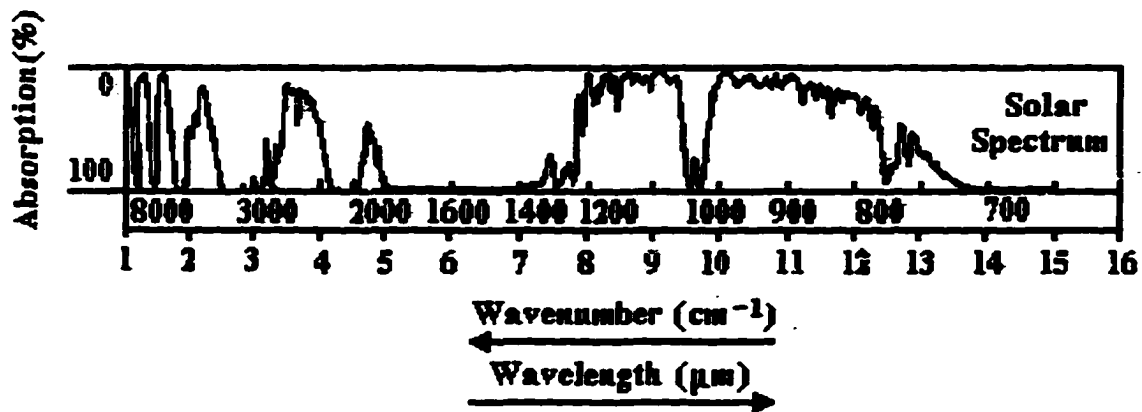


Figure 1.3: Absorption of solar radiation by the Earth's atmosphere over infrared wavelengths from 1 to 15 μm . (Adapted from LaRocca [13].)

based observations, because the Earth's atmosphere is rather opaque to infrared radiation as shown in Figure 1.3. The terrestrial atmosphere is transparent through broad spectral windows to visible and infrared radiation up to 2.4 μm , and numerous observations are reported over this wavelength range [3–8]. This is not the case for wavelengths longward of 2.4 μm where measurements are hindered by absorbers in the terrestrial atmosphere, lesser solar intensity, and less sensitive detectors. For wavelengths from 2.4 to 10 μm in particular, the spectral features of atmospheric water, carbon dioxide, and methane block all but a few narrow opacity windows. Measurements in these windows are possible but must require large corrections for atmospheric effects. [9–12]

Exoatmospheric solar experiments have been proposed that would eliminate the problems associated with viewing infrared wavelengths through the Earth's atmosphere and allow for a comprehensive study of the photosphere [14, 15]. The Halogen Occultation Experiment (HALOE) on the Upper Atmosphere Research Satellite (UARS) is a solar occultation experiment that has been accumulating solar data at eight infrared wavelengths

since October 1991 [16]. Although the objective of HALOE is to obtain information about mixing ratios of gases in the Earth's atmosphere, exoatmospheric scans of the Sun are performed to obtain relative intensity measurements for calibration purposes. These measurements provide new information on center-to-limb relative intensity in spectral bands centered at wavelengths of 2.45, 2.80, 3.40, 3.46, 5.26, 6.25, 6.60, and 9.85 μm . Analyses of these data provide an opportunity to more completely describe the lower photosphere from approximately the base to 150 km above the reference level of $\tau_{\lambda=0.5\mu\text{m}} = 1$.

1.2.2 The Quiet Photosphere

The quiet photosphere refers to the solar surface devoid of sunspots and active regions. Early observations of the solar disk showed that the edges appeared darker than the center of the disk. This is referred to as limb darkening and is due to a change in perspective as the curved solar surface is viewed. The perceived depth seen in the photosphere decreases as an observer's line of sight becomes more skewed towards the limb. Therefore, the observed light from the limbs actually comes from higher, cooler layers.

Since limb darkening is due to the large temperature gradient of the photosphere, analysis of limb darkening at near infrared wavelengths provides a direct technique for learning about the temperature structure as a function of depth. The behavior of center-to-limb relative intensity is described by a limb-darkening function, which is typically a polynomial having wavelength dependent coefficients. For visible and infrared wavelengths up to 2.4 μm , these functions are available in several forms [3, 5–7]. One in particular was used by Pierce and Waddell [5], who found coefficients for their limb-darkening function at wavelengths from 0.31 to 2.4 μm [5]. This is one of the few functions for which limb-darkening information exists for wavelengths longer than 2.4 μm . Allen [3] listed this

function and its coefficients over a wavelength range from 0.2 to 10 μm . In and near the range of HALOE wavelengths, Allen listed coefficients to the Pierce and Waddell limb-darkening function at only wavelengths of 2, 3, 5, and 10 μm .

1.2.3 Sunspots

Sunspots are some of the more interesting features seen on the solar surface. With the invention of the telescope came a concerted effort to regularly track sunspots, and analysis of these records indicates that their number and position on the Sun behave in a periodic way. Through telescopic observations, it was also learned that sunspots exhibit a general structure and are linked to neighboring phenomena. The sunspot and other features around it make up an area called an active region. Within an active region, it is not uncommon to find two larger spots aligned in latitude. The leading spot is forward of the trailing spot relative to the Sun's rotation. Although the features of active regions vary with time, they might include any number of sunspots and cloud-like bright regions called faculae.

Although sunspots vary in size and appearance, they typically consist of a dark central core called the umbra which may be surrounded by a slightly less-dark border called the penumbra. Visible and infrared spectral information indicates that sunspots are more than 1000 K cooler than the surrounding photosphere, and hence they appear dark in contrast. Although the specific mechanism that causes sunspots is still unknown, it has been found that they are a manifestation of the Sun's magnetic field. In fact, the magnetic field of a leading sunspot is found to be of opposite polarity as that of its trailing sunspot. Within the sunspot, intense magnetic activity inhibits the motion of the photospheric plasma which constricts the flow of energy from the convection layer directly below the photosphere. Due to this, gases in the sunspot cool, and they appear dark when observed because they are cooler than the surrounding photosphere.

A physical description of sunspot structure and behavior can provide useful information needed for understanding the Sun. As is the case in limb darkening, analysis of infrared sunspot intensities can provide useful information on its temperature structure. Ground-based observations of sunspot intensity as a function of position on the disk have been made for visible and infrared wavelengths up to $2.4 \mu\text{m}$ [17–19]. Sunspot intensities at wavelengths longward of $2.4 \mu\text{m}$ are difficult to obtain due to interference by the terrestrial atmosphere.

1.3 Solar Models

Unfortunately, there is no method to probe the structure of the Sun first hand. Remote solar observations have provided important information regarding the physical nature of the Sun; however, many basic questions pertaining to unseen solar processes can only be answered by developing theory that produces values that match what is observed. Models attempt to provide specific information on the temperature, density, and velocity structure of the solar atmosphere. In so doing, they increase the general understanding of the basic physical mechanism that produces the observed data. The information presented in this work is useful for the construction of models as well as a test of their validity [20].

Limb darkening as a function of wavelength has served as the principal tool in building photospheric models. From the intensity distribution across the Sun, models are able to map the temperature as a function of depth. The temperature structure of the solar atmosphere provides clues to the local physical state and serves as a good boundary condition for the processes taking place in the solar interior. Vernazza, Avrett, and Loeser assembled available solar data and developed a semiempirical model of the solar atmosphere [2]. Specifically, their model M (henceforth VAL-M) produces a temperature structure over the entire photosphere. Two of the temperature quantities given by the model are the disk

brightness temperature as a function of wavelength and the temperature as a function of optical depth. This model is used as a basis for comparison to the present work.

Intensity measurements of sunspots have led to a description of their temperature structure through semiempirical models. A sunspot umbral model has been given by Maltby, *et al.* [17], which is based upon center-to limb measurements of the umbra/photosphere intensity ratios over wavelengths from 0.387 to 2.35 μm . The measurements of the present work extend the wavelength coverage of available data to 10 μm .

Chapter 2

Radiative Transfer

This chapter sets forth portions of radiative transfer theory that have been collected from introductory solar physics books and authoritative articles [2, 5, 21–24]. The intent of the following discussion is to theoretically describe the solar photosphere where the energy observed by HALOE is produced. The relatively high density of the photosphere makes assumptions possible which reduce the complexity of the discussion. The final derivations will show how limb-darkening measurements can be used to reveal solar temperature information.

Radiative transfer describes the flow of electromagnetic energy and is characterized in terms of quantities such as intensity and flux. The intensity is defined as the average energy per unit time per unit cross-section area and is pictorially represented in Figure 2.1. Consider an element of area da with normal vector \hat{n} . Radiative energy per unit time or power, dP_λ , with wavelength interval $d\lambda$ passes uniformly through da . The intensity of this radiation, $I_\lambda(\theta)$, is defined as the power, dP_λ , passing through da in the direction \hat{s} into a solid angle $d\omega$.

$$dP_\lambda = I_\lambda(\theta) da \cos \theta d\omega d\lambda. \quad (2.1)$$

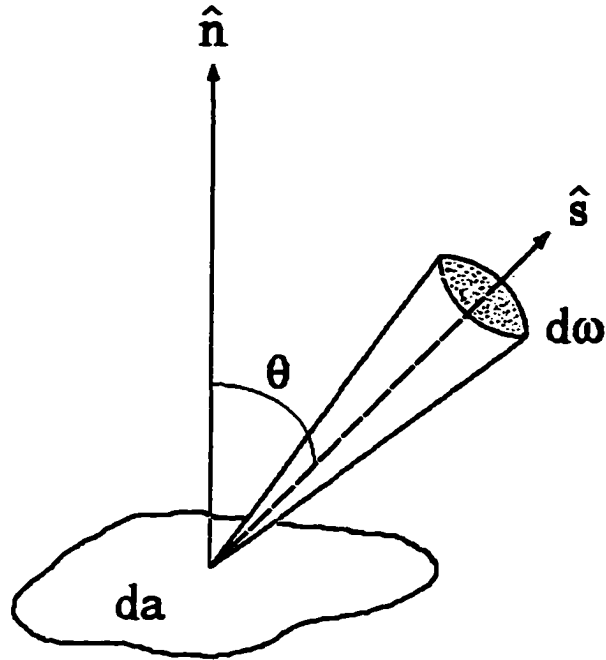


Figure 2.1: The definition of intensity.

Here P_λ has the units of Watts(W) for intensity in units of $W \text{ cm}^{-2} \mu\text{m}^{-1} \text{ sr}^{-1}$. Since the energy flow is uniform, the intensity is assumed to be azimuthally symmetric about \hat{n} .

The net outward flux, F_λ , is the net intensity in all outward directions from da and is calculated by summing the intensity over the total solid angle of 2π sr.

$$F_\lambda = \int I_\lambda(\theta) \cos \theta d\omega. \quad (2.2)$$

The solid angle can be written in terms of θ and ϕ which is the azimuth angle corresponding to a rotation about \hat{n} .

$$d\omega = \sin \theta d\theta d\phi. \quad (2.3)$$

Substituting this into Equation 2.2 gives an explicit form for the flux.

$$F_\lambda = \int_0^{2\pi} d\phi \int_0^{\pi/2} I_\lambda(\theta) \cos \theta \sin \theta d\theta. \quad (2.4)$$

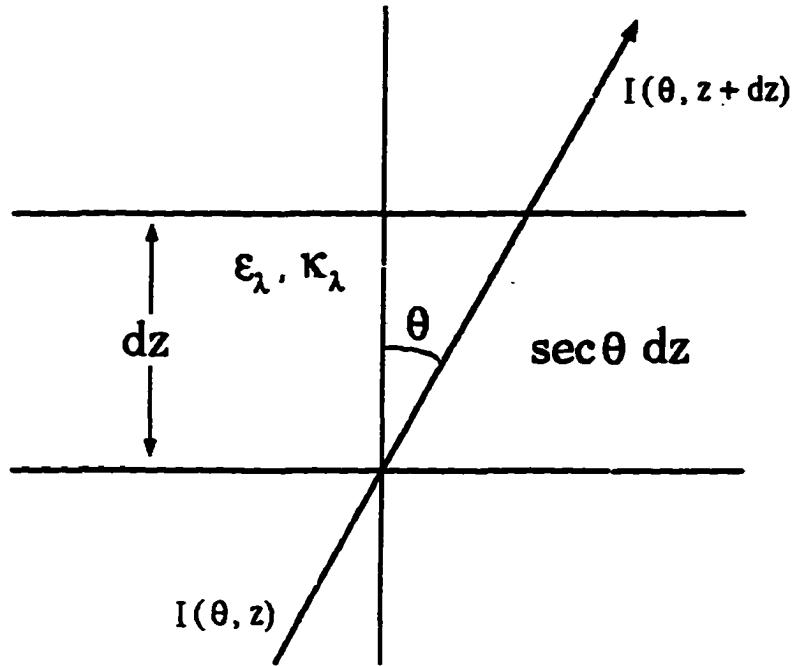


Figure 2.2: Geometry of beam trajectory in slab of material where emission and absorption occur.

$$F_\lambda = 2\pi \int_0^{\pi/2} I_\lambda(\theta) \cos \theta \sin \theta d\theta. \quad (2.5)$$

Typically the integral is simplified further by making the substitution $\mu = \cos \theta$ so that the flux becomes

$$F_\lambda = 2\pi \int_0^1 I_\lambda(\mu) \mu d\mu. \quad (2.6)$$

For intensity in units of $W \text{ cm}^{-2} \mu\text{m}^{-1} \text{ sr}^{-1}$, the flux will have units of $W \text{ cm}^{-2} \mu\text{m}^{-1}$.

Now consider the plane-parallel slab of thickness dz that contains a medium in which emission and absorption can occur (see Fig. 2.2). Two defined quantities of the medium $\epsilon_\lambda(z)$ and $\kappa_\lambda(z)$ are respectively the monochromatic emission and absorption coefficients per centimeter of path (units of cm^{-1}). The change in intensity of a beam passing through

the element at an angle θ to the normal is the difference between absorption and emission.

$$I_\lambda(\theta, z + dz) - I_\lambda(\theta, z) = [\epsilon_\lambda(z) - \kappa_\lambda(z)I_\lambda(\theta, z)] \sec \theta dz. \quad (2.7)$$

The left side can be reduced to $dI_\lambda(\theta, z)$.

$$\cos \theta \frac{dI_\lambda(\theta, z)}{dz} = [\epsilon_\lambda(z) - \kappa_\lambda(z)I_\lambda(\theta, z)]. \quad (2.8)$$

The optical depth, τ_λ gives a measure of the opacity of the medium and its definition allows it to serve as the new depth coordinate in place of z .

$$d\tau_\lambda = -\kappa_\lambda dz. \quad (2.9)$$

The negative sign in this relation indicates that the optical depth increases with depth into the medium in which z is taken to increase outward. Substituting this expression into Equation 2.8 gives the standard form of the radiative transfer equation.

$$\mu \frac{dI_\lambda}{d\tau_\lambda} = I_\lambda - S_\lambda, \quad (2.10)$$

Introduced in this equation is a quantity called the source function, $S_\lambda = \epsilon_\lambda/\kappa_\lambda$, which has the same units as intensity. Note that the emergent intensity is completely specified by the source function rather than ϵ_λ or κ_λ individually.

The standard radiative transfer equation can be solved for the photosphere by initially considering a plane-parallel element bounded by surfaces τ_1 and τ_2 with $\tau_1 < \tau_2$ as illustrated in Figure 2.3a. A total differential form for the equation can be obtained by multiplying the expression by $e^{-\frac{\tau}{\mu}}$.

$$\mu \frac{dI_\lambda}{d\tau_\lambda} e^{-\frac{\tau}{\mu}} - I_\lambda e^{-\frac{\tau}{\mu}} = -S_\lambda e^{-\frac{\tau}{\mu}}. \quad (2.11)$$

$$\mu \frac{d(I_\lambda e^{-\frac{\tau}{\mu}})}{d\tau_\lambda} = -S_\lambda e^{-\frac{\tau}{\mu}}. \quad (2.12)$$

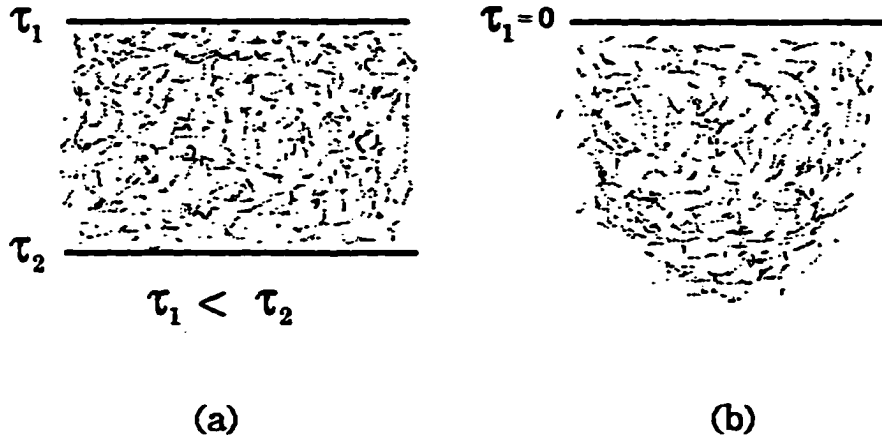


Figure 2.3: (a) A plane-parallel element bounded by surfaces τ_1 and τ_2 with $\tau_1 < \tau_2$ (b) A semi-infinite atmosphere where element boundaries are $\tau_1 = 0$ and $\tau_2 = \infty$.

Integrating this expression over the slab gives the emergent intensity at the τ_1 surface.

$$\mu \int_{\tau_1}^{\tau_2} d(I_\lambda e^{-\frac{\tau}{\mu}}) = - \int_{\tau_1}^{\tau_2} S_\lambda e^{-\frac{\tau}{\mu}} d\tau. \quad (2.13)$$

$$I_\lambda(\tau_2, \mu) e^{-\frac{\tau_2}{\mu}} - I_\lambda(\tau_1, \mu) e^{-\frac{\tau_1}{\mu}} = - \frac{1}{\mu} \int_{\tau_1}^{\tau_2} S_\lambda e^{-\frac{\tau}{\mu}} d\tau. \quad (2.14)$$

$$I_\lambda(\tau_1, \mu) = I_\lambda(\tau_2, \mu) e^{-\frac{\tau_2 - \tau_1}{\mu}} + \frac{1}{\mu} \int_{\tau_1}^{\tau_2} S_\lambda e^{-\frac{\tau - \tau_1}{\mu}} d\tau. \quad (2.15)$$

The photosphere can be viewed in terms of a semi-infinite atmosphere where $\tau_1 = 0$ and $\tau_2 = \infty$ as shown in Figure 2.3b. In this case the emergent intensity can be expressed in

terms of an integral of the source function.

$$I_{\lambda}(0, \mu) = \frac{1}{\mu} \int_0^{\infty} S_{\lambda} e^{-\frac{\tau_{\lambda}}{\mu}} d\tau. \quad (2.16)$$

What is needed to complete this calculation is a suitable source function.

For conditions where a radiative medium is in thermodynamic equilibrium, the source function is found to be a function of temperature. Assume that material in an adiabatic cavity of uniform temperature with perfectly absorbing and emitting walls is in equilibrium. Under these circumstances, all energy emitted must be absorbed; therefore, the temperature must be uniform and the intensity is isotropic. As noted by Kirchhoff, the source function is independent of the composition of the material and depends only upon the temperature and wavelength.

$$S_{\lambda} = \epsilon_{\lambda} / \kappa_{\lambda} = B_{\lambda}(T). \quad (2.17)$$

Here B_{λ} is the Planck function, and it has the same units as intensity.

$$B_{\lambda}(T) = \frac{2\pi hc^2}{\lambda^5} \frac{1}{\exp(hc/k\lambda T) - 1}. \quad (2.18)$$

The previous discussion can be applied to the photosphere and leads to a great simplification of the radiative transfer problem. In the photosphere the gas density is such that most photons are absorbed and thermalized before traveling a distance over which there is a significant temperature change. The radiation field is in local thermodynamic equilibrium (LTE) with the local temperature of the gas. So for the photosphere, the source function is well represented by the Planck function.

A description of photospheric intensity follows from the solution of Equation 2.16 after replacing the source function with the Planck function, $S_{\lambda} = B_{\lambda}$.

$$I_{\lambda}(0, \mu) = \frac{1}{\mu} \int_0^{\infty} B_{\lambda}(\tau_{\lambda}) e^{-\frac{\tau_{\lambda}}{\mu}} d\tau, \quad (2.19)$$

The relative intensity, $I_{\lambda}^*(0, \mu)$, is found by normalizing this equation to the absolute central intensity, $I_{\lambda}(0, 1)$.

$$I_{\lambda}^*(0, \mu) = \frac{I_{\lambda}(0, \mu)}{I_{\lambda}(0, 1)} = \frac{1}{\mu} \int_0^{\infty} B_{\lambda}^*(\tau_{\lambda}) e^{-\frac{\tau_{\lambda}}{\mu}} d\tau_{\lambda}. \quad (2.20)$$

In this expression, $B_{\lambda}^*(\tau_{\lambda}) = B_{\lambda}(\tau_{\lambda})/I_{\lambda}(0, 1)$ is the normalized Planck function.

The relative intensity, $I_{\lambda}^*(0, \mu)$, in Equation 2.20 can be found using limb-darkening measurements. If $B_{\lambda}^*(\tau_{\lambda})$ can be represented by some analytical formula containing expansion coefficients, then $I_{\lambda}^*(0, \mu)$ can be calculated in terms of these coefficients. Pierce and Waddell used the following expression for the normalized Planck function [5].

$$B_{\lambda}^*(\tau_{\lambda}) = \frac{B_{\lambda}(\tau_{\lambda})}{I_{\lambda}(0, 1)} = a_{\lambda} + b_{\lambda} \tau_{\lambda} + c_{\lambda} E_2(\tau_{\lambda}). \quad (2.21)$$

Here a_{λ} , b_{λ} , and c_{λ} are numerical coefficients and $E_2(\tau_{\lambda})$ is the exponential integral of order

2. The exponential integral is given by

$$E_n(z) = \int_1^{\infty} \frac{e^{-zt}}{t^n} dt \quad (n = 0, 1, 2, \dots; \Re z > 0) \quad (2.22)$$

and can be calculated numerically using series expansions [25]. Substituting Equation 2.21 into Equation 2.20 and integrating gives

$$I_{\lambda}^*(0, \mu) = \frac{I_{\lambda}(0, \mu)}{I_{\lambda}(0, 1)} = a_{\lambda} + b_{\lambda} \mu + c_{\lambda} [1 - \mu \ln(1 + \mu^{-1})]. \quad (2.23)$$

This equation describes the relative intensity as a function of μ , and its coefficients can be found by least-squares fitting to limb-darkening observations. Notice that at disk center ($\mu = 1$), Equation 2.23 becomes

$$1 = a_{\lambda} + b_{\lambda} + c_{\lambda} [1 - \ln 2]. \quad (2.24)$$

This is particularly useful in simplifying the fitting procedure as explained in Chapter 4.

After the coefficients to the limb-darkening function are obtained, they can be used in Equation 2.21 to derive the temperature as a function of monochromatic optical depth,

$T(\tau_\lambda)$. The combination of Equation 2.18 with Equation 2.21 gives an expression that can be solved for temperature as a function of optical depth, $T(\tau_\lambda)$.

$$\frac{2\pi hc^2}{\lambda^5} \frac{1}{\exp(hc/k\lambda T) - 1} = I_\lambda(0, 1) [a_\lambda + b_\lambda \tau_\lambda + c_\lambda E_2(\tau_\lambda)]. \quad (2.25)$$

Absolute calculations of $T(\tau_\lambda)$, however, depend upon the availability of the central intensity value, $I_\lambda(0, 1)$.

Another temperature quantity, the disk brightness temperature $T_b^{disk}(\lambda)$, gives a measure of the Sun's temperature as compared to a same-sized black body emitting radiation of the same intensity and wavelength. The values of $T_b^{disk}(\lambda)$ can be calculated from flux values, which are obtained from limb-darkening coefficients. The flux at 1 AU (1 AU is the average distance between the Sun and the Earth) is found by integrating the intensity, $I_\lambda(0, \mu)$.

$$F_\lambda = 2\pi r_\odot^2 \int_0^1 I_\lambda(0, \mu) \mu d\mu. \quad (2.26)$$

The quantity r_\odot is the solar radius expressed in AU and $I_\lambda(0, \mu)$ can be represented by the absolute central intensity and the limb-darkening coefficients.

$$I_\lambda(0, \mu) = I_\lambda(0, 1) [a_\lambda + b_\lambda \mu + c_\lambda [1 - \mu \ln(1 + \mu^{-1})]]. \quad (2.27)$$

The calculation of a disk brightness temperature from the computed flux proceeds under the assumption of LTE. For a given flux value, the disk brightness temperature, $T_b^{disk}(\lambda)$, is defined from an equation relating the flux to the Planck function.

$$F_\lambda = B_\lambda(T_b^{disk}). \quad (2.28)$$

Upon substitution of the explicit form of the Planck function given by Equation 2.18 and multiplying the constants, $T_b^{disk}(\lambda)$ can be represented as a function of the flux.

$$T_b^{disk}(\lambda) = \frac{14388}{\lambda \ln\left[\left(\frac{0.80978}{\lambda^5 F_\lambda}\right) + 1\right]}. \quad (2.29)$$

This expression gives T_b^{disk} in K for λ in μm and F_λ in $\text{W cm}^{-2} \mu\text{m}^{-1}$.

Chapter 3

Instrument And Observing Information

The Halogen Occultation Experiment (HALOE) on the Upper Atmosphere Research Satellite (UARS) was launched by the Space Shuttle Discovery on September 12, 1991 and began acquiring scientific data on October 11, 1991 [16]. It has been recording data regularly from that time up to the present. The instrument is depicted in Figure 3.1. HALOE is a solar occultation experiment designed to measure the distribution of temperature and mixing ratios of constituents in the Earth's atmosphere as a function of pressure. Its data have provided important information regarding the composition of the terrestrial atmosphere as well as the physical processes and chemical reactions occurring there (see for example Russell *et al.* [26]). Although this is its primary objective, HALOE also records relative intensity measurements of the Sun. These data are unique because they are exoatmospherically acquired measurements of solar infrared radiation between 2.45 and 10 μm . Ground-based solar observations at these wavelengths are extremely difficult to obtain because the Earth's atmosphere is partially opaque to infrared radiation (see Figure 1.3).

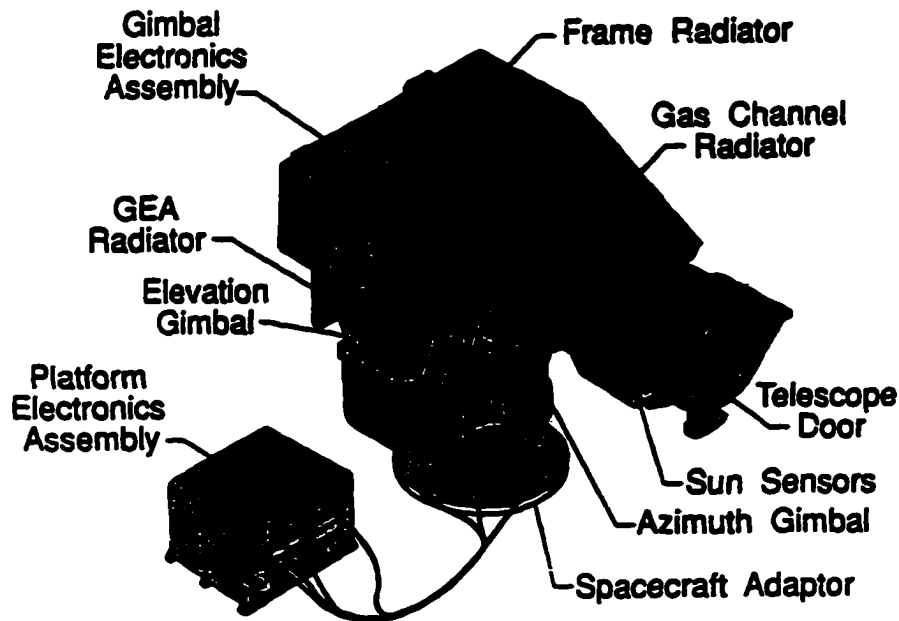


Figure 3.1: The HALOE instrument and its external components.

HALOE orbits the Earth on UARS at an altitude of 585 km and an inclination to the equator of 57° . HALOE is an occultation experiment and records science data twice each orbit during periods in which the Sun rises or sets on its horizon. There are typically fifteen sunrise and fifteen sunset events daily, each having a period in which the instrument performs exoatmospheric solar scans. During this time, HALOE moves its instrument field of view (IFOV) across the disk ten times in a direction perpendicular to the limb of the Earth at a rate of 2.16 arc minutes per second. During this time, it records both science and instrument information several times every 1.024 seconds. Data recorded 8 times during 1.024 seconds are referred to as 8 Hz data and those sampled 64 times are called 64 Hz data.

The IFOV has dimensions of 2 arc min perpendicular to the limb and 6.12 arc min parallel to the Earth's limb. The instrument simultaneously records relative intensity in eight spectral bands centered at wavelengths between 2.45 and 9.85 μm . Since this data is obtained at a rate of 8 Hz, over sampling (relative to the IFOV) is greater than a factor of seven. Measurements are obtained as voltages and recorded digitally with a digitization of 0.00244 volts and a signal at the center of the solar disk of approximately 3 volts. Nearly 1500 measurements per spectral band are recorded during the ten solar scans with a sampling spacing of 16.2 arc sec on average. The rest of this chapter will provide information about HALOE that is pertinent to the analysis of its solar data.

3.1 Spectral Response

HALOE measures solar energy in spectral bands centered at wavelengths of 2.45, 2.80, 3.40, 3.46, 5.26, 6.25, 6.60, and 9.85 μm . At these eight wavelengths, solar relative intensity from the exoatmospheric disk scans is measured using essentially a broadband radiometer approach. The end-to-end spectral response of these bands was measured in each HALOE channel during preflight testing. The spectral response of each channel is shown as a function of wavelength in Figures 3.2 and 3.3. The bandwidths at the 5% response level are given in Table 3.1. Detailed descriptions of some of the HALOE filter shapes and/or bandwidths are given in the atmospheric-constituent validation papers [27–32]. It should be noted that center wavelengths and bandwidths shift slightly with instrument temperature; however, the instrument temperature remains fairly constant during solar data collection so these shifts are negligible during an event.

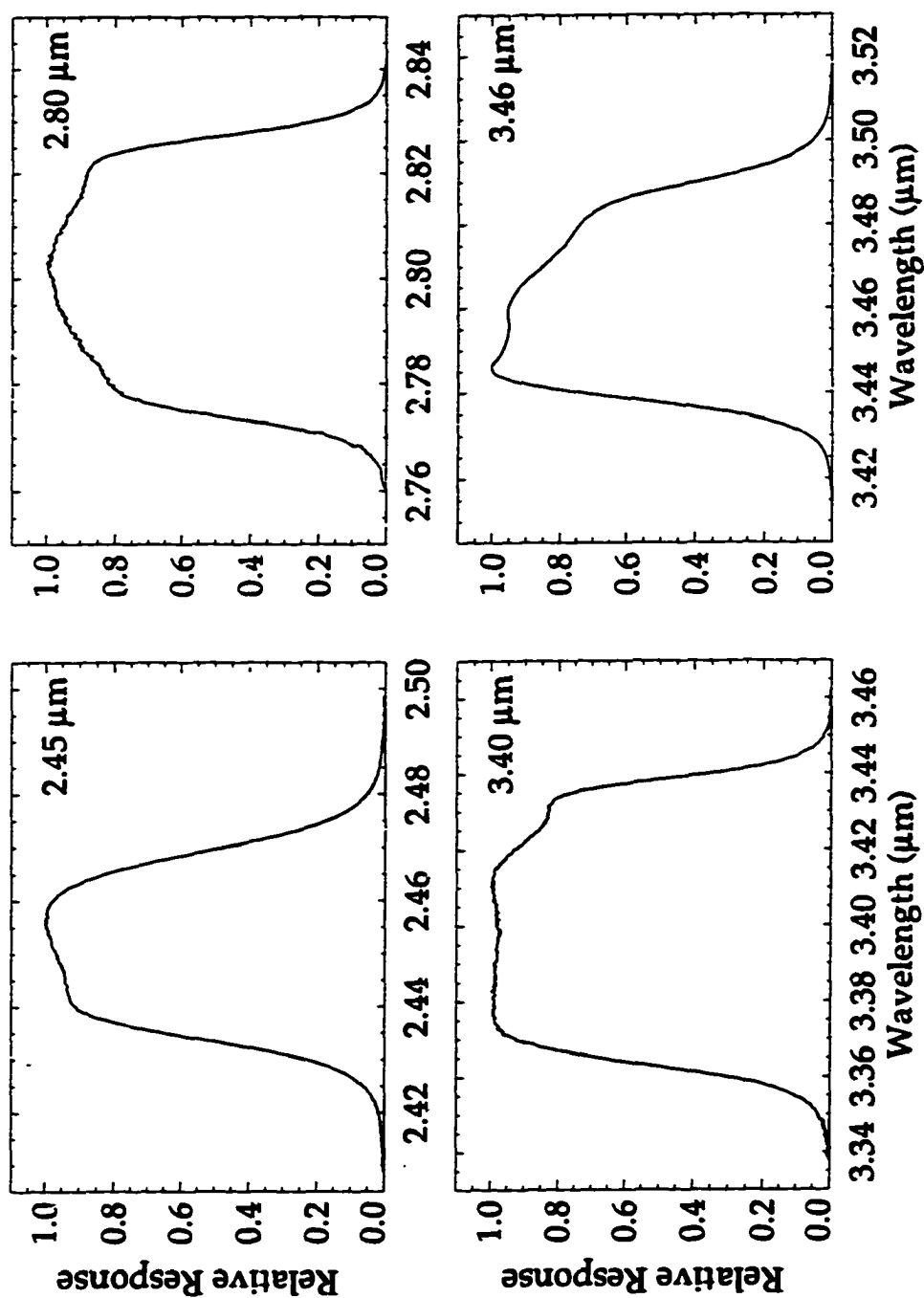


Figure 3.2: The spectral response of the HALOE instrument over the channels centered at wavelengths of 2.45, 2.80, 3.40, and 3.46 μm .

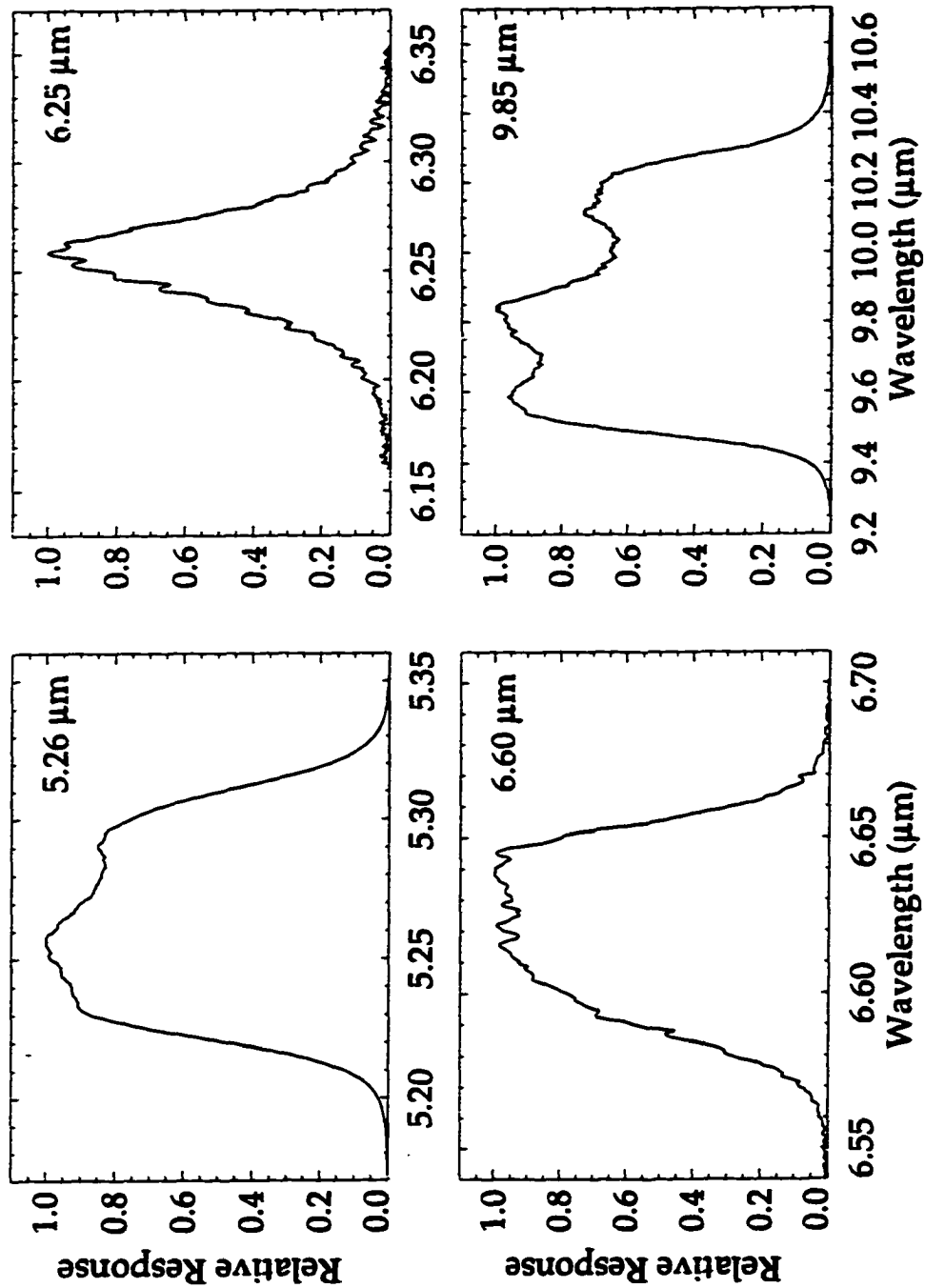


Figure 3.3: The spectral response of the HALOE instrument over the channels centered at wavelengths of 5.26, 6.25, 6.60, and 9.85 μm .

Wavelength (μm)	Bandwidth (μm)
2.45	0.06
2.80	0.07
3.40	0.09
3.46	0.07
5.26	0.12
6.25	0.12
6.60	0.11
9.85	1.01

Table 3.1: HALOE Wavelengths and Bandwidths at 5% Level.

3.2 Spatial Response

Preflight tests determined the spatial response of each HALOE channel over the IFOV. Tests included the scanning of a knife edge and a narrow slit between the detectors and a solar simulator source. From this information, a normalized IFOV function in elevation, $F(\theta_i)$, is determined for each channel. This function is defined for 61 points located between $-2 \leq \theta \leq 2$ (θ in arc minutes) measured from the center of the IFOV. Each of the eight IFOV functions show a 50% response at ± 1 arc min, which correspond to the top and bottom of the slit defining the IFOV. The normalized IFOV functions for the eight HALOE channels are plotted as a function of arc minutes in elevation (relative to the center of the IFOV) in Figures 3.4 and 3.5.

3.3 Sun Sensor

The position of the IFOV on the solar disk is guided by Sun sensors that provide information to stepper motors which drive elevation and azimuth gimbals. There are two analog coarse Sun sensors (CSS); one tracks the elevation of the IFOV, the other tracks

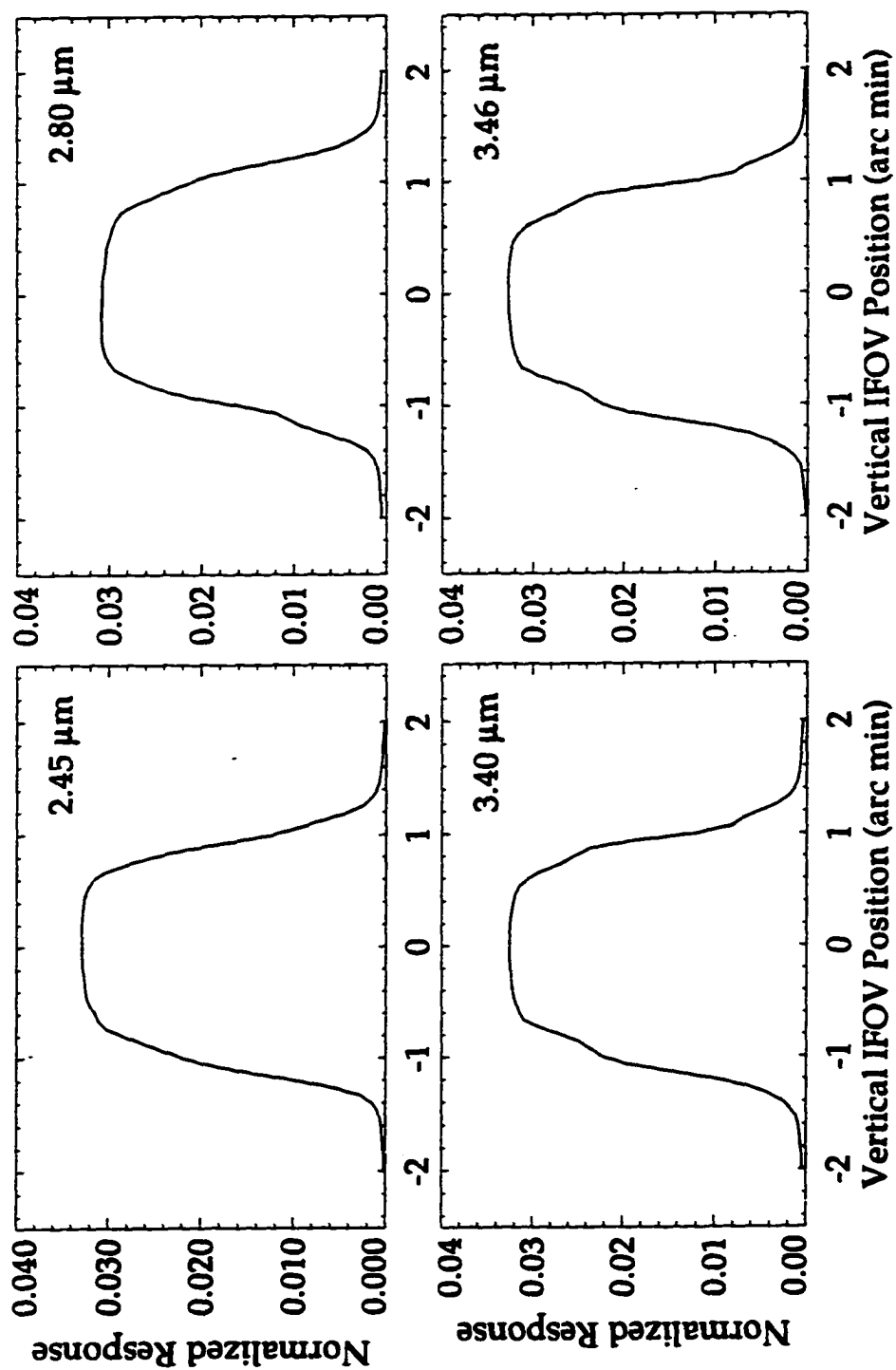


Figure 3.4: HALOE spatial response functions plotted in elevation to ± 2 arc min from the center of the IFOV at 2.45, 2.80, 3.40, and 3.46 μm .

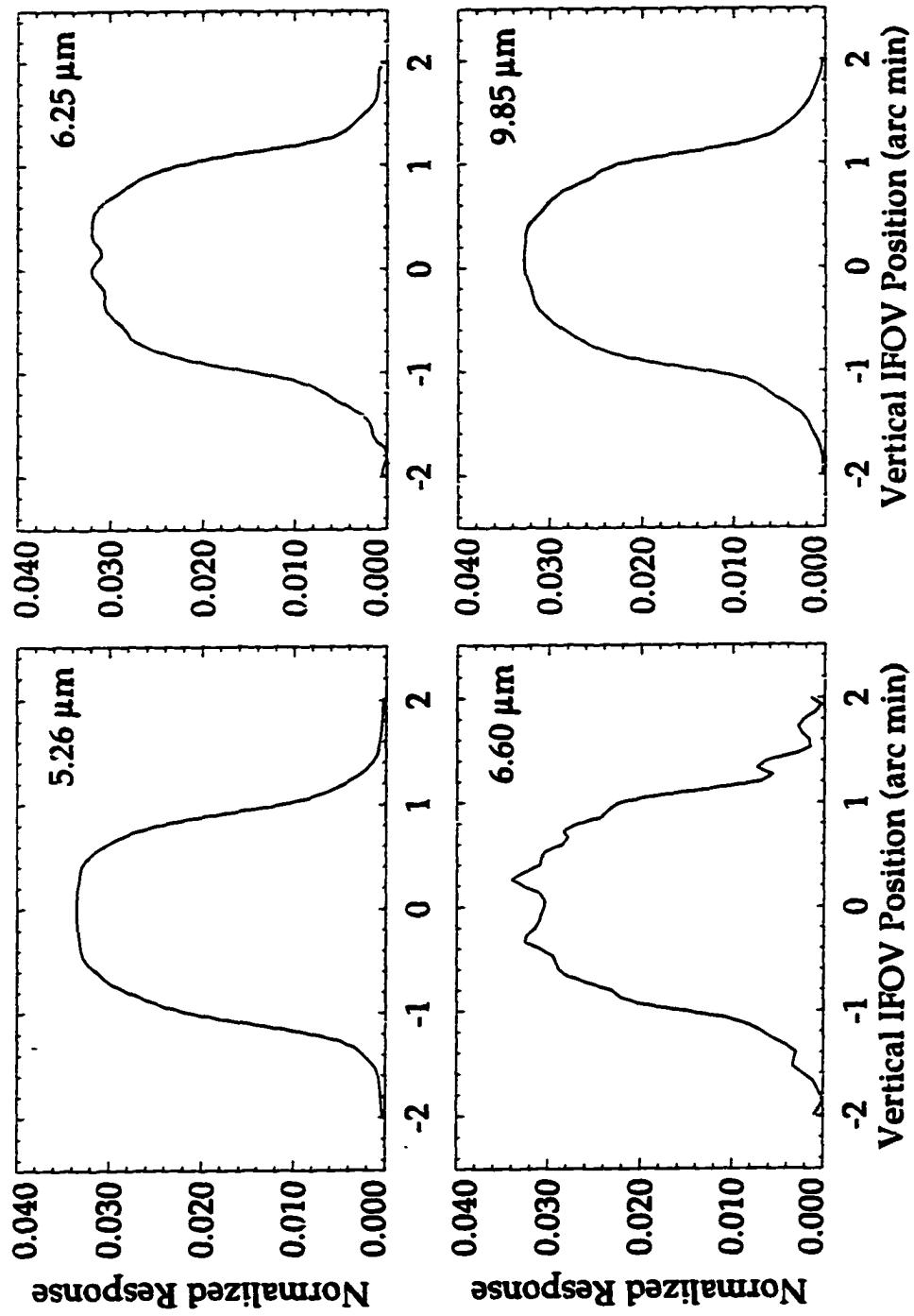


Figure 3.5: HALOE spatial response functions plotted in elevation to ± 2 arc min from the center of the IFOV at 5.26, 6.25, 6.60, and 9.85 μm .

the azimuth. The azimuth CSS (CSSAZ) is used to both acquire and track the radiometric Sun center diameter. CSSAZ is sampled at 8 Hz and recorded throughout the event. The elevation CSS (CSSEL) is used to acquire the Sun at the beginning of an event and as a precursor to track control by the fine Sun sensor (FSS). The FSS provides more sensitive elevation information on the IFOV. It tracks the top and bottom limb of the Sun using a 256-element diode array that has a spacing between diodes of 16.2 arc sec. Diodes are numbered sequentially and register as 'on' or 'off' depending on whether they are pointed on or off the solar disk. The diode number that is 'on' just inside the top limb is recorded as FSSTOP and the last 'on' diode at the bottom is recorded as FSSBOT. The telemetered sampling rate for FSSTOP is 64 Hz while that of FSSBOT is 8 Hz.

3.4 Electronics Response

The amplitude distortion and phase delay caused by HALOE electronics have been accurately determined. These are introduced into the instrument through a low pass electronics filter that increases signal to noise by reducing the noise component of the HALOE signal above 4 Hz. The instrument's frequency response is given in Fourier space by a four-pole Butterworth filter, $\beta(\omega)$, which has 3 dB cutoff at 0.91 Hz.

$$\beta(\omega) = \frac{1}{(\omega_m^4 - A\omega_m^2 + 1) - i(B\omega_m^3 - C\omega_m)}. \quad (3.1)$$

In this expression, $\omega_m = 2\pi\omega/D\omega_B$, $\omega_B = 0.91$ Hz, $A=3.67$, $B=2.774$, $C=2.840$, $D=7.3086$, and $i=\sqrt{-1}$.

The Butterworth filter introduces a time delay in the HALOE signal. The inverse Fourier transform of $\beta(\omega)$ gives the impulse response of the instrument and exhibits a time delay of one-half second. Prelaunch tests have determined that this accurately describes the instrument's response time within 2% or better. From this information, a normalized im-

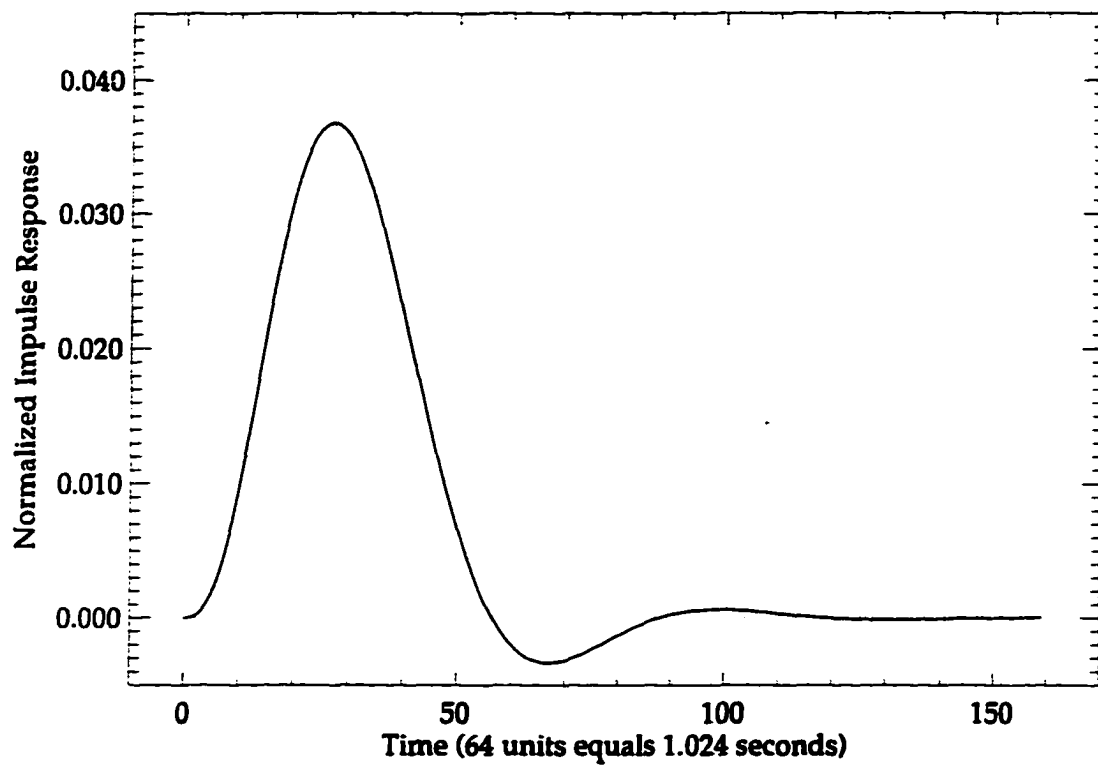


Figure 3.6: The Butterworth function, $B(t_k)$, illustrating the time delay effects in the HALOE signal.

pulse function (henceforth Butterworth function), $B(t_k)$, is determined for the instrument.

This function is defined for 160 points on a 64 Hz scale and is plotted in Figure 3.6.

Chapter 4

Analysis Technique

HALOE solar data have been analyzed to find intensity information about the quiet photosphere and sunspots. In both situations, a nonlinear least squares technique proves to be a powerful tool in obtaining science data values as well as instrument function parameters. A significant portion of the work was spent developing an algorithm that models the HALOE instrument during solar data acquisition. By producing an accurate description of the instrument, a good representation of the data was obtained for nonlinear least squares evaluation. In this chapter, the nonlinear least squares theory will be reviewed and descriptions of the data analysis procedure for obtaining limb darkening information and sunspot intensity will be given.

4.1 Nonlinear Least Squares

A nonlinear least squares technique was adopted to obtain relative intensity information from HALOE solar data. Nonlinear least squares theory has been discussed by several authors, and algorithms employing the method have been developed for a variety of scientific applications [33–37]. The basic premise of this method is to represent some

measurements or data using a set of nonlinear equations that are expressed as functions of unknown parameters. The parameter solutions are obtained when the nonlinear equations describe the data within acceptable limits. In cases where data is represented by a set of nonlinear equations, a solution can be obtained by first order Taylor approximations about a trial value for the parameters [33,34]. Consider n measurements that individually can be represented by the function M_i , where $i = 1, 2, \dots, n$. These data can be approximated with the function $m_i(\alpha, \beta, \dots)$, where α, β, \dots are the parameters to be determined. At each data point, the residual, $R_i(\alpha, \beta, \dots)$, is the difference between the measurement and the approximating function.

$$R_i(\alpha, \beta, \dots) = M_i - m_i(\alpha, \beta, \dots). \quad (4.1)$$

The best values of the parameters, α, β, \dots , are obtained by minimizing the weighted sum of the squares of the residuals, $S(\alpha, \beta, \dots)$.

$$S(\alpha, \beta, \dots) = \sum_1^n w_i [R_i(\alpha, \beta, \dots)]^2. \quad (4.2)$$

The quantity w_i is the weight of the residual and has been introduced here to account for the precision of the measurement .

Solving a system of nonlinear equations can be a formidable task; however, the complexity of the problem can be reduced by considering a Taylor expansion of the approximating function about an initial trial solution, $p_0 = (\alpha_0, \beta_0, \dots)$ [33, 34, 37].

$$M_i = m_i(p_0) + \frac{\partial m_i}{\partial \alpha} \Delta \alpha + \frac{\partial m_i}{\partial \beta} \Delta \beta + \dots \quad (4.3)$$

The quantities $\Delta \alpha$ and $\Delta \beta$ have been used to represent $\alpha - \alpha_0$ and $\beta - \beta_0$ respectively. Rearranging this expression gives a more useful form.

$$M_i - m_i(p_0) = \frac{\partial m_i}{\partial \alpha} \Delta \alpha + \frac{\partial m_i}{\partial \beta} \Delta \beta + \dots \quad (4.4)$$

Since $M_i - m_i(p_c)$ is simply the residual, Equation 4.4 provides a way of producing a set of expressions that are linear in terms of the unknown parameters. Upon calculation of the coefficients to the linear terms, which are specified by the partial derivatives, the parameters can be obtained through the usual least squares procedure. The final solution is obtained through an iterative process in which the parameters are varied and the sum of the squares of the residuals converges to a local minimum.

HALOE solar data have been analyzed using a modified Levenberg-Marquardt algorithm which minimizes the sum of the squares of the residuals between the experimental solar measurements and the relative intensity calculated using fitted parameters [34,37]. Each fitted parameter is initialized and subsequently updated after the approximating functions are determined from the HALOE instrument model. During an iteration, the derivative of each measurement point with respect to each parameter is calculated, and together these derivatives form the Jacobian, J . The final solution is obtained after the sum of the squares of the residuals is minimized within predetermined limits. It is instructive to calculate the standard deviation of the fit, σ_s , for the final solution of n measurements and q parameters.

$$\sigma_s = \sqrt{\frac{S(\alpha, \beta, \dots)}{(n - q)}}. \quad (4.5)$$

This quantity measures the scatter between the data and calculated values and gives a general indication of the precision of the solution.

An inherent difficulty in nonlinear problems is obtaining the appropriate parameter solution from the multiple possible minima. This is particularly troublesome when the approximating function depends upon many parameters. Therefore, it is desirable to obtain the best possible estimates to the initial parameter values. This helps ensure that successive parameter values better approximate the root at the correct local minimum and, as a by-product, the computation time is reduced. In many cases good initial parameter values can

be obtained from a preliminary inspection of the measured data as well as from the past experience of the investigator.

The majority of computational time in the nonlinear least squares analysis is usually spent calculating the derivatives that make up the Jacobian. Typically, these derivatives are found using the method of finite differences where the derivative at a particular data point i with respect to parameter α is found after changing the parameter value by a sufficiently small value, ϵ .

$$\frac{\partial m_i(\alpha, \beta, \dots)}{\partial \alpha} \cong \frac{m_i(\alpha + \epsilon, \beta, \dots) - m_i(\alpha, \beta, \dots)}{\epsilon} \quad (4.6)$$

This method is time consuming since the approximating functions must be recalculated with a small difference in the parameter. Although this technique is slow, it is generally reliable. In some applications, however, the size of ϵ produces a small enough change in the function that roundoff in the finite difference becomes a problem. To avoid these situations, an alternative method for calculating derivatives can be used in some cases. In Section 4.3.3 and in the Appendix, this is explained in more detail.

The nonlinear least squares technique also provides information on the reliability of the solved parameters. From the values of the derivatives which form the Jacobian, J , the parameter uncertainties as well as the correlations between parameters can be found following the discussion of Whittaker and Robinson [33]. These calculations use the elements of the covariance matrix defined as $(J^T J)^{-1}$. The uncertainty in parameter j , σ_j , can be found from the diagonal element of the covariance matrix, x_{jj} .

$$\sigma_j = \sqrt{x_{jj}} \sigma_s \quad (4.7)$$

It should be noted that this uncertainty does not account for all errors in the measurements, but serves only as an indication of the uncertainty due to the scatter of the data combined with the deviation of the mathematical model from the measurements. The off-diagonal

elements of the covariance matrix can be used to find the correlation between pairs of parameters. The correlation between parameters j and k , ρ_{jk} , is found from the off diagonal element of the covariance matrix, x_{jk} .

$$\rho_{jk} = x_{jk} \frac{\sigma_s^2}{\sigma_j \sigma_k}. \quad (4.8)$$

Before any parameters can be evaluated by the method reviewed here, a means of accurately calculating the approximating functions must be determined. HALOE solar data can be analyzed with this technique by modeling the instrument's behavior during data acquisition. A description of forward models used to obtain solar relative intensity information is presented in the remaining portions of this chapter.

4.2 Limb Darkening Analysis

A computer program was written that accurately modeled the HALOE instrument and produced a representation of its measured center-to-limb relative intensities. A non-linear least squares routine found the best values to fitted parameters through a process that consisted of two iterations, each containing two steps. Each step involved the forward calculation of the HALOE signal using the limb-darkening function (Equation 2.23) and the HALOE system response function, which included the spatial IFOV function and the Butterworth filter function. Different parameters were evaluated in each step, and their updated values were used in subsequent steps. In the following discussion, the details of the process are given for the analysis of one event at one HALOE wavelength. An example of the raw relative intensity signal for the ten scans of one event is shown in Figure 4.1.

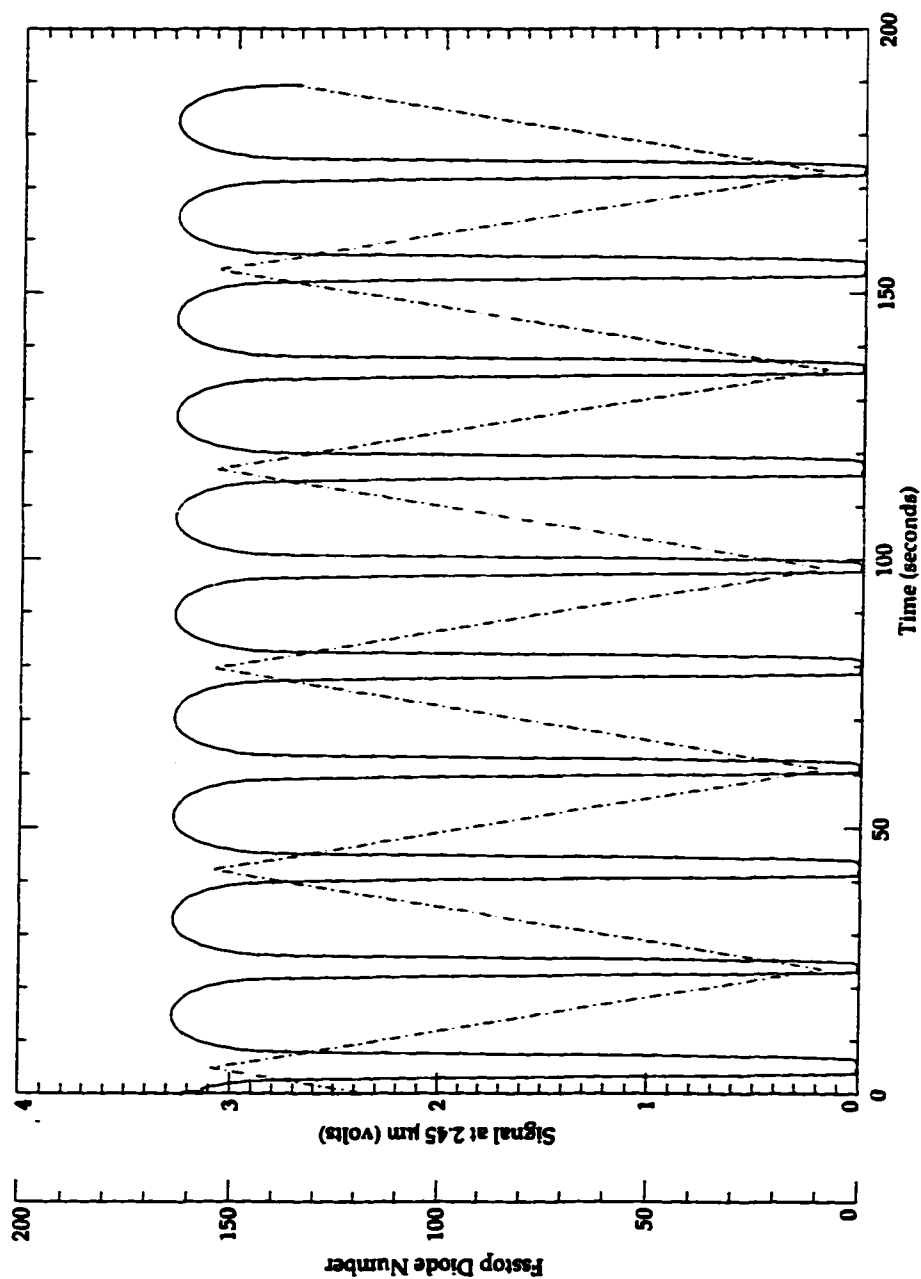


Figure 4.1: Example of $2.45 \mu\text{m}$ raw solar scan data for one event. The relative intensity signal (solid line) in volts shows smooth variation over the disk and sharp discontinuities as the IFOV scans over the limb. The dotted line represents the FSSTOP diode values which increase as the IFOV scans toward the top limb and decrease as the IFOV moves towards the bottom limb.

4.2.1 The Instrument Model

An accurate forward model of the HALOE instrument depends greatly on the ability to properly describe pointing information. This information is obtained relative to the solar disk whose extent can be obtained from ephemeris data. The extent, E , is approximately 32 arc min but varies slightly over the course of the year due to the eccentricity of the Earth's orbit. HALOE scans its IFOV vertically across the solar disk along a chord which has a small azimuth offset, Φ_{az} , measured in arc minutes from disk center. The scan chord on the solar disk is illustrated in Figure 4.2. Also shown in Figure 4.2 are the designations for the two scan orientations. Each of the 10 scans of an event can be characterized as positive or negative depending on whether the IFOV is moving towards the respective top or bottom of the disk as seen by the instrument.

A Cartesian coordinate system is centered on the apparent solar disk and is oriented such that the vertical axis is perpendicular to the local horizon and parallel to the instrument's scan direction. The dimensions of the coordinate axes are linearly specified in units of arc minutes, since the projection of angles less than the extent of the Sun to a sufficient approximation behave in a linear fashion. In this coordinate system, the top and right limb as viewed by the instrument occur at $+\frac{E}{2}$ and the bottom and left limb at $-\frac{E}{2}$. The scale determined in this manner is replicated on the scan chord. As shown in Figure 4.2, angles are designated along the scan chord with the zero angle located where a perpendicular from disk center intersects the chord. Relative to the instrument, positive scan angles start at the center of the chord and move sequentially to the top limb and beyond. Negative scan angles are specified over the bottom half of the scan chord. Since the scan path is usually displaced from the vertical diameter, the limbs occur at scan chord angles less than $\pm\frac{E}{2}$.

Over the scan chord, scan angles, θ_i , are designated that locate the center of the IFOV. In all, 243 scan angles are measured over the scan chord and range from 0 to approx-

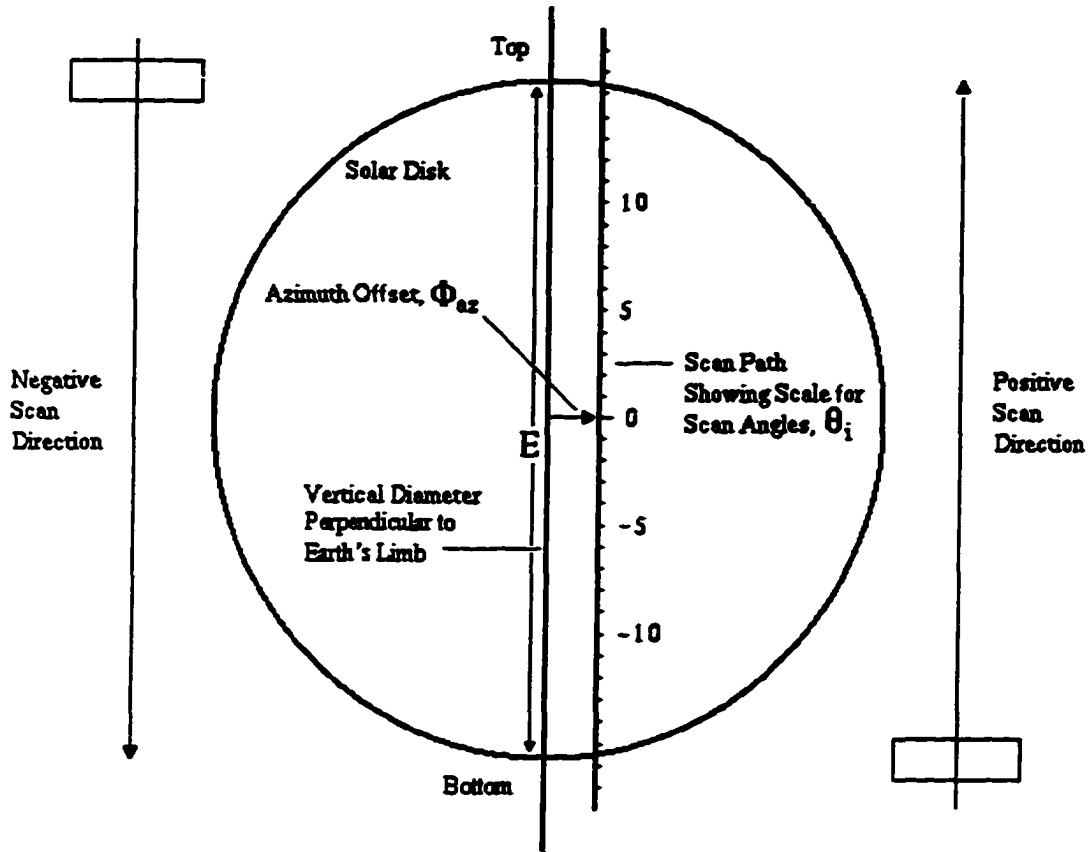


Figure 4.2: Geometry of the scan chord on the solar disk.

imately ± 20 arc min. At each θ_i , the instrument's spatial response effects are incorporated using the IFOV function explained in Section 3.2. At scan angle θ_i , the relative intensity, I_{IFOV} , is calculated at $\theta_i + \theta_j$, where j runs from 1 to 61 and θ_j is the measured IFOV function positions specified from -2 to +2 arc min. The I_{IFOV} values defined in this manner are convolved with the IFOV function to model the spatial effects of the instrument at θ_j and produce a corrected value of the relative intensity, $I_s(\theta_i)$, at that scan angle.

$$I_s(\theta_i) = \sum_{j=1}^{61} F(\theta_j) I_{IFOV}(\theta_i + \theta_j). \quad (4.9)$$

As given in Section 3.2, the vertically defined $F(\theta_j)$ values are obtained by averaging the horizontal responses over the 6.12 arc min width of the IFOV. The $F(\theta_j)$ are shown for each HALOE wavelength in Figure 3.4 and 3.5. Even though no specific horizontal IFOV information exists, horizontal relative intensity information is available due to the finite width of the IFOV and the position dependence of the solar intensity. The $I(\theta_i + \theta_j)$ values that are convolved with the IFOV function are obtained by numerically integrating the relative intensity over the width of the IFOV. This thorough treatment of the available information is accomplished using Gaussian quadrature (see Chandrasekhar chapter 2 [21]).

$$I_{IFOV}(\theta_i + \theta_j) = \sum_{k=1}^g G_w(\phi_k) I_{\lambda}^*(0, \mu(\theta_i + \theta_j, \phi_k)). \quad (4.10)$$

In this expression, the number of quadrature points g is 11, and $G_w(\phi_k)$ are the Gaussian weights at the points of integration within the IFOV. The quadrature points, ϕ_k , are specified in terms of angles over the width of the IFOV. Viewed on the disk from the instrument, these angles fall within the left edge at -3.06 arc min and the right edge at +3.06 arc min of the IFOV. These points are indicated for the position $I(\theta_i + \theta_j)$ in Figure 4.3.

The relative intensity at the quadrature point, $I_{\lambda}^*(0, \mu(\theta_i + \theta_j, \phi_k))$, can be found from the limb darkening function given by Equation 2.23 after solving for $\mu = \cos \theta$. The angle θ is measured from disk center and can be calculated from the coordinates of the IFOV and quadrature point.

$$\theta = \sqrt{(\Phi_{ax} + \phi_k)^2 + (\theta_i + \theta_j)^2}. \quad (4.11)$$

The geometry which leads to this expression is illustrated in Figure 4.4. At any quadrature point on the disk, the relative intensity can be calculated from Equation 2.23. At points outside the limb, the relative intensity is modeled as zero since the decrease in surface brightness is larger than the instrument's signal to noise.

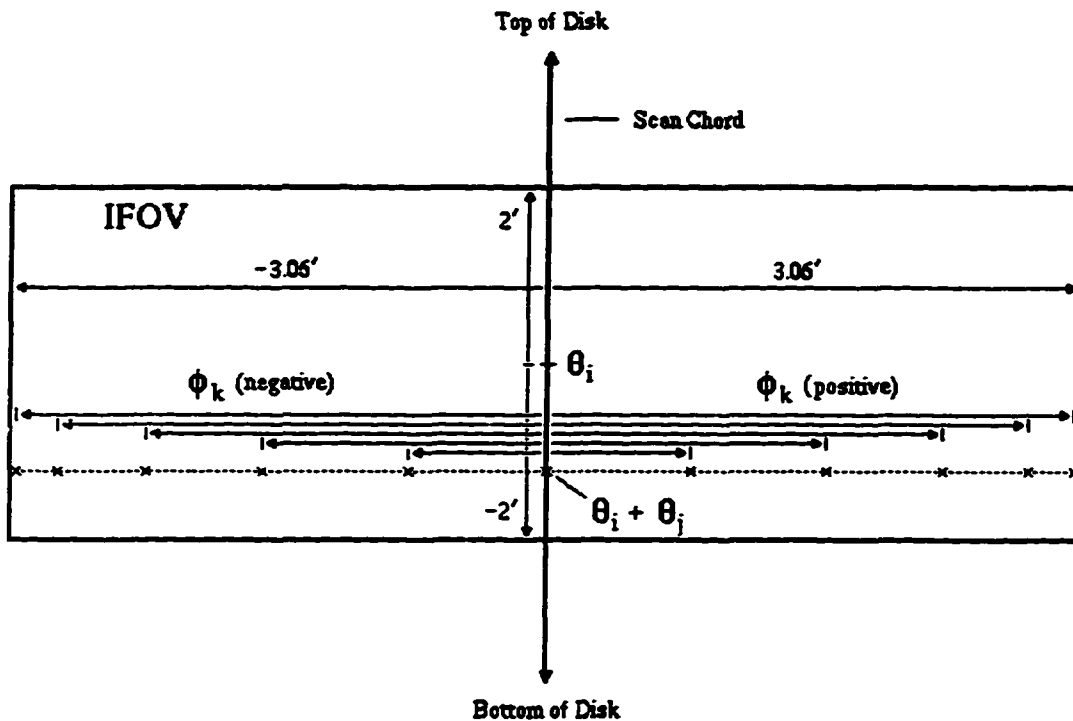


Figure 4.3: The positions of the Gaussian quadrature points in the IFOV for the horizontal integration of the relative intensity at $\theta_i + \theta_j$.

The horizontal relative intensity information in the IFOV is especially important at the limb because of the azimuth offset and the curvature of the limb. As illustrated by condition 1 in Figure 4.5, a particular IFOV function angle, $\theta_i + \theta_j$, specified on the disk near the limb may have only a partial horizontal contribution to the integrated relative intensity. Condition 2 in Figure 4.5 shows that although a $\theta_i + \theta_j$ angle is off the disk, it too may have a partial horizontal intensity contribution if the angle is near the limb. The horizontal intensity contribution in either of these situations can be found by numerically

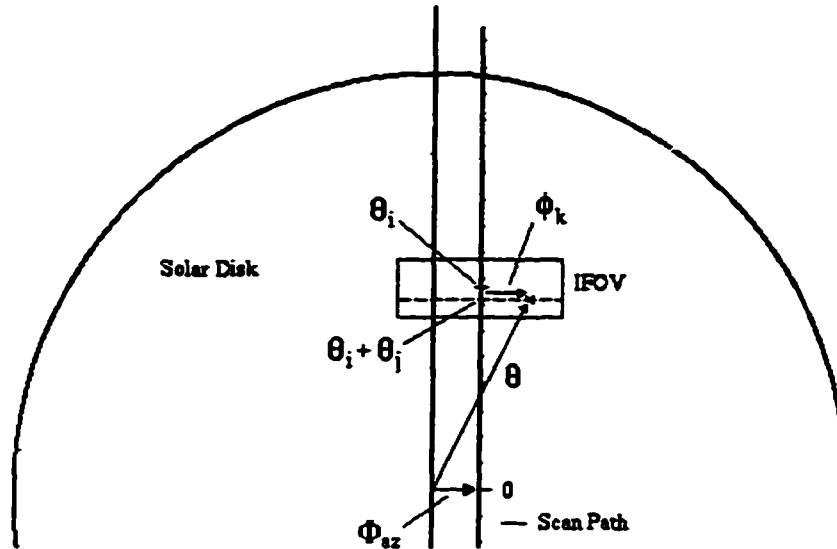


Figure 4.4: Diagram of the geometry used to calculate the angle from disk center, θ . The measured angle θ is the hypotenuse of the right triangle of sides given by $\Phi_{az} + \phi_k$ and $\theta_i + \theta_j$.

integrating the intensity over the horizontal portion l that is on the disk. The relative intensity, $I_{IFOV}(\theta_i + \theta_j)$, at these angles is found by multiplying the integrated value by the ratio of the length of the horizontal portion on the disk, l , to the width of the IFOV, L .

$$I_{IFOV}(\theta_i + \theta_j) = \left(\frac{l}{L}\right) \sum_{k=1}^g G_w(\phi_k) I_{\lambda}^*(0, \mu(\theta_i + \theta_j, \phi_k)). \quad (4.12)$$

The spatially convolved relative intensities, $I_s(\theta_i)$, must be mapped into an 8 Hz time frame that matches that of the recorded HALOE solar measurements. This is done using the FSSTOP data (see Section 3.3), which is recorded on a time scale that coincides with

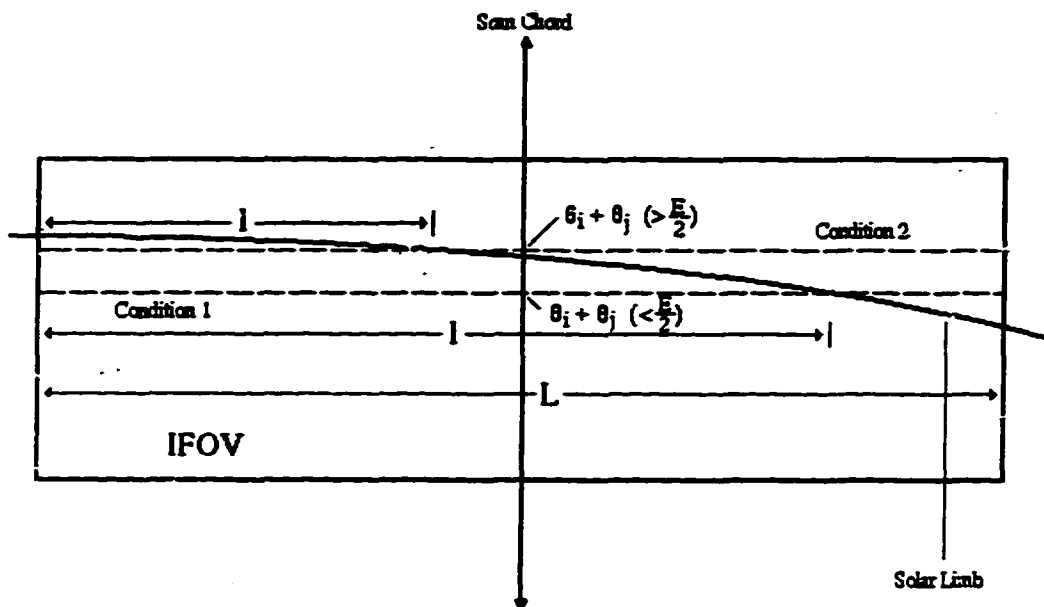


Figure 4.5: An illustration of two conditions where IFOV function angles, $\theta_i + \theta_j$, near the limb have only a partial horizontal intensity contribution to the intensity convolved with the IFOV function. The intensity is found by integrating over the horizontal length that is on the disk, l .

the HALOE relative intensity sampling. The top limb and the bottom limb are determined relative to the diode number scale. Since successive diodes are separated by 16.2 arc sec, each FSSTOP diode can be assigned to a specific scan angle that represents the position of the IFOV. This permits the spatially convolved relative intensity, $I_s(\theta_i)$, to be calculated for each FSSTOP diode number. The actual FSSTOP diode values recorded by HALOE are read and values of the convolved relative intensity can be assigned. $I_s(\theta_i)$ is now on a

time scale that coincides with the actual relative intensity recorded by HALOE.

$$I_s(\theta_i) = I_s(\theta_i(t_k)). \quad (4.13)$$

Here t_k refers to the instrument measurement sample times.

To account for the electronic effects of the instrument, the time-scaled relative intensity, $I_s(\theta_i(t_k))$, is convolved with the Butterworth function, $B(t_k)$, which was described in Section 3.4.

$$I_B(t_i) = \sum_{k=1}^b B(t_k) I_s(\theta_i(t_k)). \quad (4.14)$$

Each value of $I_B(t_i)$ is converted to give the final modeled intensity, $I_f(t_i)$, in volts. This conversion requires determining the maximum signal parameter, I_{max} , and the zero level given as a linear function of time, $I_{zero}(t_i)$.

$$I_f(t_i) = I_{max} I_B(t_i) + I_{zero}(t_i). \quad (4.15)$$

The $I_f(t_i)$ can now be compared to actual HALOE solar measurements. Residuals are measured voltage minus $I_f(t_i)$.

4.2.2 Analysis Description

Preceding the nonlinear least squares analysis, an assessment of instrument data allows the initialization of several instrument model parameters. Raw instrument and science data (designated Level 0') are read in their digital form. Where appropriate, the counts are converted to voltages.

$$volts = 5.000 - \frac{10 \times counts}{4095}. \quad (4.16)$$

Each CSSAZ measurement is converted from voltages, V_{az} , to arc minutes from the vertical diameter of the solar disk, $(\phi_{az})_i$, using a third order polynomial.

$$(\phi_{az})_i = -1.91575 - 13.9966 V_{az} + 3.41057 V_{az}^2 - 0.773352 V_{az}^3. \quad (4.17)$$

The average of the $(\phi_{az})_i$ values over the event, Φ_{az} , is used as the azimuth offset for the event. A positive Φ_{az} indicates that the scan path is to the right of the instrument's vertical diameter on the solar disk while a negative value indicates the scan path is to the left. The recorded FSSTOP data are also examined. Since FSSTOP data was recorded at 64 Hz, a ± 4 point boxcar average is calculated about the FSSTOP data point that coincides with the 8-Hz recorded science data. The fixed value of Φ_{az} and the averaged FSSTOP data determine the necessary pointing information for the scans.

Level 0' relative intensity data are also assessed to produce information about the signal parameters. The digitally recorded relative intensity measurements are converted to voltages and analyzed to find the initial values to the maximum signal and zero level parameters. The fifty highest voltage measurements averaged together produce the initial maximum signal value used in the forward calculation. The initial zero level is the average of the fifty lowest voltages.

Coefficients to the limb-darkening function (Equation 2.23) are obtained from a process that also solves for best values for the limb position in terms of FSSTOP diode number and for signal parameters. An initial attempt at solving for the coefficients and other parameters all at once showed strong nonlinearity and poor convergence. It was deemed necessary to initially solve for certain parameters and then fix them in the subsequent analysis. The following procedure of two iterations consisting of two steps each was developed and adopted to solve for the limb-darkening function coefficients.

In the first step of the first iteration, the FSSTOP diode numbers for the corresponding limb positions are found through the method of nonlinear least squares. A forward calculation is done using the limb-darkening function with interpolated coefficient values from Allen [3]. The best estimates of the limb positions are given in terms of a fractional diode number. Each diode represents 16.2 arc sec and the two limb positions can be used

to find the angular extent of the Sun along the scan chord. This calculated extent is used in the second step.

In the second step of the first iteration, a forward calculation of the limb-darkening function is repeated. This time, the limb-darkening coefficients and the voltage signal parameters are the fitted parameters of the solution. Although the pointing accuracy of the HALOE instrument is more than sufficient for its intended atmospheric use, it is not sufficiently accurate for solar studies when the sharp discontinuity of the solar limb is within the IFOV. Therefore, points are weighted in this step according to how much of the modeled relative intensity is calculated over the limb. Points that are not influenced by the limb are fully weighted.

The second iteration proceeds in the same manner as the first. However, the values of the center-to-limb coefficients, limb positions, and signal parameters found in the first iteration are now the initial values for this iteration. The best values of the coefficients and other parameters are obtained at the end of the second iteration. At this point, the estimated uncertainties in the coefficients and the correlation between the coefficients are calculated following the explanation in Section 4.1.

This is the procedure followed to obtain limb-darkening coefficients for one particular HALOE wavelength from the data of one event. The computer program has evolved into a flexible form, however, that allows for different solution options. The program can simultaneously solve for the limb-darkening coefficients at all eight HALOE wavelengths using data from multiple events.

4.3 Sunspot Intensity Analysis

The forward model described in Section 4.2.1, serves as the foundation for a method that finds the relative intensity of a sunspot located within the IFOV during the solar scan

period. Evidence of the IFOV passing over a sunspot during a solar scan can be seen as a dip in the relative intensity measurements at the sunspot's position. An example of this situation is shown in Figure 4.6 where the relative intensity in volts is plotted as a function of time over the ten scans of one event for the Level 0' signal at $2.45 \mu\text{m}$. The description that follows describes how a one-component sunspot model is incorporated into a nonlinear least squares technique that solves for the relative intensity of a sunspot.

4.3.1 Position Determination of the Sunspot

An initial survey of the HALOE orbital data for a particular event allows the determination of the position of the sunspot relative to the IFOV during the solar scans. The optimal case is to have the sunspot located on or near the center of the IFOV (on or near the scan path) over the course of an event since this situation will minimize any unaccounted horizontal spatial effects of the IFOV. The position calculation involves converting between two coordinate systems and is not only used for the initial position evaluation but in the data analysis as well.

The reference for position calculations is a coordinate system projected onto the solar disk. The origin is at disk center and the ordinate runs in the direction of solar North and South while the abscissa runs East and West. Angles are linear specified on the axes in units of arc minutes with positive values towards North and East and negative angles towards South and West. It should be noted that disk representations designate solar East to the left and solar West to the right as viewed from Earth.

The orientation of the scan chord in the disk coordinate system is calculated using the recorded orbital information of the instrument and spherical trigonometry. Following the theory given in Smart's Chapter VII [38], the solar axis, the Earth's axis of rotation, and the instrument's vertical diameter are projected onto the observed solar disk. The

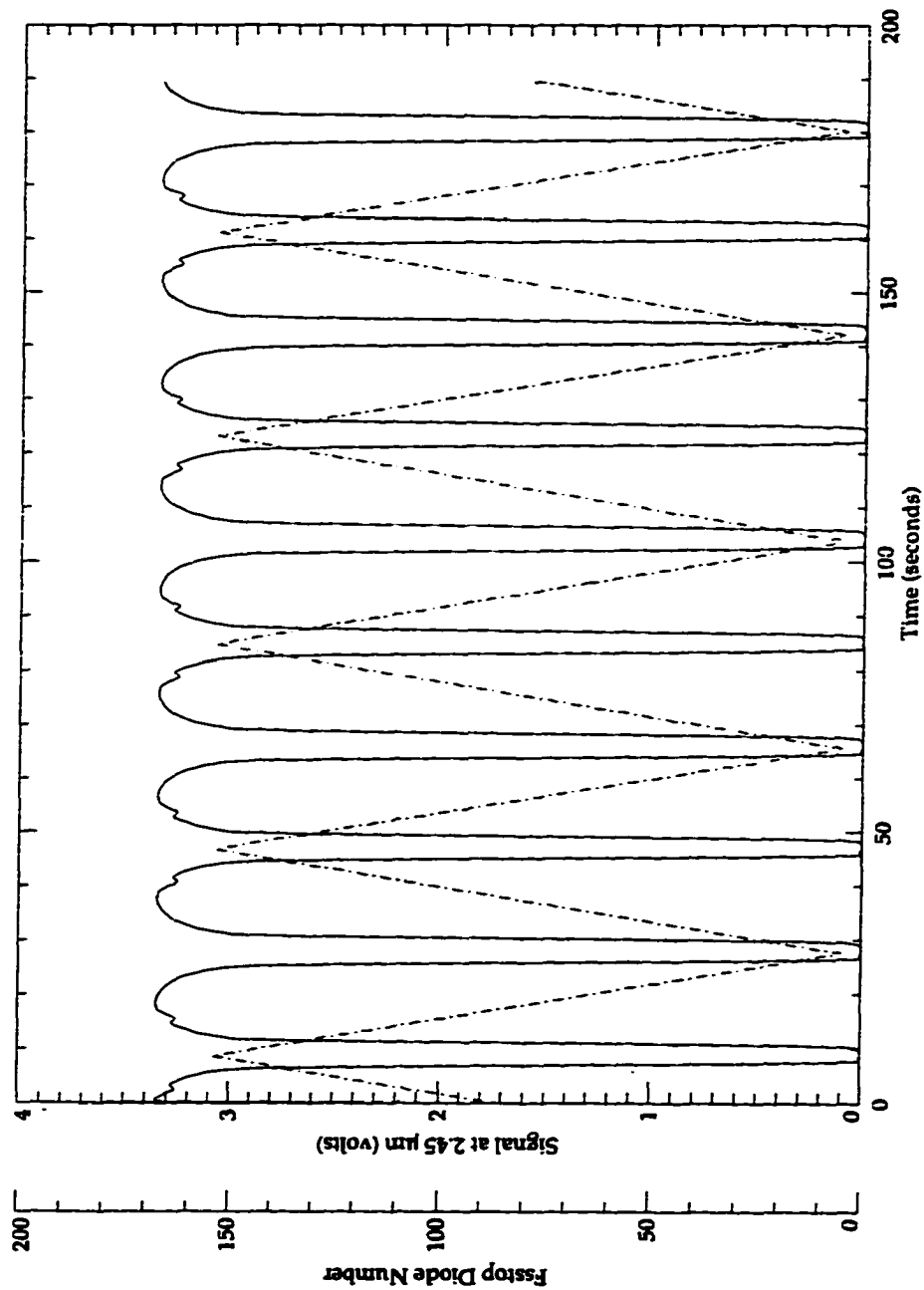


Figure 4.6: An example of raw solar scan data for an event that includes a sunspot. The $2.45 \mu\text{m}$ signal (solid line) in volts shows a small dip when the IFOV scans over a sunspot. The dotted line represents the FSSTOP diode values which increase as the IFOV moves toward the top limb and decrease as the IFOV moves towards the bottom limb.

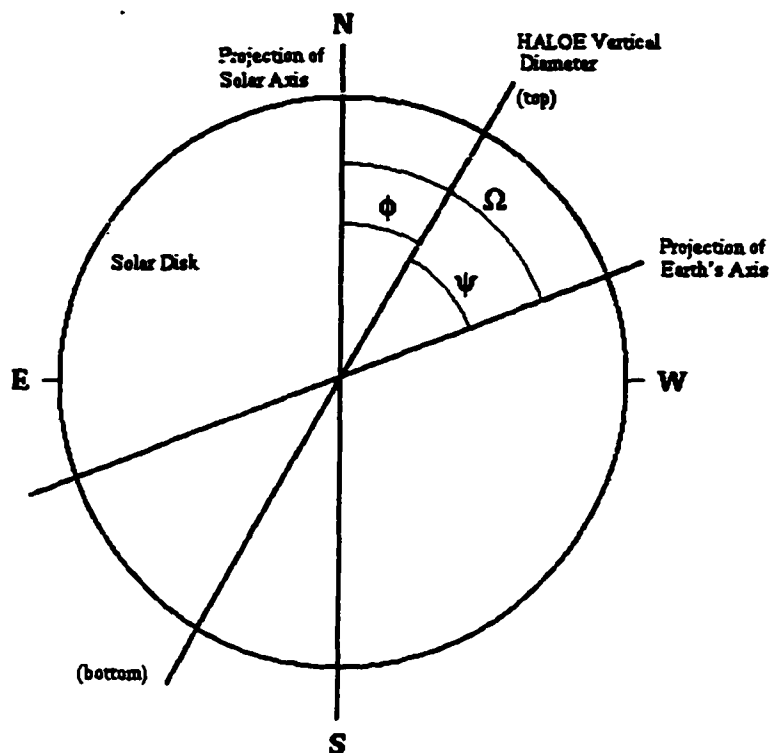


Figure 4.7: The geometry of the projections of the disk coordinate system, the solar axis, the Earth's axis of rotation, and scan chord onto the observed solar disk. The angle ψ is measured between the projection of the Earth's rotation axis and the vertical diameter of the instrument. The calculated angle Ω is measured between the projection of the Earth's axis of rotation and the projection of the solar axis.

orientation of these projected lines is illustrated in Figure 4.7. Together the angles ψ and Ω shown in Figure 4.7 give the orientation of the scan path with the solar axis. Orbital geographic coordinates of the instrument at the time of the solar scanning period are used to compute ψ which is the angle between the projection of the Earth's rotation axis and the the vertical diameter of the instrument on the solar disk. The calculation of this angle follows from Smart page 53 [38]. The angle that the projection of the Earth's axis makes with the projection of the solar axis, Ω , is found from the discussion in Chapter VII of Smart [38]. The orientation of the scan chord relative to the solar axis is given by the angle

ϕ which is found by combining the angles ψ and Ω .

$$\phi = \Omega - \psi. \quad (4.18)$$

With ϕ known, the disk coordinates for any point on the scan chord can be calculated.

The location of the sunspot on the solar disk can be found using published sunspot position data. Numerous observers track sunspots daily and record the heliographic latitude and longitude of sunspots as well as other solar data which are available in monthly publications (see for example [39, 40]). Sunspot positions are given at several times (given as Universal Time, UT) over the course of a day. This information points out that sunspot coordinates change with time due to the solar rotation. Over the approximately three minute HALOE solar data collect period, however, sunspot coordinates typically vary less than 0.04 degrees in heliographic longitude and remain virtually constant (within 0.0003 degrees) in latitude.

From the published coordinates on a particular day, a linear relationship can be derived that determines the heliographic longitude and latitude as functions of UT. Since the time (in UT) of a HALOE solar scan is recorded in the LEVEL 0' data, the heliographic latitude and longitude of a sunspot at the time of a solar scan can be calculated from the linear relationships developed from the observed data. The sunspot's heliographic position can now be mapped onto the disk and an ordered pair of disk coordinates can be determined for the sunspot.

The sunspot's location relative to the scan path determines whether the IFOV will scan over it. Since disk coordinates for any point on the scan path can be specified, an equation for a line that represents the path can be determined. The disk coordinates for the point, P , where a line passing through the sunspot perpendicularly intersects the line representing the scan path can be calculated algebraically. Conversion of the disk coordinates of P to a scan angle gives the angle measured along the scan path, θ_{spot} . The

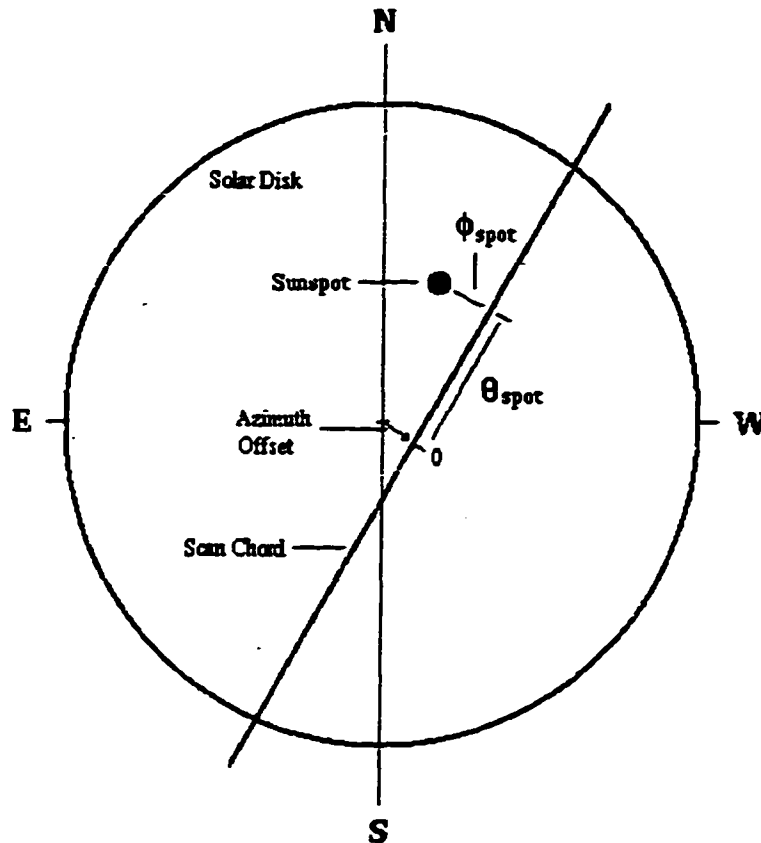


Figure 4.8: Coordinates of a sunspot measured in arc minutes along the scan path, θ_{spot} , and perpendicular to the scan path, ϕ_{spot} .

distance between this point and the sunspot point, ϕ_{spot} , represents the amount the sunspot is displaced perpendicularly from the scan path. These coordinates are illustrated in Figure 4.8. From the perspective of the instrument, the angularly measured ϕ_{spot} is given a positive value if the sunspot center is to the right of the scan path and a negative value if the sunspot is to the left. Data for which the sunspot center is located on or near the scan chord are desirable.

4.3.2 Analysis Technique

The sunspot relative intensity analysis of HALOE solar data includes several steps involving the forward instrument model described in Section 4.2.1. Prior to the actual analysis procedure, instrument data are assessed in a manner described in Section 4.2.2. Where appropriate, Level 0' data are converted to voltages. CSSAZ data are used to find Φ_{az} , FSSTOP data are smoothed, and the relative intensity measurements are examined to determine the preliminary values of the maximum signal parameter and the zero level.

In the initial step, analyses of the HALOE relative intensity data produce information on the limb position in terms of FSSTOP diodes. A forward calculation is done using the limb-darkening function with coefficients fixed to values obtained from investigations of the quiet photosphere. At this point, no attempt is made to correct the smoothly behaving limb-darkening function for the lower intensity of the sunspot. The modeled relative intensity at the limbs is not significantly influenced by the intensity of the sunspot, so reliable FSSTOP diode numbers for the limb position can still be obtained through a forward model analysis. The resulting limb position values are fixed throughout the remaining procedure. The signal parameter results, however, are only preliminary since they are heavily influenced by the sunspot intensity.

Next, the residuals from the previous step are analyzed to obtain more specific information on the location of the sunspot. Since the sunspot is less intense than the surrounding photosphere, the residual versus scan angle plot will show dips on either side of the location where the sunspot is in the IFOV. The two dips occur because of the time delayed nature of the measurements taken from opposite scanning directions of the IFOV. To help identify the exact location of the relative intensity minimum, the scans are divided and classified as positive or negative scans. Positive scans have the IFOV scanning towards the top of the solar disk relative to the instrument (in the direction of the designated positive

scan angles). Negative scans have the IFOV scanning in the opposite direction. The average of the residual minimum positions specifies the value of the angle θ_{spot} of the sunspot center.

The horizontally measured position of the sunspot center to the scan path, ϕ_{spot} , can now be calculated using the published sunspot positions. The heliographic latitude of the sunspot can be represented in disk coordinates as a line since the sunspot's latitude remains constant over the time of solar data acquisition. The intersection of this line and one perpendicular to the scan path passing through θ_{spot} is used to calculate the horizontally measured displacement from the scan path to sunspot center, ϕ_{spot} . Relative to the instrument's perspective, the value for ϕ_{spot} is assigned a positive or a negative value if the sunspot center is located to the right or left of the scan path.

Once the location of the sunspot center is found, the angles θ_{spot} and ϕ_{spot} are used to find a range of IFOV positions where the sunspot relative intensity is measured. Since the sunspot is modeled as a circle of radius R and the IFOV vertical dimensions are ± 2 arc min from its center, the sunspot will be at least partially in the IFOV when the distance measured along the scan path between θ_{spot} and the scan angle of the IFOV is less than $(2 + R)$ arc min. This position is determined as the IFOV approaches the sunspot for all positive and negative scans. A sunspot circular model is shown relative to the moving IFOV in Figure 4.9.

As the IFOV scans past the sunspot, however, the time delay of the signal carries sunspot intensity information beyond $(2 + R)$ arc min. The data of each scan can now be separated into two groups. If the sunspot is located within the IFOV of a particular data point, or if the point has effects of the sunspot due to the signal time delay, the point is indicated as a sunspot point. Those data that have no sunspot information are designated as photosphere points. After these data points are identified, a nonlinear least squares

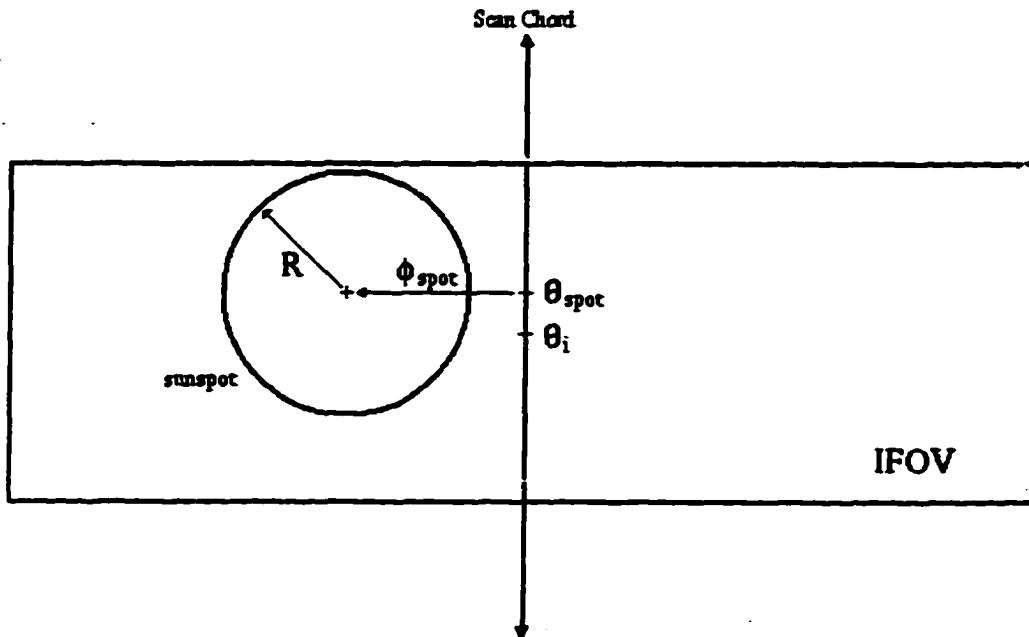


Figure 4.9: A circle of radius R with its center located at θ_{spot} and ϕ_{spot} shown relative to the moving IFOV. A portion of the sunspot will be located within the IFOV at scan angles where the difference between θ_i and θ_{spot} is less than $2 + R$.

analysis of only the photosphere points obtains the best values of the signal parameters.

These parameters are fixed to these values throughout the remainder of the study.

The sunspot information is obtained in the final step. Since sunspots vary in appearance and position, the specifics of the analysis may need to be modified; however, the following general procedure forms the basis. After gathering all preliminary information, sunspot parameters are evaluated by analyzing only the sunspot data points. A one-component model of the sunspot is adopted which assumes that the sunspot appears

as a dark circle of uniform intensity on the solar disk. A nonlinear least squares method is used to obtain specific sunspot parameters: the radius of the spot, the intensity difference between the photosphere and the spot, and the scan angle position of the sunspot. The parameter results are recorded and uncertainties for each are calculated as described in Section 4.1.

4.3.3 Calculation of Sunspot Parameter Derivatives

As explained in Section 4.1, a nonlinear least squares analysis involves calculating the derivative of each data point with respect to each fitted parameter to form the Jacobian. In most cases, the derivatives are calculated by the method of finite differences which involves a recalculation of the relative intensity at each point with a small change in the parameter. This procedure is computationally time consuming especially when a large number of evaluations must be performed. The derivatives with respect to the sunspot parameters can be found directly, thus avoiding the need to recalculate the relative intensities. This approach also increases the accuracy of the derivatives by eliminating the the need for obtaining the horizontal contribution of the relative intensity over the IFOV with Gaussian quadrature integration. The details of the alternative derivative calculation with respect to each of the the sunspot parameters are given in the Appendix.

Chapter 5

Photospheric Relative Intensity and Temperature

This chapter describes information on the quiet photosphere obtained from HALOE solar data and gives a complete accounting of details previously published [41]. At eight infrared wavelengths, center-to-limb relative intensity is evaluated by solving for coefficients to a limb darkening function. These coefficients are used to determine temperature information over a range of photospheric altitudes. The results of this analysis are compared to existing measurements as well as model predictions.

5.1 Instrument and Observing Information

In selecting HALOE solar scan data to analyze, two conditions were considered: solar activity and scan orientation. Days of very low solar activity in early and late May and early June 1994 afforded the best opportunity to view the quiet Sun, and HALOE solar scans were done over a variety of orientations on the solar disk during that time. Over this time, HALOE obtained data while scanning the solar equator during the sunrise events of

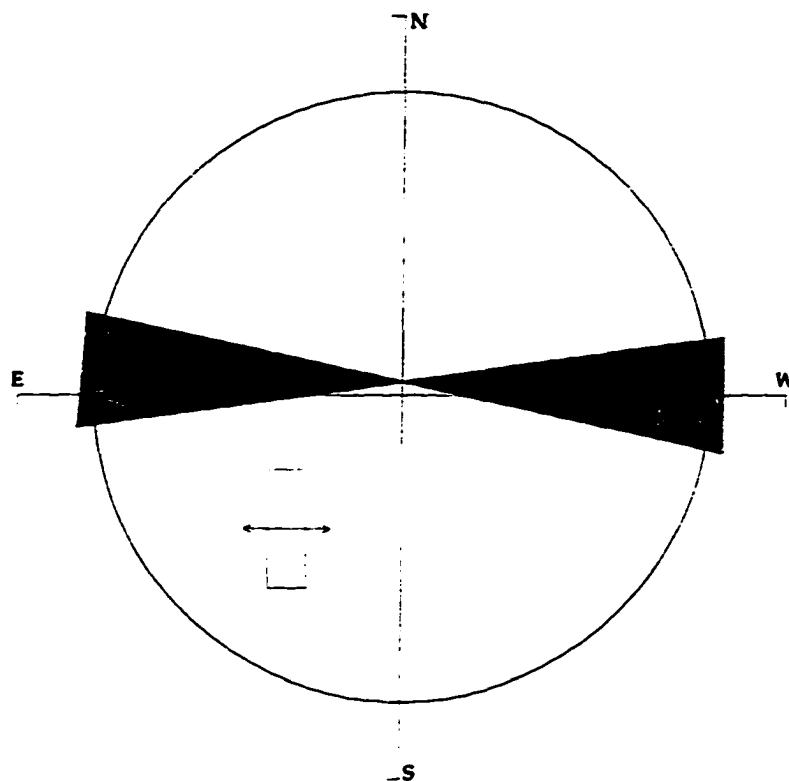


Figure 5.1: HALOE solar scan positions relative to the solar disk. The shaded horizontal region indicates the coverage of the center of the scan chords for the sunrise events that scanned the solar equator. The IFOV is shown to scale on the lower left portion of the disk.

May 4-6, 1994. Activity was very low over these three days with American Relative Sunspot Numbers ranging from 11 to 18 [39].

The position of the scan chord during the selected events are indicated in Figure 5.1. Because the orbital position of HALOE (relative to the Earth's limb and the Sun) is constantly changing, the instrument's scan path across the disk also changes from event to event. The scan path also varies over the course of a single occultation event, but this change is small; the initial and final paths differ by less than one-half the width of the IFOV.

In addition, all scans have a small azimuth offset from the center of the Sun that remains relatively constant over the duration of the event.

Events were chosen that had the center of their scan path at the limb less than one-half the IFOV width from the solar equator. A few events were included that meet this criterion at one limb but do not quite meet it at the opposite limb. During this time 45 occultation sunrise events met the geometric criterion for a total of 65,700 data points. The azimuth offsets of these events ranged from 0.5 to 0.9 arc min, and the average instrument temperature over this data collection period ranged from 25.3° to 26.9° C.

5.2 Relative Intensity Results

This HALOE solar data is analyzed using a nonlinear least squares method in the manner described in Section 4.2. The two limb-darkening function coefficients, a_λ and b_λ , are simultaneously obtained at the eight HALOE wavelengths by fitting data from the 45 selected events over the solar equator. For the fits to the measurements, weighted residual (observed minus calculated) plots are shown in Figure 5.2 for the eight HALOE wavelengths. Position values on the abscissa of these plots are given in terms of the ratio of the observing angle from scan center, ϕ , to the angle from center to limb, ϕ_\odot . The dotted lines represent the digitization level of the instrument for that channel. The standard deviation of the fit ranges from 3.1 to 5.9×10^{-4} of the central intensity, and in all instances the data are fit to the digitization level of the experiment.

The retrieved coefficients, a_λ and b_λ , are given along with their uncertainties in Table 5.1. The correlation between the two coefficients is approximately -0.99, which indicates a very high interdependence between a_λ and b_λ . Thus, the uncertainties in the coefficients are much larger than the uncertainties in the center-to-limb relative intensities. It is also found that the uncertainty in the limb-darkening function, which is calculated from the

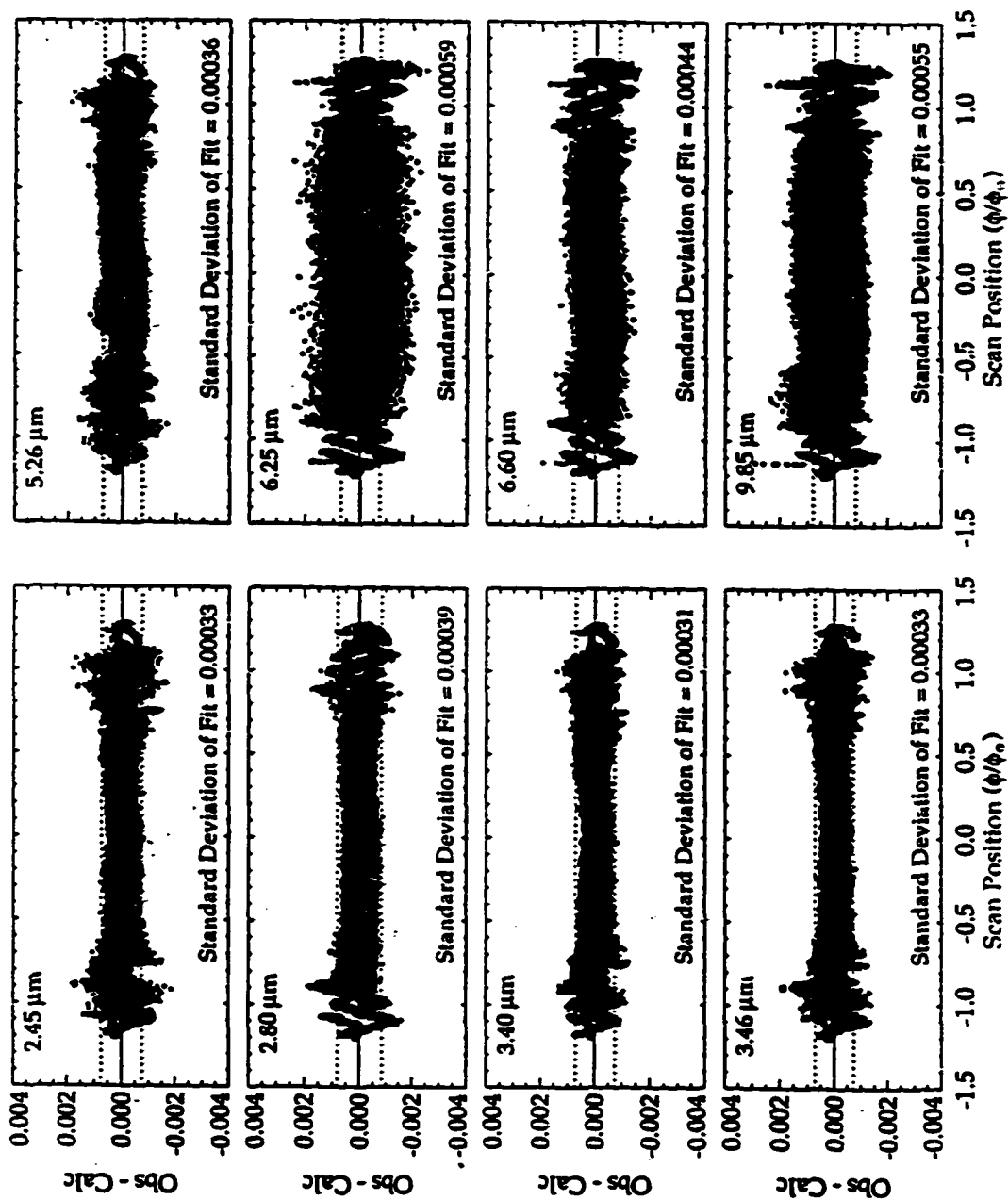


Figure 5.2: Weighted residuals (observed minus calculated) from the analysis of the solar equator data of May 4-6, 1994. In each plot the values on the vertical axis are normalized to unit central intensity. The position on the disk is measured along the scan path and is given in terms of the ratio of the observing angle from scan center, ϕ , to the angle from center to limb, ϕ_{\odot} . All fits match the experimental data to the digitization level (indicated by the dotted horizontal lines in each plot).

uncertainty of the two correlated coefficients, is unrealistically small due to the large number of data points analyzed. In order to obtain a more reasonable value, it is estimated that systematic errors would produce at most a one-half bit uncertainty in the measurement. The residual plots of Figure 5.2 confirm this. The uncertainty of the relative intensity is found by combining the uncertainties due to the coefficients and the estimated uncertainty due to the digitization level of the measurement. From the center of the Sun to 0.25 arc min from the limb (more than 98% of the solar disk), twice the standard deviation (2σ) is less than or equal to 0.1% for each HALOE wavelength.

Wavelength (μm)	a_λ	b_λ	c_λ^\dagger
2.45	1.0749(2)	0.0610(1)	-0.4429(4)
2.80	1.0716(3)	0.0547(1)	-0.4116(5)
3.40	1.0449(2)	0.0568(1)	-0.3314(4)
3.46	1.0459(2)	0.0563(1)	-0.3331(4)
5.26	1.0361(3)	0.0469(1)	-0.2705(5)
6.25	1.0439(5)	0.0359(2)	-0.2601(8)
6.60	1.0455(4)	0.0335(2)	-0.2574(6)
9.85	1.0614(5)	0.0166(2)	-0.2542(8)

[†] Calculated using a_λ and b_λ in Equation 2.24

Table 5.1: Coefficients to the limb-darkening function at HALOE wavelengths.

The limb-darkening functions are calculated from the coefficients given in Table 5.1 and plotted as a function of μ in Figure 5.3(a). The decrease of limb darkening with wavelength is apparent. HALOE results are compared with other published data in Figure 5.3(b). Allen [3] reported coefficients for Equation 2.23 at 2, 3, 5, and 10 μm . Pierce, Slaughter, and Weinberger [7] reported coefficients for a different limb-darkening function at wavelengths in the near infrared up to 2.4 μm . Other measurements over the disk were reported by Pierce *et al.* [12] at 3.5, 8.3, and 10.2 μm and Léna [9, 10] at 5 and 10.4 μm .

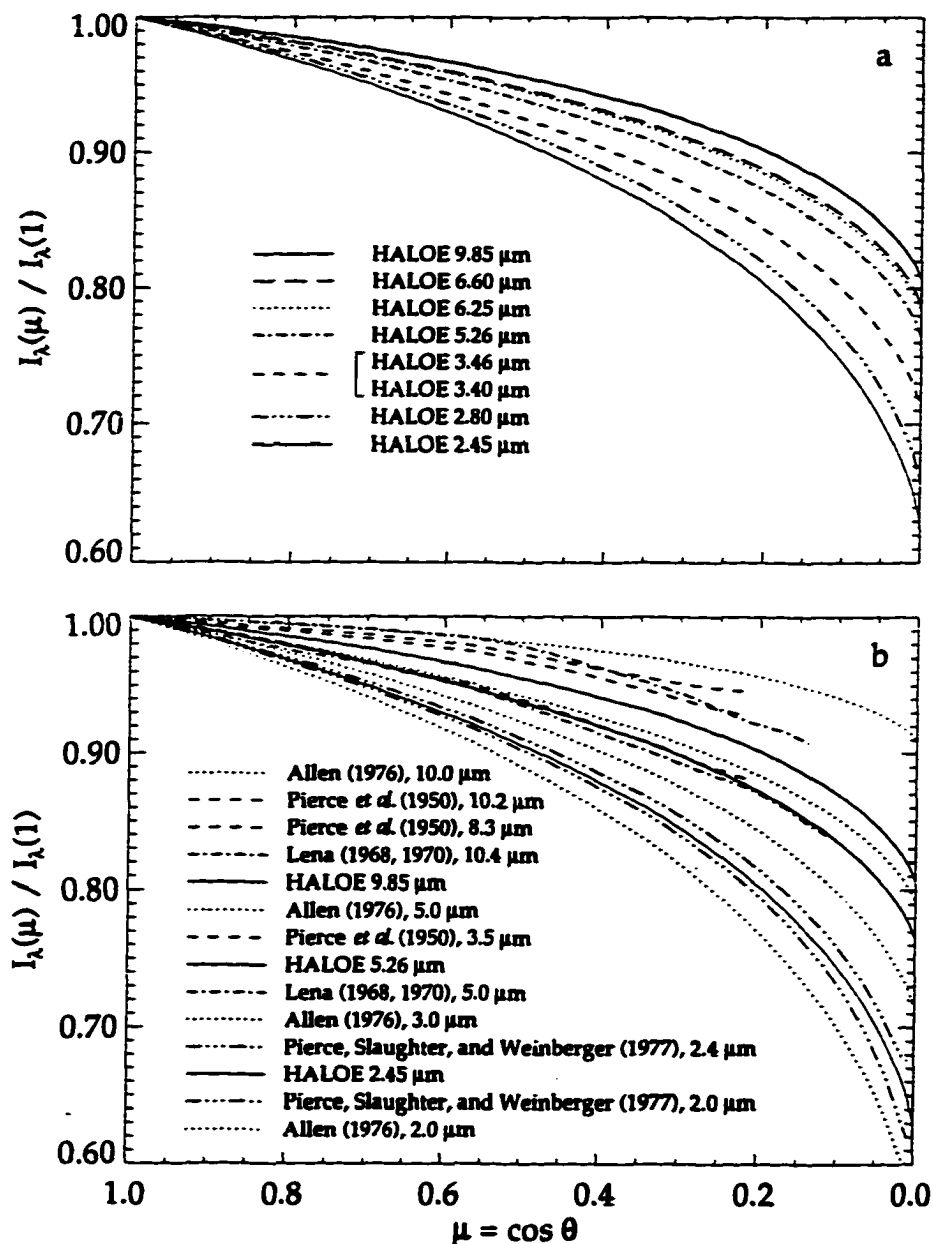


Figure 5.3: (a) The limb-darkening functions as calculated using the coefficients of Table 5.1. The order that the curves are labeled indicates their position in the plot. A single line indicates the limb-darkening functions at 3.40 and 3.46 μm , since they are indistinguishable at this scale. (b) HALOE relative intensity at selected wavelengths along with various other relative intensity data are plotted as a function of μ . In general, the line labels coincide with the order of the curves in the plot.

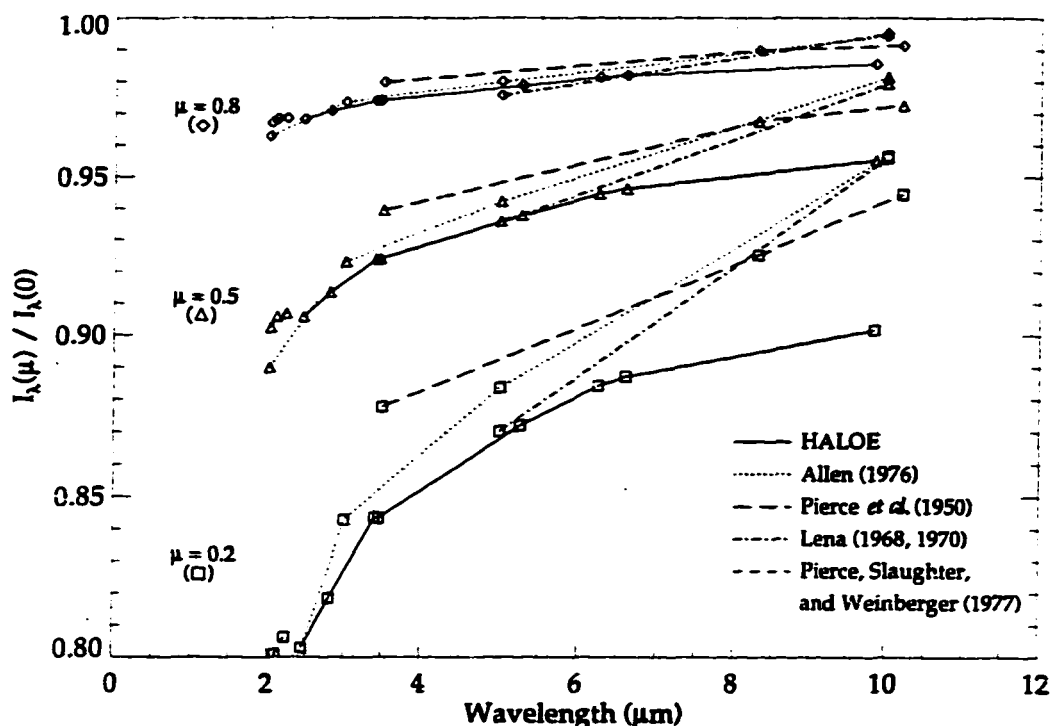


Figure 5.4: Relative intensity as a function of wavelength at three values of μ for both HALOE and other measurements. In general, good agreement exists between HALOE relative intensity and other data between 2 and 5 μm . Between 5 and 10 μm , however, HALOE relative intensities are lower than other values.

Figure 5.3(b) shows that as wavelength increases, the HALOE relative intensity exhibits more limb darkening than that reported by other experiments. Small differences are seen between HALOE values and other measurements at 2.45 μm . Predicted higher relative intensity values from both Allen [3] and Pierce, Slaughter, and Weinberger [7] would differ from HALOE results at 2.45 μm by at most 1.5% of the central intensity. Figure 5.4 shows that these small differences between the data sets are evident up to approximately 5 μm ; however, the Pierce *et al.* [12] values at 3.5 μm are much higher than all others. From 5 to 10 μm , increasing differences between HALOE relative intensities and other data become more apparent. In this wavelength range, HALOE results predict a trend towards

more limb darkening than Allen [3], Léna [9,10], and Pierce *et al.* [12]. In the extreme case around $10\ \mu\text{m}$, Figure 5.4 shows that HALOE limb darkening is nearly twice as great as the other data sets.

As a means of gauging the reliability and consistency of the results, coefficients for the limb-darkening function are also retrieved from HALOE data obtained over two different scanning paths: pole to pole and diagonal (from the 45° latitude northeast limb to the -45° southwest limb as viewed by the instrument). Previous work by Caccin *et al.* [42], Altrock and Canfield [4], and Falciani, Rigutti, and Roberti [43] suggested that there is no significant temperature variation between the solar equator and pole. It is anticipated that relative intensity measurements would also vary little from equator to pole.

Data over vertical and diagonal scan paths were selected from events occurring in late May and early June, 1994. The coverage of the scan paths for these two orientations is shown in Figure 5.5. From May 31 to June 2, 1994, HALOE recorded measurements diagonally across the disk from the 45° NE limb to the -45° SW limb. During this time 42 sunset events (containing 61320 points) occurred that met an analogous geometric criterion to that previously described for the equator scans. Pole-to-pole relative intensities were measured during 44 sunrise events (64240 total data points) from June 3-5, 1994. Activity was very low during both of these time periods; the American Relative Sunspot Number for these days was 0 [39,40]. The average instrument temperature over this six day data collection period ranged from 23.3° to 27.6° C.

Relative intensities from these two sets of measurements are consistent with the results from the equator data to the uncertainty level of the measurements. The differences between the results from the three orientations are shown as a function of μ in Figure 5.6. When relative intensities from the three different scan paths are compared, the differences found are very small. From the center of the Sun to approximately 2 arc min from the limb,

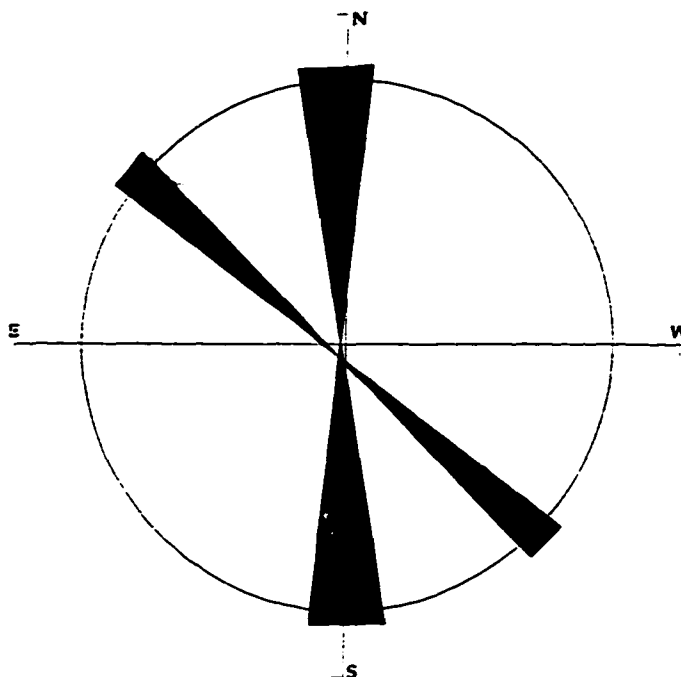


Figure 5.5: HALOE solar scan positions relative to the solar for two other relative intensity studies. The vertical shaded region indicates the coverage of the centers of the scan chords for the sunrise events used to analyze the relative intensity from pole-to-pole. The shaded region from the 45° NE limb to the -45° SW limb as seen by the instrument indicate the coverage of the scan chords for sunset events used to obtain diagonally measured relative intensity.

the values over the equator are greater than those from pole to pole at every wavelength, but the amount is less than 0.06%. This difference is not significant since it is very close to the noise level of the measurements. However, it does demonstrate the consistency of the HALOE relative intensity results. Comparable or smaller differences were found between the values for the diagonal path and those for the other paths.

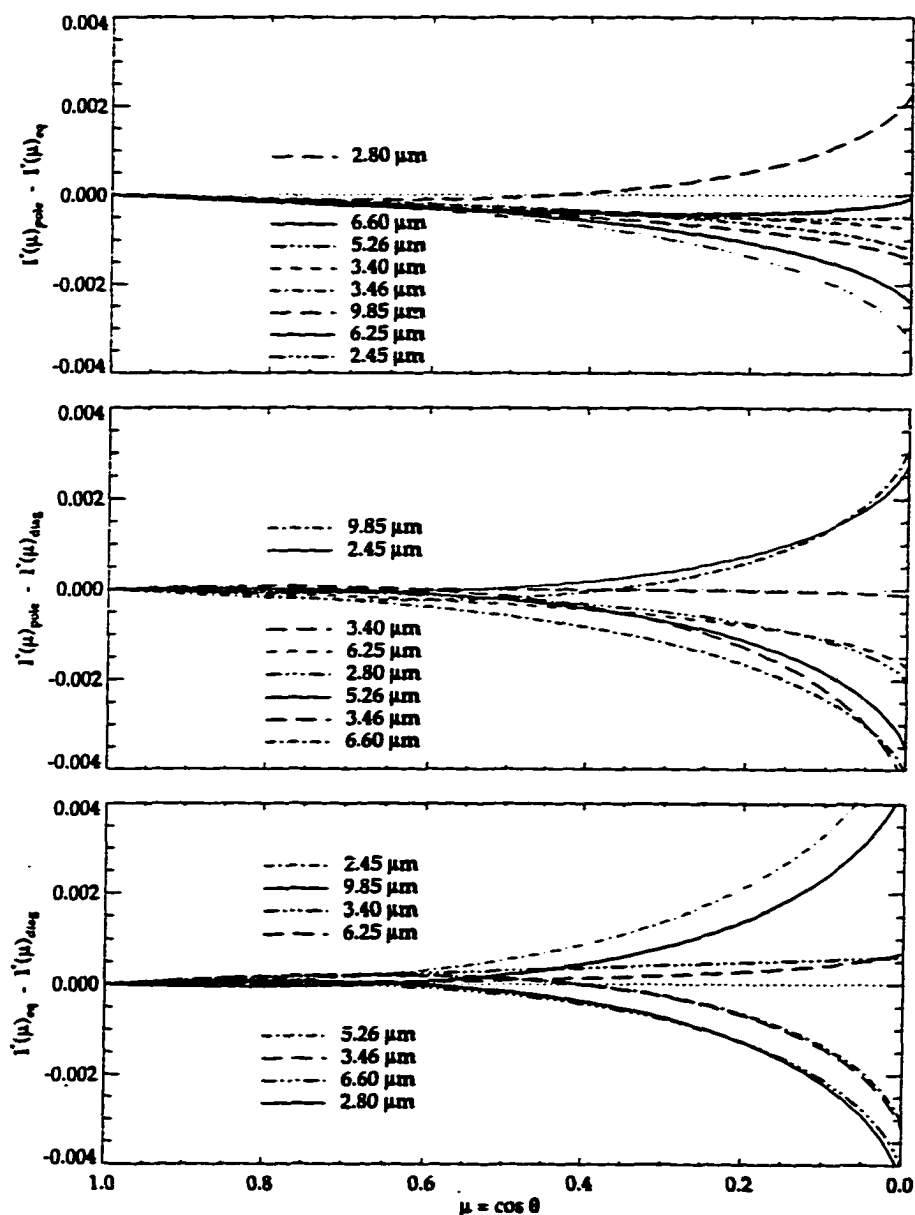


Figure 5.6: Center-to-limb relative intensity differences between results obtained from equator, pole-to-pole, and diagonal (from the 45° NE limb to the -45° SW limb) scans. The differences between the measured relative intensity, $I_\lambda^*(\mu)$, are given as a function of μ at the eight HALOE wavelengths. The line labels coincide with the order of the curves in the plot. All differences are less than the uncertainty of the relative intensity measurements.

5.3 Temperature Analysis

Certain observable quantities, such as limb darkening, over a range of continuum wavelengths serve as the basis for semi-empirical solar atmospheric models. The Vernazza, Avrett, and Loeser model M (VAL-M) gives a comprehensive analysis of the photosphere and chromosphere [2]. In the following, the results from the relative intensity analysis are combined with central intensity measurements to gain information about the temperature structure of the lower photosphere. Two temperature quantities are calculated, and both are compared to VAL-M predictions.

5.3.1 Calculated Disk Brightness Temperatures, $T_b^{disk}(\lambda)$

From the limb-darkening functions, disk brightness temperatures, $T_b^{disk}(\lambda)$, are calculated using equations previously given in Chapter 2. The flux at 1 AU from the center of the Sun is found using Equation 2.26 upon substitution of the expression for the solar intensity, $I_\lambda(0, \mu)$, given by Equation 2.27. In order to obtain absolute flux values, central intensities at HALOE wavelengths are obtained from two sets of measurements. Pierce [44] reported relative values of $I_\lambda(1)$ from 0.9 to 2.6 μm , which Vernazza, Avrett, and Loeser [2] calibrated to the data of Labs and Neckel [45] to obtain absolute units (henceforth: P-LN). There are no uncertainties given for these values. Kondratyev *et al.* [11] reported central intensity measurements and uncertainties from 3 to 13 μm . The combination of these two sets of measurements allows for a linear interpolation of $I_\lambda(1)$ for all eight HALOE wavelengths. These are given in Table 5.2.

Wavelength (μm)	Central Intensity ($\text{W cm}^{-2} \mu\text{m}^{-1} \text{sr}^{-1}$)	
	$I_{\lambda}(1)^{\dagger}$	Uncertainty [‡]
2.45	82.2	–
2.80	51.2	–
3.40	25.1	0.8
3.46	23.4	0.8
5.26	4.76	0.13
6.25	2.36	0.06
6.60	1.91	0.05
9.85	0.394	0.009

[†] Interpolated from P-LN and Kondratyev *et al.* [11] data.

[‡] Derived from Kondratyev *et al.* [11] uncertainty data.

Table 5.2: Interpolated central intensity values and estimated uncertainties at HALOE wavelengths.

Where applicable, estimated uncertainties in $I_{\lambda}(1)$ are also specified in Table 5.2. Since uncertainties are not available for P-LN data, none are assessed at 2.45 and 2.80 μm . At all other wavelengths, the uncertainty is estimated by taking the larger of the two fractional values given by Kondratyev *et al.* [11] at the points used in the interpolation of $I_{\lambda}(1)$.

At each HALOE wavelength, the flux as calculated using Equation 2.26 is listed in Table 5.3. The uncertainty in the flux is produced by the uncertainties in $I_{\lambda}(1)$ and the relative intensity. The contribution from each of these is listed in separate columns in Table 5.3. This is done to point out that the flux uncertainty is predominantly due to the uncertainty in $I_{\lambda}(1)$.

In order to directly compare HALOE results to model predictions, calculated temperature quantities allow for a direct comparison between HALOE results and model predictions. The disk brightness temperature, $T_b^{\text{disk}}(\lambda)$, is found from the computed flux using

Wavelength (μm)	Flux at 1 AU ($10^{-4} \text{ W cm}^{-2} \mu\text{m}^{-1}$)			Disk Brightness Temperature (K)		
	F_λ	Uncertainty from		$T_b^{disk}(\lambda)$	Uncertainty from	
		$I_\lambda(1)^\dagger$	HALOE $\frac{I_\lambda(\mu)^\ddagger}{I_\lambda(1)}$		$I_\lambda(1)^\dagger$	HALOE $\frac{I_\lambda(\mu)^\ddagger}{I_\lambda(1)}$
2.45	52.2	–	0.05	5790	–	4
2.80	32.7	–	0.02	5760	–	4
3.40	16.2	0.5	0.03	5700	130	4
3.46	15.0	0.5	0.02	5660	130	4
5.26	3.10	0.08	0.003	5470	110	4
6.25	1.54	0.04	0.002	5240	110	4
6.60	1.25	0.03	0.001	5220	110	4
9.85	0.260	0.006	0.0003	5030	100	4

[†] Derived from Kondratyev *et al.* [11] uncertainty data.

[‡] Twice the standard deviation (2σ).

Table 5.3: Calculated flux and disk brightness temperatures with uncertainties at HALOE wavelengths.

Equation 2.29. These values are given at each HALOE wavelength in Table 5.3. Also listed here is the uncertainty in $T_b^{disk}(\lambda)$, which is dominated by the central intensity uncertainty (through the flux).

These calculated disk brightness temperatures are compared with the semiempirical VAL-M model of the photosphere. Engelke [46] derived an analytic approximation to VAL-M disk brightness temperatures for wavelengths that include the HALOE wavelength region.

$$T_b^{disk}(\lambda) = 4260 \left[1 + \frac{13.77}{\lambda} \right]^{0.182} \quad (5.1)$$

For λ in μm , this expression is reported to give disk brightness temperatures (in K) to within 0.25% of the model between 2 and 25 μm . Equation 5.1 is used to calculate VAL-M predictions at the eight HALOE wavelengths between 2.4 and 10 μm .

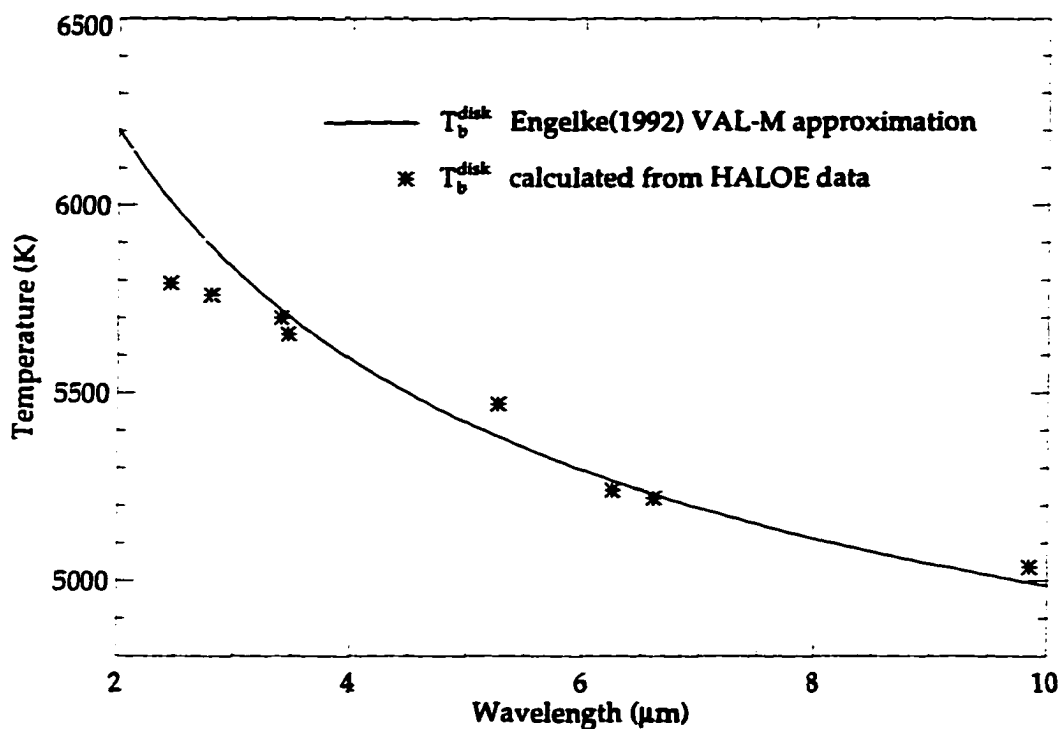


Figure 5.7: Disk brightness temperature comparison between calculated HALOE results and the Engelke [46] VAL-M approximation. Good agreement exists except at the shortest two wavelengths of 2.45 and 2.80 μm .

Figure 5.7 shows the comparison of the calculated disk brightness temperatures with the Engelke (1992) VAL-M approximation. There is good agreement except at the shortest two HALOE wavelengths, where the calculated value is less than the model prediction by approximately 130 K at 2.80 μm and almost 220 K at 2.45 μm . Unfortunately, the dominant uncertainty in the calculated T_b^{disk} value is not available at these two wavelengths; however, the differences here are equal to or exceed the disk brightness temperature uncertainties at other wavelengths.

The discrepancies at these shorter wavelengths can be interpreted two ways. One is that VAL-M is in error and produces higher disk brightness temperatures than observed between 2 and 3 μm . This, however, is not reinforced by comparisons at other HALOE wavelengths. At the other six wavelengths, especially at neighboring 3.40 and 3.46 μm , observations agree very well with the model.

The more likely explanation addresses the accuracy of the central intensities used to calculate the disk brightness temperatures at these HALOE wavelengths. At 2.45 μm , the central intensity is obtained by a linear interpolation between two P-LN data points. The central intensity at 2.80 μm is obtained by interpolating between the last value of the P-LN data (at 2.60 μm) and the initial value of Kondratyev *et al.* [11] (at 3 μm). The question of consistency between these two data sets arises. Central intensities interpolated strictly from the measurements of Kondratyev *et al.* [11] produce disk brightness temperatures that agree very well with VAL-M, while those central intensities interpolated from P-LN produce results lower than model predictions. This suggests inaccuracies with the Pierce [44] measurements or with the absolute scaling of these measurements to Labs and Neckel [45] data by Vernazza, Avrett, and Loeser [2].

5.3.2 Calculated $T(\tau_\lambda)$

After the coefficients to the limb-darkening function are obtained, they can be used in Equation 2.25 to derive the temperature as a function of monochromatic optical depth, $T(\tau_\lambda)$. Figure 5.8 illustrates the behavior of $T(\tau_\lambda)$ for all eight HALOE wavelengths and VAL-M at 2.5 and 10 μm . The range of optical depths in Figure 5.8 is confined to $0.1 \leq \tau \leq 5.0$. After analysis of the contribution functions, Pierce and Waddell [5] concluded that this is the approximate range of optical depths where temperatures are meaningful.

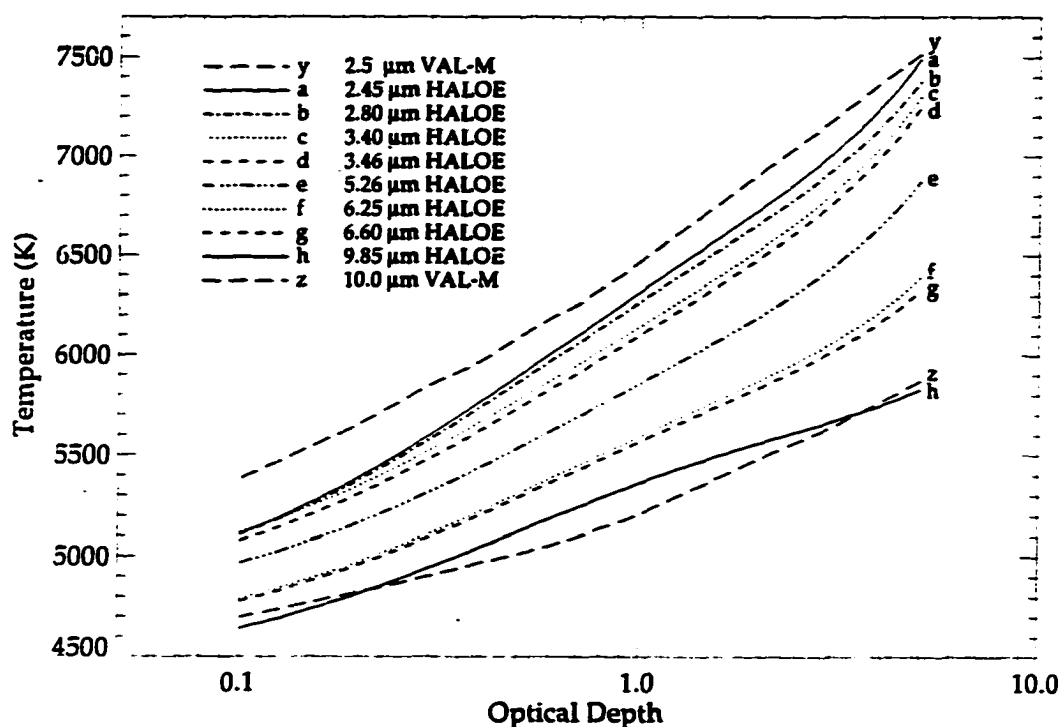


Figure 5.8: Temperature as a function of optical depth for all eight HALOE wavelengths and VAL-M at 2.5 and 10 μm . HALOE results at 9.85 μm and VAL-M at 10 μm compare very well. Calculated temperatures at 2.45 μm , however, are lower than those of VAL-M at 2.5 μm .

In general the behavior of $T(\tau_\lambda)$ at HALOE wavelengths is consistent with respect to wavelength and follows the same trend as VAL-M. At longer wavelengths the results compare very well with VAL-M. The difference in form between the HALOE curve at 9.85 μm and VAL-M at 10 μm is due to the behavior of the calculated function using the limb darkening coefficients. There is a significant difference, however, between $T(\tau_\lambda)$ results and the model at shorter wavelengths. Over the entire range of optical depths, calculated temperatures at 2.45 μm are lower than those of VAL-M at 2.5 μm . The difference between the two also

varies since the temperature results at 2.45 μm exhibit a steeper gradient. This difference approaches 280 K at small τ and decreases with increasing τ to around 100 K at the largest optical depths.

Similar to the findings in the comparison of disk brightness temperatures, the differences between calculated and model values of $T(\tau_\lambda)$ are more pronounced at shorter wavelengths. It is suspected that once again the problem lies with the central intensities. To quantify this, $T(\tau_\lambda)$, found from Equation 2.25, is fit to VAL-M predictions at 2.5 and 10 μm using a nonlinear least squares technique. In this manner, the values of $I_\lambda(1)$ and the numerical coefficients can be obtained at each of the two wavelengths. The central intensities obtained from the fits at 2.5 and 10 μm can be directly compared to the P-LN central intensity at 2.5 μm and the Kondratyev *et al.* [11] central intensity measurement at 10 μm . The limb-darkening functions found from the numerical coefficients obtained through this process can be compared to HALOE results at the nearby wavelengths of 2.45 and 9.85 μm .

After completing the fitting process at 10 μm , the $T(\tau_\lambda)$ function is found to represent VAL-M temperatures very well. The $I_\lambda(1)$ value obtained is compared to the measurement of Kondratyev *et al.* [11] and is found to be 7% higher. This is larger than the 2.2% uncertainty Kondratyev *et al.* [11] reported. The limb-darkening function obtained at this wavelength shows less limb darkening than HALOE results at 9.85 μm . The trend of less limb darkening with increasing wavelength is to be expected, so a small difference between the HALOE measured values at 9.85 μm and the calculated values at 10 μm is not surprising. For example, the difference at $\mu = 0.2$ is less than 2% of the center relative intensity.

Again at 2.5 μm , model temperatures are well represented by the $T(\tau_\lambda)$ function. The resulting relative intensity obtained at 2.5 μm shows less limb darkening than that measured by HALOE at 2.45 μm , but not by a significant amount. The difference is less

than 3% of the central relative intensity at $\mu = 0.2$. The $I_\lambda(1)$ value is over 12% higher than the P-LN central intensity. It is difficult to estimate the uncertainty of the P-LN value; however, expectations of 12% are not unreasonable when considering how the P-LN central intensities were obtained.

Chapter 6

Sunspot Intensity and Temperature

As well as center-to-limb relative intensity, HALOE solar data can also be analyzed to obtain the intensity of sunspots relative to the surrounding photosphere. The intensity relative to disk center was obtained at the eight HALOE wavelengths from data acquired over one solar scan event in which the IFOV scanned a particularly large sunspot. The ratio of sunspot umbra relative intensity to photospheric relative intensity was calculated and compared to other published data at shorter wavelengths. From the intensity data, the temperature at each HALOE wavelength was also found and compared with values of previous published sunspot investigations.

6.1 Instrument Parameters and Data Information

On August 19, 1992, the IFOV passed over a large sunspot during sunrise events. This sunspot was in the NOAA/USAF Group 7260 [47]. Over this 24-hour period, its position on the solar surface was a virtually constant 17° North latitude and varied in

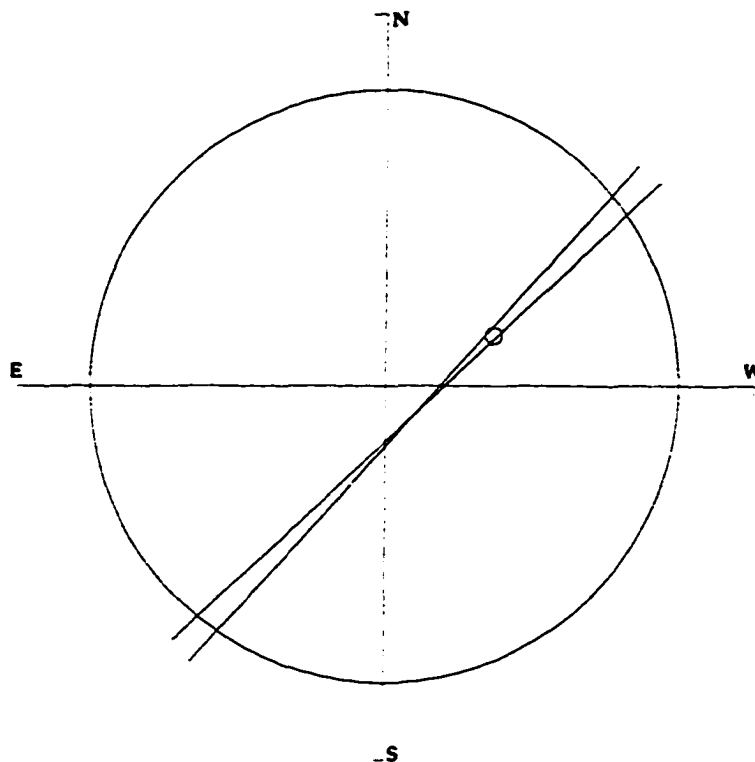


Figure 6.1: HALOE solar scan positions and sunspot position during one event on August 19, 1992.

longitude from 12° to 26° West. The HALOE solar scan data analyzed were from a sunrise event in which the center of the scan path was very nearly across a diameter of the sunspot. The azimuth offset of the IFOV during the solar scans of this event was 2.14 arc min and the instrument temperature was 26.1° C. The coverage of the scan paths during this event and the position of the sunspot are shown in Figure 6.1.

Of the 1460 relative intensity measurements acquired at each of the eight HALOE wavelengths during the solar scans, approximately 400 data points were designated as being recorded over the sunspot. The sunspot points were analyzed using a nonlinear least

squares method to obtain the relative intensity of the sunspot at each of the eight HALOE wavelengths.

6.2 Modified Sunspot Analysis Technique

To obtain relative intensity for this particular sunspot, modifications were made to the general retrieval method that was outlined in Section 4.3. These changes were due to the fact that a second, smaller sunspot also appeared in the IFOV during data acquisition. On the solar surface, these two spots had the same latitude and were separated by 9.5° longitude. The larger, leading sunspot was located very close to the center of the HALOE scan path while the smaller, trailing sunspot's position was displaced horizontally towards the edge of the IFOV. Their orientation relative to the scan path and IFOV is shown in Figure 6.2.

In terms of coordinates relative to the IFOV, the sunspots are separated by 2 arc min in elevation. The vertical separation of the two spots allowed the intensity of either to be found because they would not be located within the IFOV simultaneously. The leading sunspot is analyzed using data accumulated as the centroid of the IFOV passes through or very close to the sunspot. During this time, the second sunspot is displaced horizontally in the IFOV by 1.9 arc min from the centroid.

The initial analysis of this data follows the general procedure described in Section 4.3.2. The measurements were analyzed to obtain the solar limb position in terms of FSSTOP diode number at each wavelength. Next, the data were separated according to whether the measurement contained sunspot or only photospheric information. Relative intensity measurements not associated with the sunspots were analyzed to obtain information on the signal parameters for each of the eight wavelengths. After obtaining these parameters, weighted residuals (observed minus calculated) were calculated at each HALOE

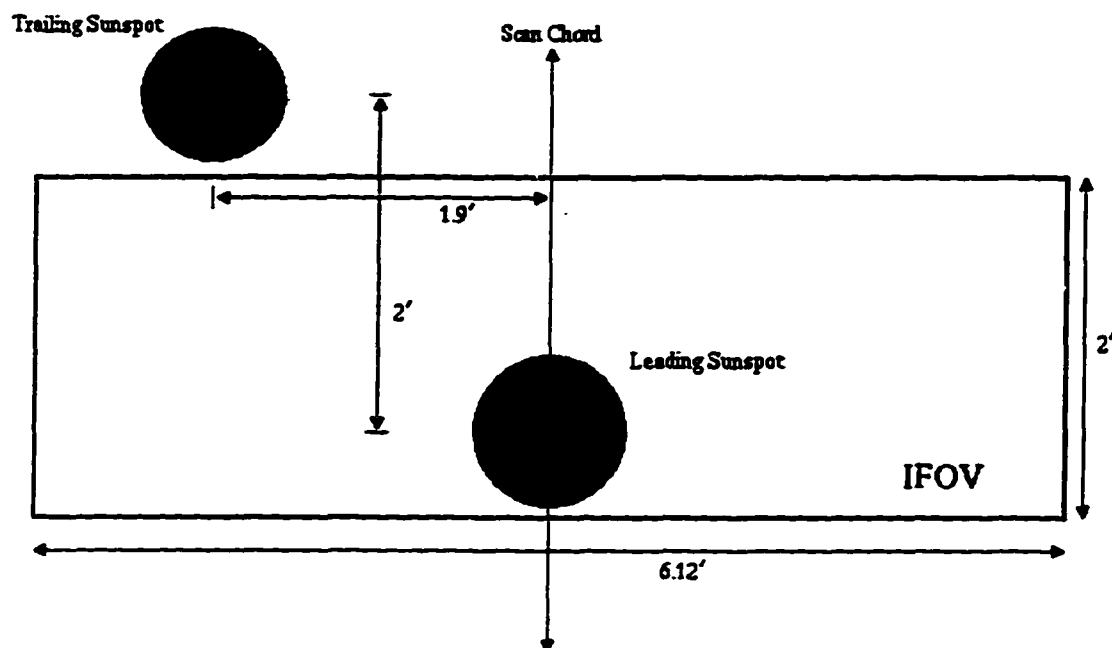


Figure 6.2: Positions of the two sunspots relative to the IFOV.

wavelength and these are shown in Figure 6.3. The sunspot points are indicated by the gaps in these plots. Position values on the abscissa of these plots are given in terms of ϕ/ϕ_{\odot} which is the ratio of the scan angle to the angle from center to limb. The dotted lines in each plot represent the digitization level of the instrument for that particular channel. The standard deviation of the fit ranges from 3.2 to 5.6×10^{-4} , and as Figure 6.3 indicates, the data are fit to the digitization level of the experiment.

It is instructive at this point to show the difference between the relative intensity of the photosphere as calculated by the limb-darkening function and the measurements obtained over the sunspots. The differences as a function of scan angle over the sunspot are

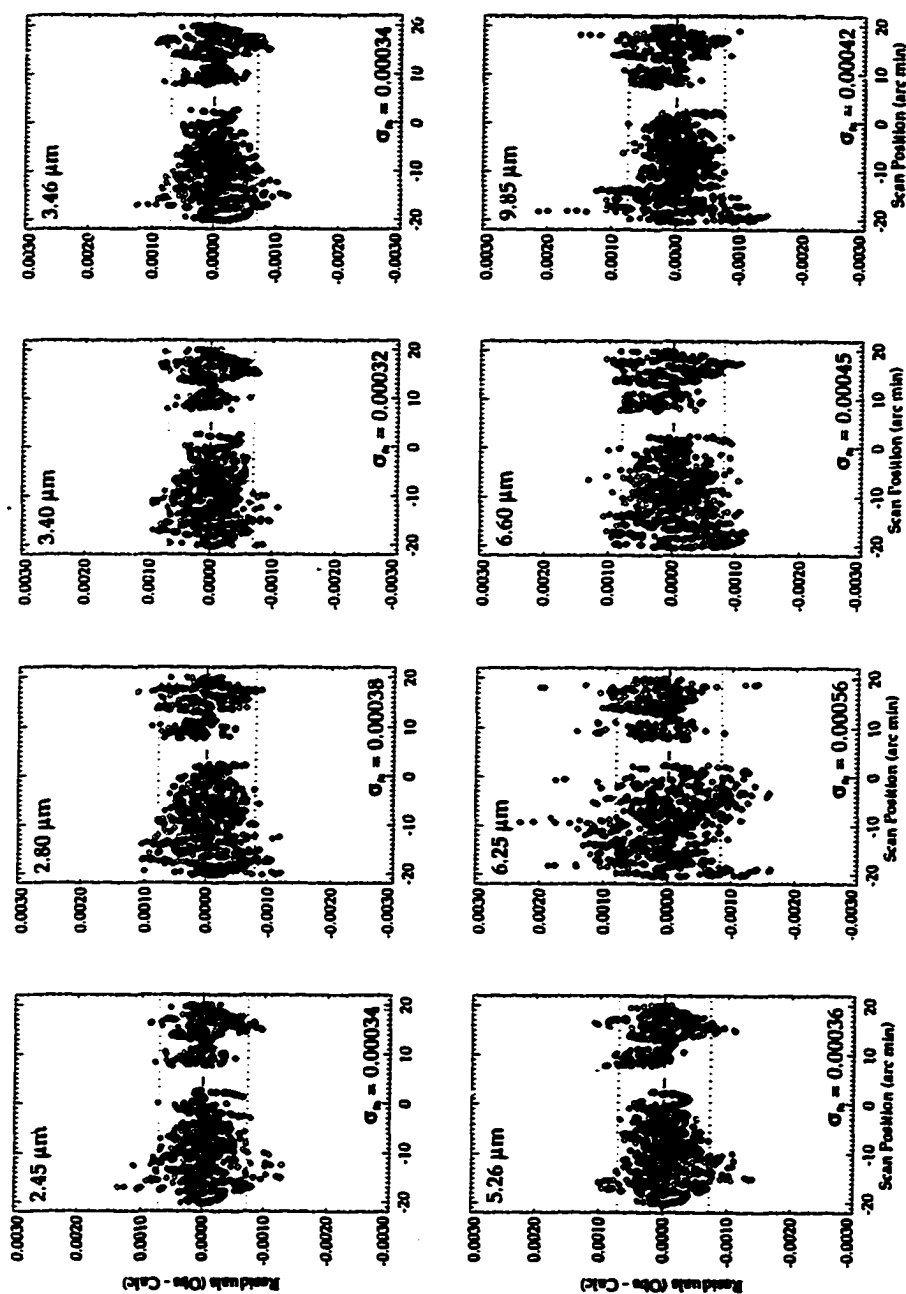


Figure 6.3: Residuals (observed minus calculated) from the analysis of measurements excluding the sunspot. Values on the vertical axis are normalized to unit central intensity. The positions of the residuals is specified by the angle measured along the scan path from scan path center. The standard deviation of the fit, σ_{fit} , indicates that all fits match the experimental data to the digitization level specified by the dotted horizontal line in each plot.

shown at each HALOE wavelength for positive scans in Figure 6.4 and for negative scans in Figure 6.5.

The large relative intensity dip is due to the darker sunspots with most of the difference due to the leading sunspot. Evidence of the trailing spot is seen as the small deviation along the left edge of the dip and is more apparent in the positive scans. This is especially obvious at the four shorter wavelengths where the relative intensity differences are greatest. At each of the four longer HALOE wavelengths, the second sunspot's effects are barely above the digitization level; therefore, very little information can be obtained concerning it. Another trend worth noting is that the intensity difference between the sunspot and the photosphere decreases as wavelength increases. This trend indicates that the ratio of the intensity of the sunspot to the photosphere becomes larger as wavelength increases; however, the sunspot intensity is still less than that of the photosphere.

The limb position and signal parameters are first fixed and data points associated with the sunspots are analyzed. As noted earlier, only data at the four shortest wavelengths contain significant information on the second sunspot; therefore, only these measurements are analyzed initially. The two sunspots are modeled as circles on the solar disk with each designating an area of constant relative intensity. A nonlinear least squares method is used to gain information on the size (radius) and the position (in terms of the scan angle) of each sunspot center as well as the relative intensity of each spot at the four wavelengths.

At the four longer HALOE wavelengths, the two sunspots are fixed in position and size to the values obtained from the analysis of the data at the four shorter wavelengths. The second sunspot does not significantly influence the measured relative intensity at the longer wavelengths, and information pertaining to the intensity cannot be accurately determined. Therefore, at the four longer wavelengths, only solutions of the relative intensity of the leading sunspot are obtained.

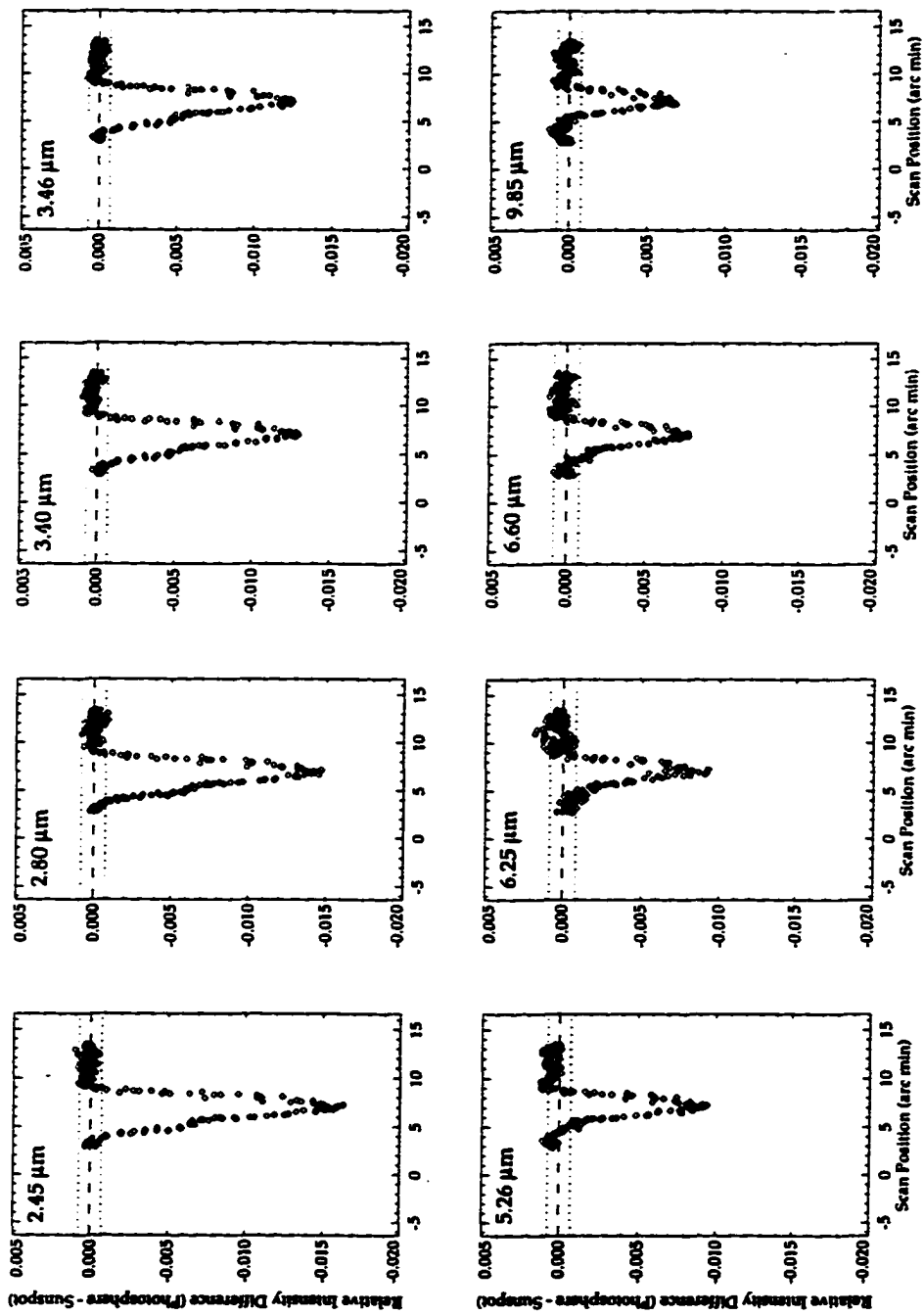


Figure 6.4: Differences between calculated photospheric relative intensity and measured relative intensity of the sunspots for positive scans. The positions are given as angles measured along the scan path from scan path center.

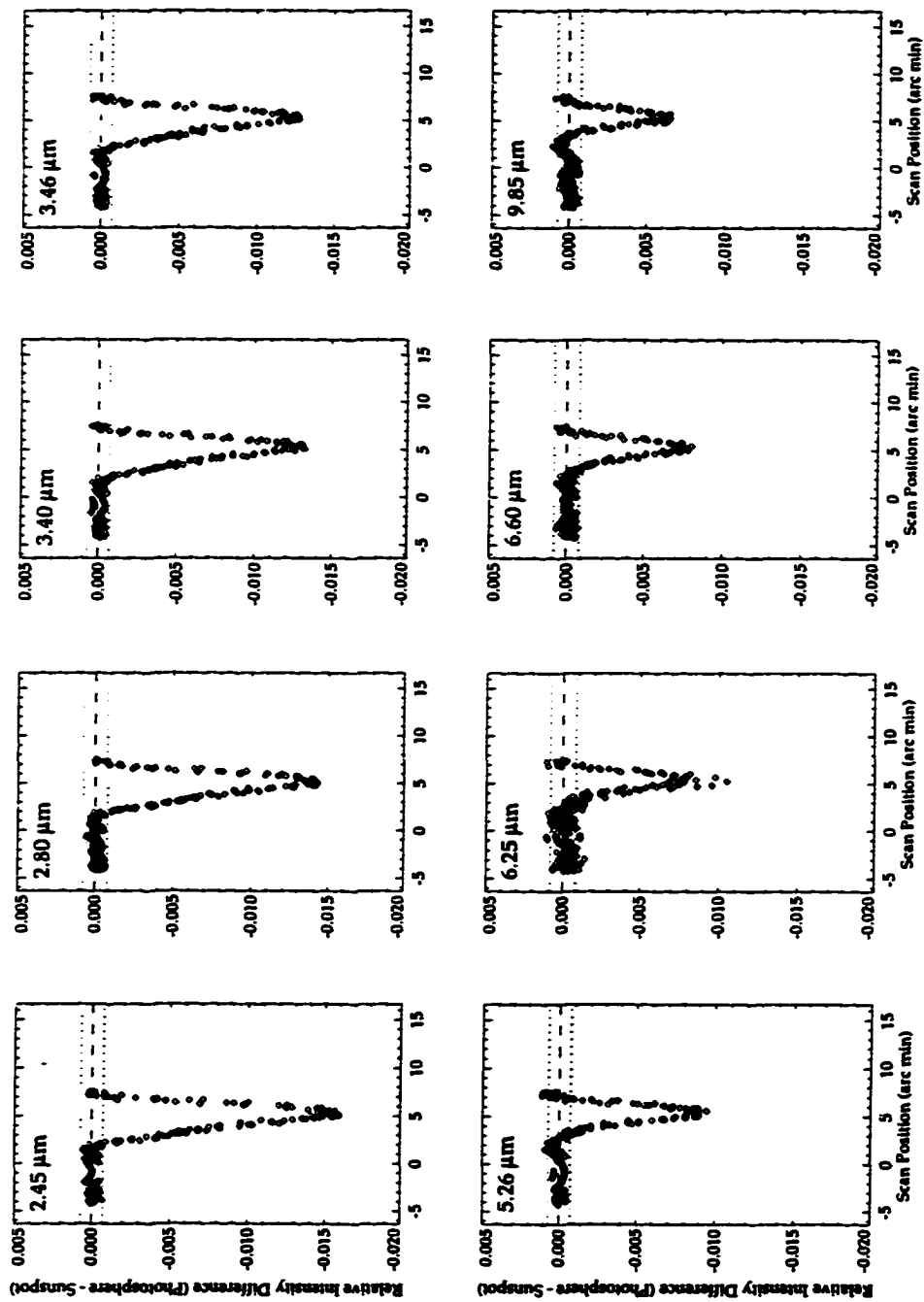


Figure 6.5: Differences between calculated photospheric relative intensity and measured relative intensity of the sunspots for negative scans. Positions are specified in arc minutes along the scan path from scan path center.

Residual (observed relative intensity minus best fit calculated) plots at all eight HALOE wavelengths are shown in Figure 6.6. These values are shown as a function of scan position (measured in arc minutes) across the sunspots. For the fit to the measurements at the shortest four wavelength, the standard deviation of the fit is 4.8×10^{-4} . The standard deviation of the fit is 6.2×10^{-4} for the fit to the data at the four longer HALOE wavelengths. To give an indication of the fit at each wavelength, the RMS values are specified in Figure 6.6. The RMS value for each channel is within the associated digitization level indicated by the dotted lines.

6.3 Sunspot Relative Intensity Results

The information obtained from the preceding analysis can be used to find the relative intensity ratio between the sunspot and photosphere. At each of the eight HALOE wavelengths, the parameter pertaining to the relative intensity of the sunspots was specified as the difference between the relative intensity of the photosphere (given by the limb-darkening function) and the sunspot. The actual relative intensity of a sunspot is found by subtracting this difference from the value of the limb-darkening function. The sunspot relative intensity values are given in Table 6.1 along with the photospheric values and the corresponding umbra to photosphere ratio.

Uncertainties in the last decimal place of these values are given in parentheses immediately following the numbers. In previous discussions, the photospheric relative intensity was judged to be 0.1% (2σ) from the center of the Sun to 0.25 arc min from the limb. The uncertainty in the sunspot relative intensity is derived from the uncertainty in the parameter returned after the fit to the data and the uncertainty in the sunspot radius which is also found from the analysis. The uncertainty of the radius must be considered because the correlation between the radius and intensity parameters is -0.99. The radius uncertainty

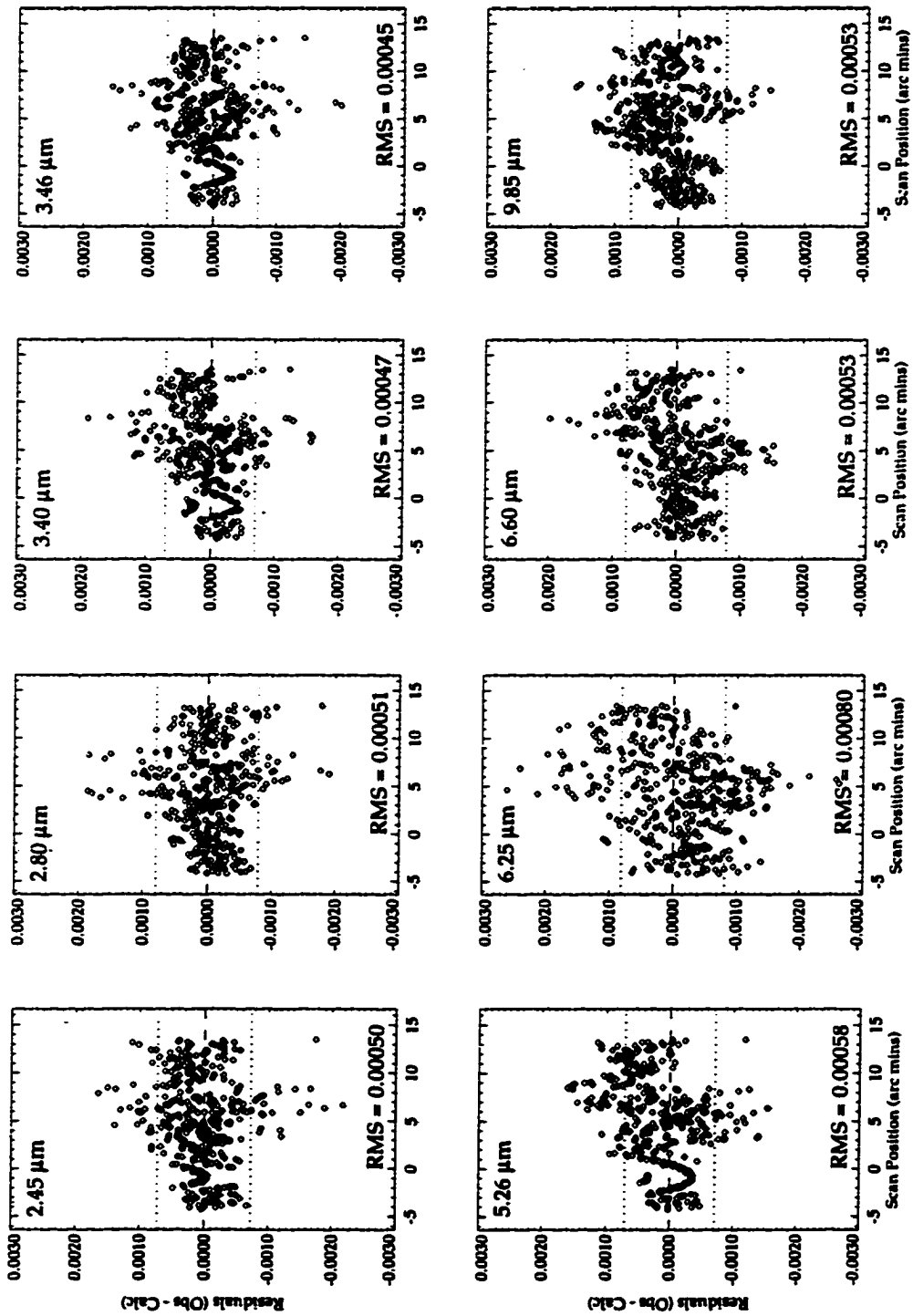


Figure 6.6: Residuals as a function of scan position at each HALOE wavelength after solving for sunspot parameters. All specified RMS values are within the associated digitization level.

Wavelength (μm)	Photosphere	Umbra	Ratio
2.45	0.9860(10)	0.669(6)	0.678(6)
2.80	0.9872(10)	0.690(6)	0.700(6)
3.40	0.9885(10)	0.729(5)	0.737(5)
3.46	0.9886(10)	0.737(5)	0.745(5)
5.26	0.9906(10)	0.809(4)	0.817(4)
6.25	0.9918(10)	0.818(4)	0.824(4)
6.60	0.9920(10)	0.829(4)	0.836(4)
9.85	0.9937(10)	0.867(3)	0.873(3)

Table 6.1: Sunspot and photosphere relative intensity and calculated sunspot to photosphere intensity ratio.

is found to be 0.9%, so it contributes a 1.8% uncertainty to the relative intensity since the intensity depends upon the square of the radius. This uncertainty combined with the uncertainty in the relative intensity parameter of the sunspot produces the umbral relative intensity uncertainty given in Table 6.1.

As a means of judging the reliability of these results, measurements from two other events were analyzed using this same procedure. The geometry of the sunspots in the IFOV was approximately the same; however, the leading sunspot was offset from the centroid of the IFOV by less than one arc minute. Umbra/photosphere intensity ratios were calculated and compared with present values. At each wavelength, the umbra to photosphere relative intensity ratios of all three events were within the calculated uncertainties.

The umbra to photosphere intensity ratios are compared with similar measurements obtained at shorter wavelengths by Albrechtsen, Jorås, and Maltby [18]. Albrechtsen *et al.* [18] measured the relative intensity of the darkest part of the umbra of four large spots as a function of heliocentric angle, θ , at ten wavelengths from 0.387 to 2.35 μm . From each measurement, they found the umbra to photosphere relative intensity ratio, ϕ_u . These values were fit using linear least squares to obtain coefficients to an expression that gives

the values of the ratio as a function of $\mu = \cos \theta$ at specified wavelengths.

$$\phi_u(\mu, \lambda) = a(\lambda) + b(\lambda)\mu. \quad (6.1)$$

Here, $a(\lambda)$ and $b(\lambda)$ are the calculated coefficients. This expression is reported to be a good representation to the umbra to photosphere intensity ratio for $0.3 < \mu < 1.0$. The relations for $\phi_u(\mu, \lambda)$ obtained by Albregtsen *et al.* [18] are given in Figure 6.7 along with the ratio values obtained at eight HALOE wavelengths for the leading sunspot located at $\mu = \cos \theta = 0.908$. The size of the symbols indicating HALOE values is representative of the uncertainty.

The HALOE umbra to photosphere intensity ratios given in Table 6.1 show a consistent trend with wavelength: as wavelengths lengthen, the ratio increases. This is also exhibited by the Albregtsen *et al.* [18] values as seen in Figure 6.7. So in general for a specified μ , the sunspot to photosphere intensity ratio increases with lengthening wavelengths from 0.387 to 9.85 μm . This behavior is due to the altitude of the solar atmosphere at which the intensities are produced. Shorter infrared wavelength radiation is produced in lower photospheric and lower sunspot altitudes than longer infrared wavelengths.

Although the behavior of the HALOE intensity ratio of umbra to photosphere is consistent with wavelength, there is a significant difference between these values and those reported by Albregtsen *et al.* [18]. Judging from the differences between the ratio values at neighboring wavelengths in either data set, the gap between the HALOE value at 2.45 μm and the Albregtsen *et al.* [18] value at 2.35 μm is larger than anticipated. The one-component sunspot model that was adopted for the analysis may be responsible for this since it may not sufficiently represent the varying nature of the umbra relative intensity especially at the edge or penumbra. The circle of uniform relative intensity used to model the sunspot permits a value to be obtained that is essentially an average of the relative intensity over the sunspot area. This is only a first approximation.

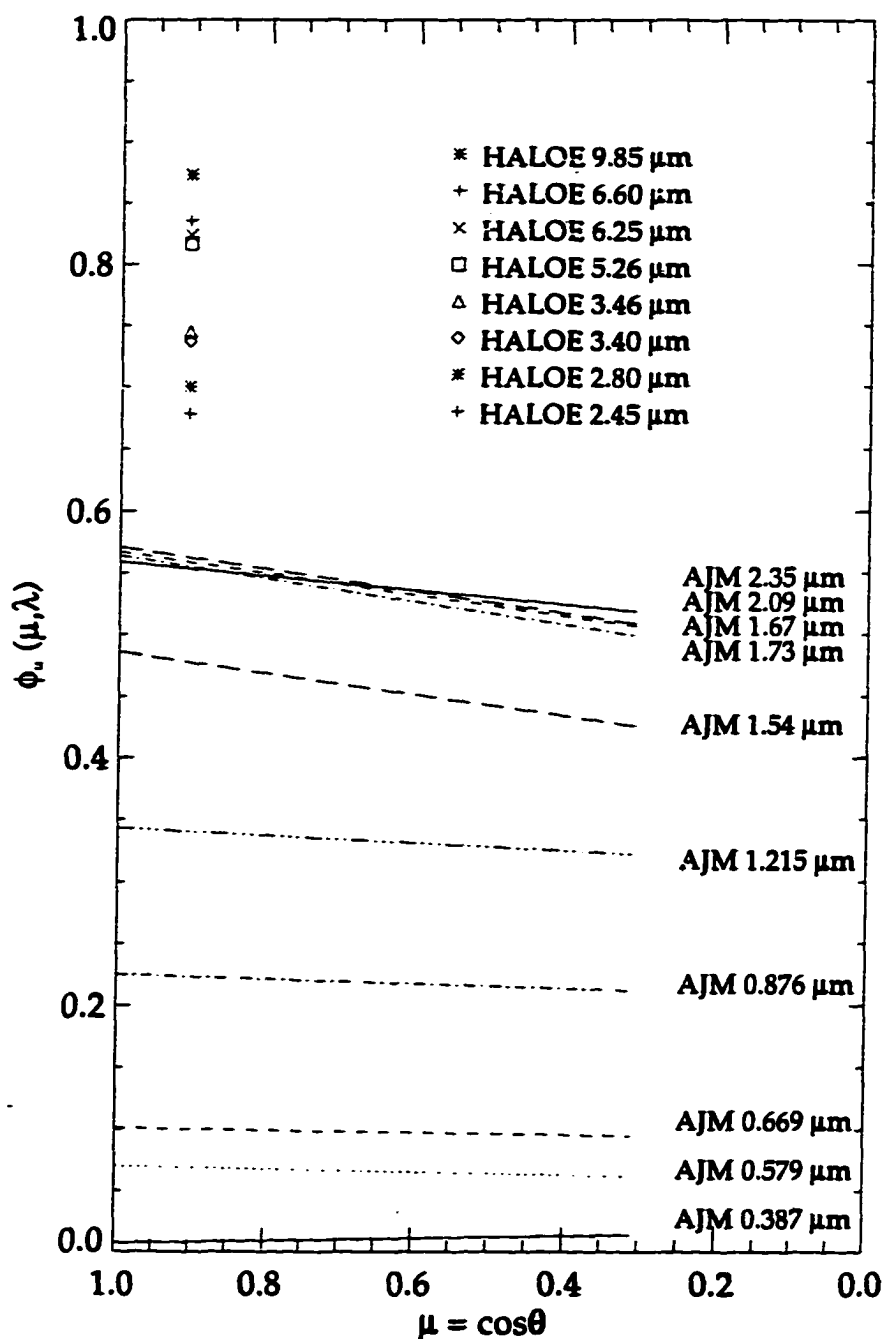


Figure 6.7: Umbra to photosphere intensity ratio at eight HALOE wavelengths along with linear relations obtained from measurements by Albregtsen *et al.* [18] at ten shorter wavelengths. The size of the HALOE data symbols is indicative of the uncertainty.

It should be noted, however, that there is little difference between the ratio values of Albregtsen *et al.* [18] at the four longest wavelengths of 1.67, 1.73, 2.09, and 2.35 μm . This behavior is not expected judging from the increasing trend exhibited by their data at shorter wavelengths. Since their information on umbra to photosphere intensity ratios was obtained from ground-based observations, uncorrected terrestrial atmospheric effects might contribute inconsistent values. This is especially the case at wavelengths near 2.35 μm where atmospheric water vapor is a significant absorber.

6.4 Temperature Analysis

The umbra and photosphere relative intensities along with the absolute central intensity given in Table 5.2 are used to calculate the black-body temperature of the photosphere and the sunspot at all eight HALOE wavelengths. The relative intensity of the photosphere and that of the sunspot are multiplied by the central intensity to obtain absolute units. These are substituted into Equation 2.18 from which the temperature may be solved. Temperature values are given in Table 6.2. Two uncertainties for each temperature are given in parentheses. The first uncertainty includes the consideration of the uncertainty in the central intensity, which is dominant. The second listed is that which is due to the uncertainty in the relative intensity values only. These were previously found to be 0.1% for the photosphere (see Section 5.2) and 1% or less for the sunspot relative intensity (see Section 6.3). The last column gives the temperature difference between the photosphere and the sunspot along with the same uncertainties.

In Figure 6.8, the sunspot temperatures are compared with those calculated by Maltby *et al.* [17] from the observations of Albregtsen *et al.* [18]. The values of Maltby *et al.* [17] show a fairly steep decrease in temperature as a function of wavelength from 1.67 to 2.35 μm . This characteristic is not supported by the longer wavelength HALOE

Wavelength (μm)	Photosphere (K)	Sunspot (K)	Difference (K)
2.45	5992 (—)(4)	4737 (—)(26)	1255 (—)(26)
2.80	5957 (—)(4)	4739 (—)(25)	1218 (—)(26)
3.40	5869 (130)(4)	4760 (103)(23)	1109 (40)(23)
3.46	5839 (143)(4)	4765 (111)(22)	1073 (42)(23)
5.26	5617 (122)(4)	4801 (102)(17)	816 (28)(18)
6.25	5383 (111)(4)	4612 (94)(16)	771 (25)(17)
6.60	5359 (115)(4)	4635 (98)(15)	724 (24)(16)
9.85	5148 (102)(4)	4578 (90)(12)	570 (18)(13)

Table 6.2: Black-body temperature comparison of photosphere and sunspot

temperatures which show a more gradual decrease. If, however, the Maltby *et al.* [17] value at 2.35 μm is ignored, HALOE temperatures would be more compatible and the two sets of data would support a less severe temperature decrease with increasing wavelength. Since the Maltby *et al.* [17] values include the effects of the Earth's atmosphere, temperature at 2.35 μm could be questioned because terrestrial water is a significant atmospheric absorber at this wavelength.

At face value, the HALOE temperatures indicate a smaller temperature gradient than that of the photosphere. This is obvious from the temperature difference values given in Table 6.2. It is expected that longer wavelength measurements would be sampled from successively higher altitudes and that the temperature would drop appreciably. The HALOE temperatures show that either the temperature gradient is small or the sampled altitude range as a function of wavelength between 2.4 and 10 μm is considerably smaller than that of the photosphere.

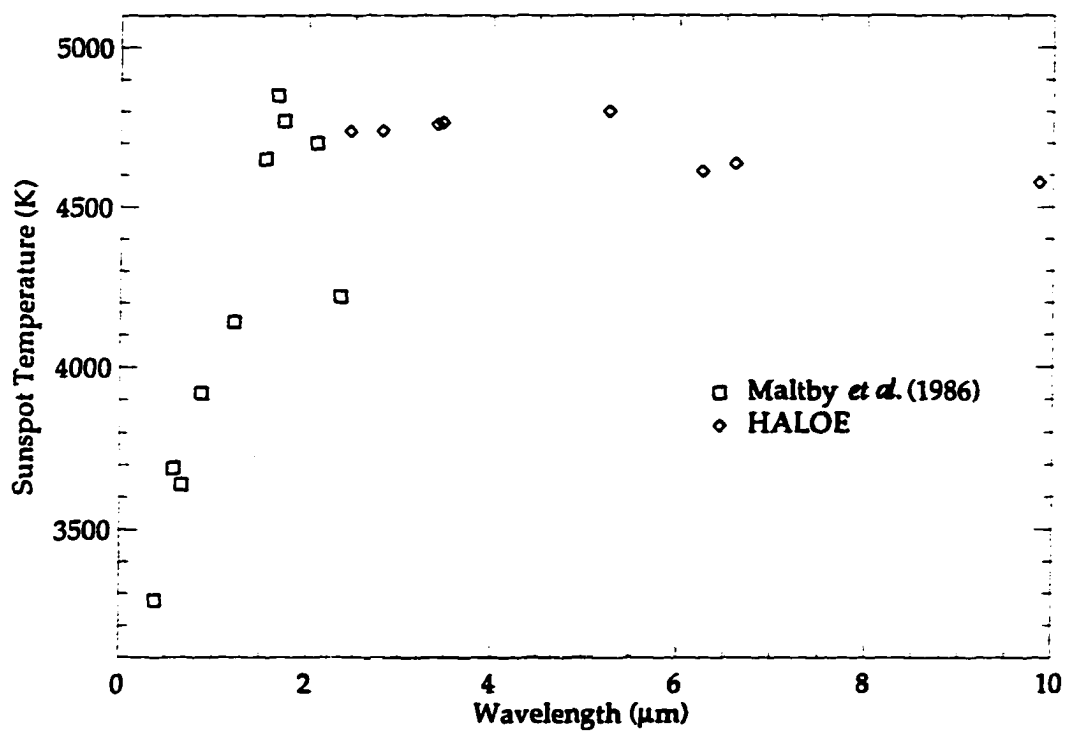


Figure 6.8: Sunspot temperatures calculated by Maltby *et al.* [17] from observations of Albregtsen *et al.* [18] at ten wavelengths and HALOE values.

Chapter 7

Conclusions

Solar observations at infrared wavelengths can be used to probe the structure of the photosphere. Radiation with a wavelength of $1.6 \mu\text{m}$ is formed in the deeper layers of the photosphere with radiation of wavelengths longward of $1.6 \mu\text{m}$ coming from successively higher layers. Infrared limb-darkening measurements across the Sun provide a means to determine the photospheric temperature structure with depth. HALOE solar data provide the first opportunity to examine exoatmospherically acquired relative intensity from 2.4 to $10 \mu\text{m}$. The retrieval method produces satisfactory fits to two coefficients of a limb-darkening function and allows for a description of solar relative intensities to 0.1% (2σ). As expected, the resulting limb-darkening functions are self consistent and exhibit less limb darkening as wavelengths lengthen from 2 to $10 \mu\text{m}$. When compared to other relative intensity measurements, the results compare favorably at shorter wavelengths but show significantly more limb darkening at longer wavelengths. The calculated values of $T_b^{disk}(\lambda)$ and $T(\tau_\lambda)$ tend to support the predictions of VAL-M. From 3.0 to $10 \mu\text{m}$, results from the relative intensity analysis combined with the central intensities of Kondratyev *et al.* [11] produce temperatures that agree very well with VAL-M. Between 2.4 and $3 \mu\text{m}$, however,

P-LN central intensities are used in the temperature calculations. Here, the significant differences seen between the results and the model imply that the P-LN values are low. More absolute central intensity measurements are required to sufficiently judge VAL-M between 2.4 and 3 μm .

Observations have produced umbra/photosphere intensity ratios at wavelengths in the visible and up to 2.35 μm [17–19]. Analysis of HALOE data provides an opportunity to extend the range of available sunspot intensity measurements to 10 μm . A one-component sunspot model was incorporated into the analysis and the relative intensity of a sunspot located close to disk center was retrieved at each HALOE wavelength. The umbra/photosphere intensity ratios are computed and have an estimated standard deviation of 2% or less. The ratios increase successively from the smallest at 2.45 μm to the largest at 10 μm . This trend is similar to that found by Albrechtsen *et al.* [18] for ratios at wavelengths between 0.387 and 2.35 μm that were calculated from ground-based sunspot observations.

In comparing HALOE umbra/photosphere intensity ratios with those of Albrechtsen *et al.* [18], a larger than anticipated difference is seen between the HALOE value at 2.45 μm and that of Albrechtsen *et al.* [18] at 2.35 μm . It should be noted that for $\mu = \cos \theta$ between 1 and 0.3, their intensity ratios at 1.67, 1.73, 2.09, and 2.35 μm are within 0.02 or 2% of themselves; however, differences between successive wavelengths of 0.876, 1.215, 1.54, and 1.67 μm are an order of magnitude larger. These values have not been corrected for atmospheric effects, which are especially important at 2.35 μm . Here atmospheric water vapor is a strong absorber, and ground-based measurements must be interpreted cautiously.

Uncorrected atmospheric absorption in the Albrechtsen *et al.* [18] ratios is not the only explanation for the discrepancy between the two data sets. The one-component sunspot model adopted for the analysis of the HALOE data leads to a solution for the average relative intensity over the sunspot. The average is greater than the relative intensity of the

darkest part of the umbra; therefore, the HALOE ratio values are expected to be higher than the actual umbra/photosphere ratio and should be viewed as upper limits.

Measurements of sunspot intensity can be used to determine the sunspots vertical temperature profile. It is expected that the temperature will decrease with increasing wavelength over the HALOE wavelength interval since observations at successively longer wavelengths samples radiation from higher altitudes. This is found to be the case; however, compared to the trend indicated by the temperatures of Maltby *et al.* [17] over wavelengths from 1.67 to 2.35 μm , the HALOE temperature decrease is considerably smaller. If the Maltby *et al.* [17] temperature at 2.35 μm is ignored, HALOE values are more compatible and the two data sets would support a smaller temperature decrease with increasing wavelength. It is also noted that at HALOE wavelengths, the temperature differences between the photosphere and sunspot indicate a smaller temperature gradient in the sunspot than in the photosphere. This indicates that the sampled altitude range as a function of wavelength between 2.4 and 10 μm is considerably smaller than that of the photosphere or that the gradient of the temperature profile is considerably smaller.

Photospheric relative intensity information obtained from this work have already proven useful in verifying and extending solar models [20,41]. Since the HALOE data set spans over five years at present, several additional relative intensity studies of the photosphere and of sunspots are possible. Information important to studying the variability of the Sun could be gained by studying the photospheric relative intensity over the solar cycle. Further sunspot intensity investigations can also be conducted such as the variation of sunspots with time and the sunspot relative intensity as a function of position from center to limb. It is anticipated that refinements to the modeling of sunspot data will allow for the simultaneous solution of multiple events. These additions might include a more thorough treatment of sunspot and IFOV positions as well as a two-component sunspot model.

Throughout history, studies of the Sun have been seen to lead to new scientific theories as well as new philosophies. Directly observable solar information gives an indication of the physical nature of the universe as well as the processes that influence life on Earth. The development of solar models has been a significant step in gaining information that is not readily obtained observationally. A nonlinear least squares technique has proved to be an effective method in retrieving relative intensity information from HALOE solar data. It has produced information on the quiet and active Sun that is important to developing and verifying solar models. Refinements to the HALOE sunspot analysis technique would improve the existing method and increase the possibility of obtaining more precise umbra/photosphere intensity ratios. Further investigations of the extensive HALOE solar data set, particularly for other sunspots, would provide additional relative intensity information that would enhance our understanding of the Sun.

Appendix A

Sunspot Parameter Derivatives

The most computationally intensive section of the nonlinear least squares technique is the calculation of the derivatives. These derivatives are often calculated using the method of finite differences; however, they can be found mathematically if an explicit differentiable expression is known. The method for calculating derivatives with respect to sunspot parameters is detailed in the following discussion.

The solutions for sunspot parameters are obtained during the last step of the HALOE sunspot data analysis (see Section 4.3.3). In this step of the sunspot analysis, the derivative calculation takes place during the procedure in the forward model that introduces the instrument's spatial effects. Only the designated sunspot points contribute to the analysis here, so derivatives taken at photosphere points are immediately set to zero. At sunspot points, derivatives with respect to the vertical position, the size (in terms of the radius R), and the relative intensity of the sunspot are obtained. Before the derivatives are passed to the nonlinear least squares algorithm, they must be processed through the forward model to account for the effects of the instrument and to obtain the proper units. Each derivative is convolved with the appropriate IFOV function and the Butterworth filter function to

account for the electronic effects of the instrument. Then the derivatives are multiplied by the maximum signal parameter to obtain a derivative result in the correct units. At this point, the derivative values are passed to the nonlinear least squares algorithm for analysis.

The sunspot derivatives can be obtained and processed in this manner because only the intensity expression is dependent on the sunspot parameters. In the convolution with the Butterworth function (Equation 4.14), only the intensity is dependent upon any of the sunspot parameters, q , with $B(t_k)$ independent of these parameters. The partial derivative of $I_B(t_i)$ can be expressed in terms of the partial derivative of $I_s(\theta_i(t_k))$ only.

$$\frac{\partial I_B(t_i)}{\partial q} = \sum_{k=i}^b B(t_k) \frac{\partial I_s(\theta_i(t_k))}{\partial q}. \quad (\text{A.1})$$

Here the order of summation and differentiation are reversed. The convolution with the IFOV function in Equation 4.9 can be written similarly. The order of summation and differentiation are again reversed and $F(\theta_j)$ is independent of the sunspot parameters.

$$\frac{\partial I_s(\theta_i)}{\partial q} = \sum_{j=1}^{61} F(\theta_j) \frac{\partial I_{IFOV}(\theta_i + \theta_j)}{\partial q}. \quad (\text{A.2})$$

The sunspot relative intensity as a function of sunspot parameters can be expressed using $I_{IFOV}(\theta_i + \theta_j)$. During the IFOV convolution, the derivative of the calculated relative intensity with respect to each sunspot parameter is found at every IFOV function position. As explained in Section 4.2.1, for a particular scan angle, θ_i , the relative intensity, I_{IFOV} , is found at $\theta_i + \theta_j$ where θ_j is the IFOV function position. These values of $I_{IFOV}(\theta_i + \theta_j)$ found on the quiet photosphere are given by Equation 4.10.

The sunspot analysis technique uses a circle of radius R and uniform relative I_{spot} to model the sunspot on the solar disk. The relative intensity at IFOV function positions where the modeled sunspot contributes, I_{IFOVSS} , is found by subtracting the parameter value, α , from the relative intensity of the photosphere, $I_{IFOV}(\theta_i + \theta_j)$.

$$I_{IFOVSS}(\theta_i + \theta_j) = I_{IFOV}(\theta_i + \theta_j) - \left(\frac{l}{L}\right) \alpha. \quad (\text{A.3})$$

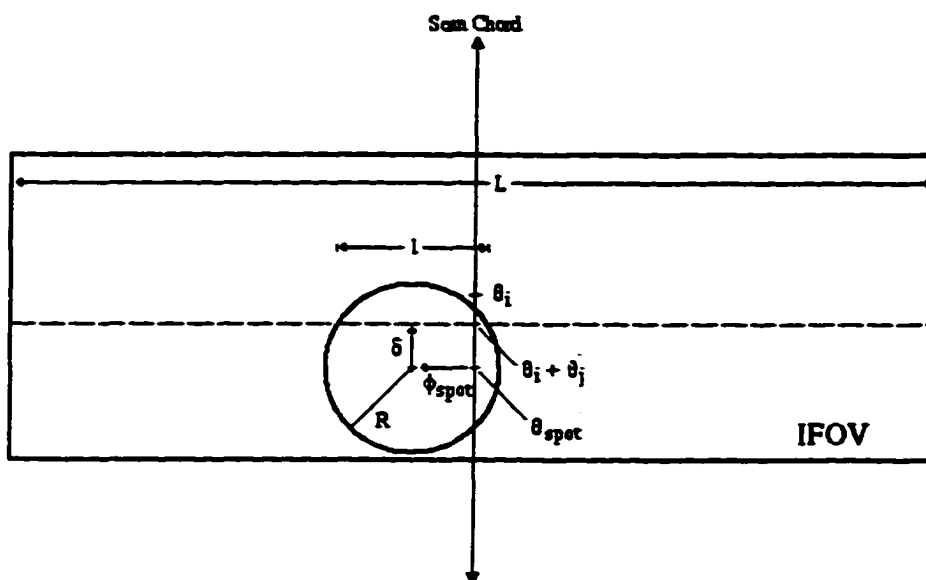


Figure A.1: Geometry of a sunspot of radius R in the IFOV. The sunspot center is given by θ_{spot} measured on the scan chord and ϕ_{spot} measured horizontally from the chord. The angular distance δ represents the vertical displacement of the sunspot center from the horizontal integration. The length of the chord through the sunspot circle on the horizontal at $\theta_i + \theta_j$ is l and the width of the IFOV is L .

To obtain proper scaling, α is multiplied by the ratio of the chord length measured in the sunspot circle along the horizontal, l , to the total horizontal dimension of the IFOV, L . The lengths of this ratio are shown for a circular sunspot of radius R relative to the IFOV in Figure A.1.

From Figure A.1, l can be related to the radius and the coordinates of the sunspot circle center. The chord length l can be calculated using R and δ which is the perpendicular

distance from the center of the sunspot circle to the horizontal line of integration at $\theta_i + \theta_j$.

$$l = 2\sqrt{R^2 - \delta^2}. \quad (\text{A.4})$$

Substituting this result into Equation A.3 gives the relative intensity at the IFOV function angles in terms of R and δ .

$$I_{IFOVSS}(\theta_i + \theta_j) = I_{IFOV}(\theta_i + \theta_j) - \frac{2\sqrt{R^2 - \delta^2}}{L} \alpha. \quad (\text{A.5})$$

The derivatives with respect to the three sunspot parameters can be mathematically obtained by differentiating this equation. The derivatives will include only the quantities in the second term of the sum since the first term, $I_{IFOV}(\theta_i + \theta_j)$, is not a function of sunspot parameters.

Sunspot Relative Intensity Derivative

Sunspot relative intensity information is obtained from the parameter α . The derivative of the IFOV relative intensity with respect to α is given as a function of the sunspot size and position.

$$\frac{\partial I_{IFOVSS}}{\partial \alpha} = -\frac{2\sqrt{R^2 - \delta^2}}{L}. \quad (\text{A.6})$$

Radius Derivative

Information on the size of the modeled sunspot is specified by the radius of the sunspot, R . The derivative with respect to R is expressed as:

$$\frac{\partial I_{IFOVSS}}{\partial R} = -\frac{2R}{L\sqrt{R^2 - \delta^2}} \alpha. \quad (\text{A.7})$$

Position Derivative

The distance δ is measured in arc minutes along a line parallel to the line representing the scan path and can be related to vertical position of the sunspot circle center along the

scan path, θ_{spot} . The vertical position of the sunspot, θ_{spot} , is a parameter in the sunspot solution, and its derivative is the same as the derivative with respect to δ .

$$\frac{\partial I_{IFOVSS}}{\partial \theta_{spot}} = \frac{\partial I_{IFOVSS}}{\partial \delta}. \quad (\text{A.8})$$

$$\frac{\partial I_{IFOVSS}}{\partial \delta} = \frac{2\delta}{L\sqrt{R^2 - \delta^2}} \alpha. \quad (\text{A.9})$$

Bibliography

- [1] J. Bahcall, F. Calaprice, A. McDonald, and Y. Totsuka, *Physics Today* **49**, 30 (1996).
- [2] J. Vernazza, E. Avrett, and R. Loeser, *Astrophys. J. Suppl. Ser.* **30**, 1 (1976).
- [3] C. Allen, *Astrophysicals Quantities, 3rd ed.* (Athlone Press, London, 1976).
- [4] R. Altrock and R. Canfield, *Solar Phys.* **23**, 257 (1972).
- [5] A. Pierce and J. Waddell, *Mem. Roy. Astron. Soc.* **58**, 89 (1961).
- [6] A. Pierce and C. Slaughter, *Solar Phys.* **51**, 25 (1977).
- [7] A. Pierce, C. Slaughter, and D. Weinberger, *Solar Phys.* **52**, 179 (1977).
- [8] H. Neckel and D. Labs, *Solar Phys.* **153**, 133 (1994).
- [9] P. Léna, *Solar Phys.* **3**, 28 (1968).
- [10] P. Léna, *Astron. Astrophys.* **3**, 28 (1968).
- [11] K. Kondratyev *et al.*, *Applied Optics* **4**, 1069 (1965).
- [12] A. Pierce, R. McMath, L. Goldberg, and O. Mohler, *Astrophys. J.* **112**, 289 (1950).
- [13] A. LaRocca, in *The Infrared Handbook*, edited by W. Wolfe and G. Zissis (United States Government Printing Office, 1978), Vol. , Chap. 5, p. 92.

- [14] T. Kostiuk and D. Deming, *Infrared Physics* **32**, 225 (1991).
- [15] P. Kaufmann, *Adv. Space Res.* **8**, 1139 (1988).
- [16] J. Russell, III *et al.*, *J. Geophys. Res.* **98**, 10777 (1993).
- [17] P. Maltby *et al.*, *Astrophys. J.* **306**, 284 (1986).
- [18] F. Albergtsen, P. Jorås, and P. Maltby, *Solar Phys.* **90**, 17 (1984).
- [19] F. Albergtsen and P. Maltby, *Solar Phys.* **71**, 269 (1981).
- [20] H. Neckel, *Solar Phys.* , accepted for publication (1997).
- [21] S. Chandrasekhar, *Radiative Transfer* (Dover Publications, New York, 1960).
- [22] P. Foukal, *Solar Astrophysics* (John Wiley, New York, 1990).
- [23] D. Milasa, *Stellar Atmospheres* (W.H. Freeman, San Fransico, 1970).
- [24] H. Zirin, *Astrophysics of the Sun* (Cambridge University Press, Cambridge, 1989).
- [25] *Handbook of Mathematical Functions*, edited by M. Abramowitz and I. Stagun (Dover Publications, New York, 1972).
- [26] J. Russell, III, M. Lou, L. Deaver, and R. Cicerone, *Nature* **379**, find (1996).
- [27] C. Bruhl *et al.*, *J. Geophys. Res.* **101**, 10151 (1996).
- [28] L. Gordley *et al.*, *J. Geophys. Res.* **101**, 10241 (1996).
- [29] J. Harries *et al.*, *J. Geophys. Res.* **101**, 10205 (1996).
- [30] J. Park *et al.*, *J. Geophys. Res.* **101**, 10183 (1996).
- [31] J. Russell, III *et al.*, *J. Geophys. Res.* **101**, 10151 (1996).

- [32] J. Russell, III *et al.*, *J. Geophys. Res.* **101**, 10163 (1996).
- [33] E. Whittaker and G. Robinson, *The Calculus of Observations; a Treatise on Numerical Mathematics* (Blackie, Glasgow, 1944).
- [34] K. Levenberg, *Quart. Appl. Math.* **2**, 164 (1944).
- [35] M. Carlotti, *Applied Optics* **27**, 3250 (1988).
- [36] D. Benner *et al.*, *J. Quant. Spectrosc. Radiat. Transfer* **53**, 705 (1995).
- [37] D. Marquardt, *J. Soc. Indust. Appl. Math.* **11**, 431 (1963).
- [38] W. Smart, *Text-Book on Spherical Astronomy, 5th ed.* (Cambridge University Press, Cambridge, 1965).
- [39] *Solar Geophysical Data* , p. 25 (1994, Prompt reports No. 598, Part 1).
- [40] *Solar Geophysical Data* , p. 24 (1994, Prompt reports No. 599, Part 1).
- [41] P. Spickler, D. Benner, and J. Russell, III, *Solar Phys.* **165**, 23 (1996).
- [42] B. Cuccin, R. Falciani, G. Moschi, and M. Rigutti, *Solar Phys.* **13**, 33 (1970).
- [43] R. Falciani, M. Rigutti, and G. Roberti, *Solar Phys.* **35**, 277 (1974).
- [44] A. Pierce, *Astrophys. J.* **119**, 312 (1954).
- [45] D. Labs and H. Neckel, *Z. Astrophys.* **65**, 133 (1967).
- [46] C. Engelke, *Astron. J.* **104**, 1248 (1992).
- [47] *Solar Geophysical Data* , p. 90 (1992, Prompt reports No. 578, Part 1).

VITA

Philip T. Spickler

Born in Lancaster, Pennsylvania on November 8, 1962. Graduated from Donegal High School in June of 1981. Entered Bridgewater College in Bridgewater, Virginia in the fall of 1981 and received a B.S. in physics in May of 1985. Enrolled in the graduate program at Ohio University in the fall of 1985 and obtained a M.S. in physics in June, 1988. Taught physics at Bridgewater College in Bridgewater, Virginia from the fall of 1988 to the spring of 1991. Began the graduate program at The College of William and Mary in the fall of 1991. In the fall of 1996, began physics faculty appointment at Ferrum College in Ferrum, Virginia.